ADVANCING TURBULENT SPRAY AND COMBUSTION MODELS FOR COMPRESSION IGNITION ENGINE SIMULATIONS

A Dissertation
Presented to
The Academic Faculty

by

Sayop Kim

In Partial Fulfillment
of the Requirements for the Degree
Doctor of Philosophy in the
School of Aerospace Engineering

Georgia Institute of Technology
May 2019

Advancing Turbulent Spray and Combustion Models for Compression Ignition Engine Simulations

Approved by:

Dr. Caroline L. Genzale, Advisor
School of Mechanical Engineering
Georgia Institute of Technology

Dr. Jechiel Jagoda
School of Aerospace Engineering
Georgia Institute of Technology

Dr. Joseph C. Oefelein
School of Aerospace Engineering
Georgia Institute of Technology

Dr. Wenting Sun
School of Aerospace Engineering
Georgia Institute of Technology

Dr. Alexander Alexeev
School of Mechanical Engineering
Georgia Institute of Technology

Dr. Tommaso Lucchini
Department of Energy
Politecnico di Milano

Date Approved: January 15, 2019

To my family

For their patience, support, encouragement, and unconditional love.

Looking 7.5 years back when I first stepped on the ground in Atlanta, I did not see how challenging life I would go through. Also, I didn't know how grateful I would feel to everyone in the end. I don't know what words can best describe my feelings for everything closing my last chapter of graduate study at Georgia Tech. I sincerely would like to thank all of the people who have enriched my life over the past 7.5 years.

I would first like to appreciate the great support, guidance, and unlimited encouragement from my advisor, Dr. Caroline Genzale. I acknowledge that she has provided me a greatly lucky chance to continue my PhD study in CFD code development and internal combustion engines starting in 2015 spring. Since then, I believe I have earned great opportunities involving conference meetings and searching jobs, and most importantly knowing great friends throughout my PhD career.

I would also like to thank the members of my thesis committee, Dr. Jechiel Jagoda, Dr. Joseph Oefelein, Dr. Wenting Sun, Dr. Alexander Alexeev, and Dr. Tommaso Lucchini for their time and feedback on my dissertation. I also appreciate the guidance provided by my first advisor, Dr. Suresh Menon. I would like to express my apology for not being able to complete my work in his group. But first half of my PhD study for learning CFD and combustion physics under his guidance has well navigated me to build up my expertise in CFD and combustion fields.

A special thanks should first go to following folks in SPhERe lab for their involvement and support during my thesis study: Dr. Benjamin Knox, Dr. Gina Magnotti, Dr. Dorrin Jarrahbashi, Dr. Farzad Poursadegh, Yoontak Kim, Gabrielle Martinez, Boni Yraguen and Ken Maassen. Also, my sincere gratitude also goes to folks in Computational Combustion Lab (CCL) and combustion lab: Dr. Balaji Muralidrahan, Dr. Reetesh Ranjan, Dr. Kalyana Gottiparthi, Dr. Joseph Schulz, Dr. Timothy Dawson, Yusuke Nagoka, Principio Tudisco, Achyut Panchal, Marc Salvadori, and Dr. Brandon Sforzo. I also specially appreciate important assistance and advices for my GTFOAM code development and providing me a job opportunity in Argonne

National Laboratory: Dr. Prithwish Kundu, Dr. Roberto Torelli, Dr. Riccardo Scarcelli, and Dr. Sibendu Som.

Last but not least, very special gratitude quotes should definitely be dedicated to my family and my parents. To my parents, my father and mother: you two have never cast doubt on every single decision I made in my academic career. You two always never stop supporting and encouraging me; so I can always put my best endeavor for my lifelong goal. To my amazing wife, Haley Hwahyun Kim: I can't thank you enough for your endless and unconditional support and belief in me. I honestly would say that I would not been able to accomplish this glorious result without your love. And lastly my last word goes to my lovely daughter Iris Ju-Young Kim: I love you so much. Me and your mother will always love you and promise to live our best life for you. This thesis is dedicated to my wife Haley and my daughter Iris with my best of love.

TABLE OF CONTENTS

LIST OF TABLES

LIST OF FIGURES

LIST OF SYMBOLS

Abbreviations

AMR Adaptive mesh refinement

$ATDC$ After top dead center

CFD Computational fluid dynamics

CFL Courant-Friedrichs-Lewy

CMC Conditional moment closure

CO Carbon monoxide

CTC Characteristics time scale combustion model

$CVCV$ Constant volume combustion vessel

DBI Diffuse back-illumination

DDM Discrete droplet model

DFI Ducted fuel injection

$E-L$ Eulerian-Lagrangian method

EBU Eddy breakup model

ECN Engine combustion network

EDM Eddy dissipation model

EGR Exhaust gas recirculation

EOI End of injection

FL Flame length

FVM Finite volume method

$HCCI$ Homogeneous charge compression ignition

HRR Heat release rate

HTC High temperature combustion

ID Ignition delay

KH Kelvin-Helmholtz

LHF Locally homogeneous flow

$LLFC$ Lean Lifted Flame Combustion

LOL Flame lift-off length

LTC Low temperature combustion

$MPFM$ Eulerian particle flamelet model

MPT Multi-physics turbulence breakup model

NS Navier-Stokes equations

NTC Negative temperature coefficient

ODE Ordinary differential equation

OOP Object oriented programming

PAH Polycyclic aromatic hydrocarbons

$PaSR$ Partially stirred reactor model

$PCCI$ Premixed charge compression ignition

PDE Partial differential equation

PDF Probability density function

$PLIF$ Planar laser-induced fluorescence

PMD Projected mass density

$PPCI$ Partially premixed compression ignition

$RANS$ Reynolds-averaged Navier-Stokes

RCM Rapid compression machine

RIF Representative interactive flamalets model

ROI Rate of injection

RT Rayleigh-Taylor wave instability

$SAMR$ Scattering absorption measurement ratio

SF Separated flow

SI Spark ignition

$SLFM$ Steady laminar flamelet model

SMD Sauter mean diameter

SOC Start of combustion

$SOPR$ Start of particle releas

SOR Start of ramp-down profile

TCI Turbulence chemistry interaction

TDC Top dead center

UHC Unburned hydrocarbons

$USAXS$ Ultra-small angle x-ray scattering

WSR Well-stirred reactor model

Greek Symbols

α_s Segregation factor in direct integration method of combustion model

β MPT model: multiplication factor

χ Scalar dissipation rate

ϵ Turbulent energy dissipation rate

λ Molecular mixing length

$\langle\widetilde{\chi_{st}}\rangle$ Domain-averaged scalar dissipation rate conditioned over stoichiometric mixture

$\mathcal{D}$ Molecular diffusivity

$\mathcal{D}_t$ Turbulent diffusivity

μ Molecular viscosity

μ' Bulk (dilatational) viscosity

μ_t Turbulent viscosity

ω_k Reaction rate of k-th species

ϕ Equivalence ratio

ρ_g Ambient gas density

ρ_g Liquid density

σ_l Liquid surface tension

τ_{bu} Primary breakup time rate

τ_{Faeth} KH-Faeth model: characteristics time scale

τ_{ij} Viscous stress tensor

k Turbulent kinetic energy

r_c Radius of child parcel

r_p Radius of parent parcel

Roman Symbols

B_0 KH model: breakup size constant

B_1 KH model: breakup time constant

C_D Droplet drag coefficient

c_p Specific heat of droplet material

Da Damköhler number

$F_{s,i}$ External force induced source term acting in i-direction in momentum balance equation

G Nozzle offset distance

H Total enthalpy of gas phase mixture

h_k Sensible enthalpy of k-species gas at given temperature

h_s Sensible enthalpy of gas phase mixture

k_g Thermal conductivity of gas phase

Kn Knudsen number

L_{Faeth} KH-Faeth model: characteristics length scale

m_p Diameter of droplet (particle)

m_p Single droplet (particle) mass

Nu Nusselt number

Oh Ohnesorge number

p Pressure of gas phase

p_v Partial pressure of vapor

Re Reynolds number

Sc_t Turbulent Schmidt number

Sh Sherwood number

T Temperature of gas phase

T_{amb} Ambient gas temperature

V_k Diffusion velocity of k-th species

W_k Molecular weight of k-th species

W_l Molecular weight of l-th element (atom)

Y_k k-th species mass fraction

z'' Mixture fraction variance

Z_l l-th element (atom) mass fraction

z_l l-th flamelet marker soluation

z_{st} Mixture fraction conditioned at stoichiometric mixture

z Mixture fraction

SUMMARY

This thesis seeks to investigate the turbulent mixing influence on spray atomization and combustion processes encountered in compression ignition diesel engines. Despite greater thermal efficiency of diesel engine than spark ignition engine, the nature of stratified air-fuel mixture and non-premixed flame gives rise to unacceptable levels of nitrogen oxides (NOx) and particulate matter (PM), thus the use of diesel engines has often been limited to heavy-duty vehicle and industrial power sources. However, recent advancement in diesel engine combustion strategies, e.g. low temperature combustion (LTC), has demonstrated promising pathways towards improvement in the engine-out pollutants. Therefore, particularly in the effort of computer-aided engine design tasks, such a new engine design concept requires more accurate modeling techniques applicable over a broader range of engine operating conditions than those of conventional engine strategies. In the notion of challenges in new engine operating conditions, this thesis aims to present successful implementation of improvement in numerical modeling techniques in high-pressure spray atomization and resulting turbulent spray flame of interest.

Three-dimensional Computational Fluid Dynamics (CFD) in in-cylinder turbulent combustion is considered an integral part of engine design progress, but rather a cost-prohibitive to apply over a broad range of engine relevant conditions. In spite of successful use of existing spray atomization modeling, prior researchers have pointed out some degree of failure in LTC targeted injection strategies. Furthermore, finite rate and strong nonlinearity of chemistry influenced by local turbulent mixing still remain in challenges to account for in cost-efficient CFD analysis. In this context, a new attempt of hybrid spray primary breakup modeling is presented and demonstrated in successful application aimed at LTC technique. In addition, the Representative

Interactive Flamelets (RIF) model with aid of multi-flamelets approach is extensively assessed in terms of predictive capability against classical combustion model. The combustion model employed in this study are fully examined in the general diesel combustion metric, e.g., ignition delay and flame lift-off length as well as newly suggested test metric, combustion recession. The combustion recession has been recently idenfied, but still remain largely unknown. Since the governing physics of this phenomenon is characterized by turbulent mixing coupled with finite rate chemistry, this can be considered as a relevant test metric for turbulent combustion models. In addition, very recent experimental studies have introduced a new non-sooting diesel combustion technique by manipulating direct injection method. The ducted fuel injection (DFI) has thus been demonstrated with its potential of low soot emissions. Knowing that the duct equipped ahead of injector nozzle was identifed to enhance turbulent mixing, investigations of DFI combustion may prove the effectiveness of turbulece-chemistry interaction modeling. This thesis presents comprehensive understandings of aformentioned diesel combustion techniques in terms of several important physics keywords, e.g., turbulent mixing and detailed chemistry.

CHAPTER 1

INTRODUCTION

1.1 Motivation

Combustion is ubiquitous in energy conversion systems such as automotive engines, gas turbine, rocket propulsion, electric power generation and industrial furnaces. Despite the emerging electric vehicles in recent years, combustion technologies in ground transportation still remains in global demand due to their immense benefits of energy efficiency and existing infrastructures. Especially, diesel engines, known as Direct Injection Compression Ignition (DICI) engines, generally achieve greater thermal efficiency than gasoline spark-ignition engines due to the intrinsically higher compression ratios. This implies that the diesel engines generally use less fuel and more air accordingly emitting less carbon dioxide (CO_2). As such, diesel engine powered vehicles are often promoted in demand of more effective environment-friendly transportation system as the worldwide CO_2 regulations have become more stringent.

However, it is notoriously known that the nature of non-premixed combustion dynamics in diesel engine is a major source of particulate matter (PM), which is generally characterized by microscopic particles. Long-term exposure to the PM emission is known to be directly linked to potential of human health problem; e.g., decreased lung function. Moreover, wide use of diesel engines is often discouraged due to the high levels of nitrogen oxides (NOx) pollutant subject to the nature of high peak in-cylinder temperature. NOx emission generally reacts to form smog and acid rain, and increases ground level of ozone. As such, emission regulations have increasingly become stringent; hence it promotes researchers to seek for advanced engine combustion techniques.

Among many attempts to reduce the emissions, one effective way to reduce both NOx and soot has been suggested in the manner of low temperature combustion (LTC). In general, the phrase of low temperature combustion may cover numerous advanced engine combustion strategies, including homogeneous charge compression ignition (HCCI) [1–3] or premixed charge compression ignition (PCCI) [4–7]. As the name implies, a primary goal of the HCCI/PCCI engines is to achieve the most possible homogeneous fuel-air charge prior to ignition; hence to get rid of the source of soot emissions by minimizing locally stratified rich mixture. Simultaneously, overall lean premixed charge can lower the in-cylinder flame temperature, which consequently prevents NOx formation/oxidation kinetics. Such a goal can be obtained by utilizing port fuel injection in the intake manifold [8], or early direct-injection timing with respect to top-dead center (TDC), which is primarily the timing for conventional high temperature combustion (HTC) strategies.

Despite aforementioned advantages, HCCI engines often suffer from combustion instability [9], potentially increasing engine noise. Also, these engines very likely involve as high level of unburned hydrocarbons (UHC) and carbon monoxide (CO) emissions as those emitted from spark-ignition (SI) engines [10–12]. This is an evidence of low engine efficiency which is mainly attributed to low flame temperature and incomplete combustion. Partially premixed compression ignition (PPCI) can be grouped into the same category with the aforementioned LTC strategies, but relatively more associated with the injection-controlled ignition and some degree of mixture stratification. The injection coupled ignition and combustion phasing controls are beneficial for simultaneous reduction of NOx and PM due to its LTC nature and promoted complete combustion by locally achievable non-premixed combustion. As combustion dynamics is obviously correlated with injection transient, early literatures [13, 14] have revealed that the UHC and CO emissions may vary sensitively to injection timing change, suggesting that the optimized injection strategy can mitigate

UHC/CO as well as NOx and soot level simultaneously.

In general, such newly proposed engine combustion techniques alter thermodynamic state of fuel-air mixture and subsequent event of combustion dynamics substantially. In this process, mixing control and subsequent change of chemistry become more important keyword for emission control. Therefore, in order to provide accurate modeling pathway, the 'mixing' and 'chemistry' phenomena should be better taken into account for advancing engine modeling strategy. Towards this goal, this thesis aims to reveal in-depth fundamentals of new engine combustion regimes and emission control strategies from numerous cases of numerical simulations over a range of new engine relevant conditions. In the end, from the adequate modeling assessment and thorough understandings, this thesis ultimately suggests advanced pathways of engine CFD modeling techniques.

1.2 Background and Literature Review

1.2.1 Fundamentals of physics in DICI engine

The fundamentals of direct injection compression ignition engine can be better understood under the notion of important physics of interest; i.e. (1) *fuel-air mixture formation process*, (2) *ignition and combustion phasing*, and (3) *pollutant species formation*. Such transient multi-phase and chemical reaction give great impact on engine exhaust emissions characteristics, such as NOx, PM, UHC and etc. In the following sections, details of such processes will be elaborated in detail.

1.2.1.1 Liquid Spray and Fuel-Air Mixture Formation

The nature of DICI engine characteristics is primarily determined by the in-cylinder fuel-air mixture formation and resulting thermodynamic state of the forming mixture. Therefore, understanding physics governing the fuel-injection process is prerequisite

to build up in-depth knowledge basis of combustion engine characteristics. In general, fuel-air mixture forming process is represented by muti-phase mass transport; i.e., phase transfer, which is characterized by high Reynolds (Re) number turbulent shear flow between ambient air and high-speed liquid jet. Hence, it is essential to better understand the dynamics of injected liquid spray particles in correlation with thermodynamic state of ambient gas.

Earlier attempts to model the in-cylinder spray and evaporation processes began with approximation of transport phenomena. Faeth [15] established two idealized classes of flow approximation; *locally homogenous flow* (LHF) model and *separated flow* (SF) model. The LHF model is defined to form a flow configuration where the gas and liquid phases can be approximately in dynamic and thermodynamic equilibrium. By the assumption, both phases have the same velocity and temperature at each fluid element. On the other hand, the SF model configures the flow in which effects of phase transport are in non-equilibrium; i.e., finite rate of phase trasfer is considered. In the same context, Siebers [16] introduces two categories of spray model; i.e. *mixing control* model and *local interphase transport control* model, equivalent to the LHF model and SF model, respectively. Both mixing control model and LHF model correspond to the flow approximation with phase equilibrium where infinitely fast multiphase transport may hold. In this limit, the spray formation process can be approximated to turbulent gas-jet problem.

As illustrated in Figure 1.1, the scaling law by Naber [17] and Siebers [18] based upon the continuum gas-jet similarity successfully described the maximum penetrating distance of liquid phase accurately against their experimental data particularly under certain limited conditions. The range of test conditions where satisfactory of the scaling law is met appears to lie in the region of relatively high ambient gas temperature, T_{amb}, and high ambient gas density, ρ_{g}, as highlighted in the gray colored area. This suggests that such a turbulent gas-jet similarity assumption; i.e.,

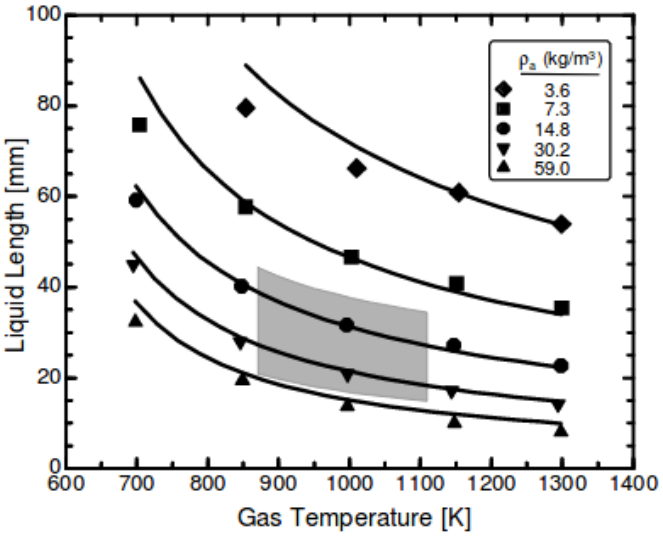

Figure 1.1: *Calculation of liquid length based on phase equilibrium by Siebers [18]*

mixing-controlled spray, may reasonably apply under conventional engine relevant conditions, where the high temperature combustion (HTC) may represent. To be specific, the study [18] addressed that vaporizing is solely limited by the turbulent mixing process aided by high-temperature air entrainment under the condition that the phase-equilibrium assumption may apply. However, as the ambient gas thermodynamic state approaches towards the extreme of low T_{amb} and low ρ_{g}, discrepancy of the prediction gets considerable, suggesting that the phase equilibrium and gas-jet assumption no longer dictates the process in this limit, and relative effect of non-equilibrium phase transport may emerge significantly.

Earlier experimental studies [19, 20] presented liquid injection processes transition from two-phase spray atomization phenomena to single phase diffusion-dominated mixing. To further discuss the spray regime transition and the realization of approximated flow configuration, Dahms and Oefelein [21] conducted their theoretical analysis and developed a regime diagram that quantifies the conditions in which the transition could take place as shown in Figure 1.2. As the figures demonstrate, their study grouped diesel sprays into two distinguishable spray regimes; e.g., *diffusion dominated mixing regime* and *atomization dominated spray regime*. They related the

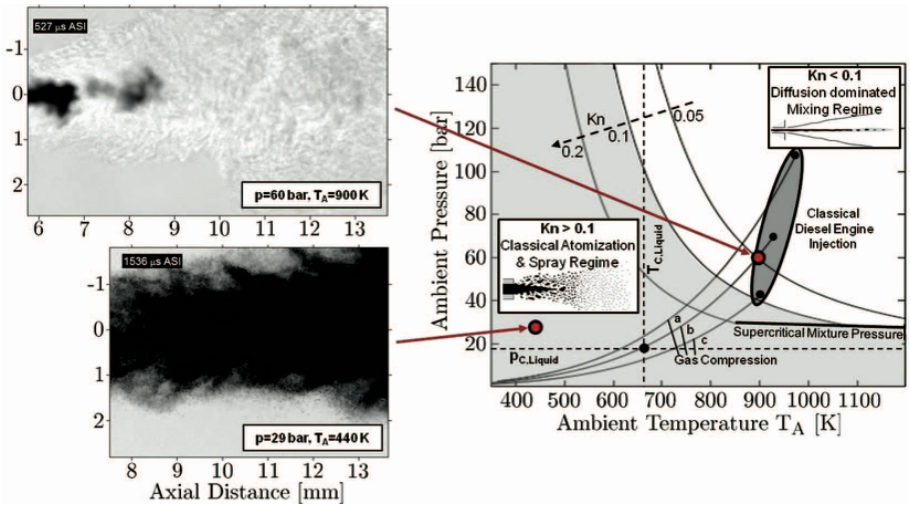

Figure 1.2: *High-speed imaging of liquid injection at subcritical/supercritical pressure conditions for liquid sprays with respect to regime diagram [21]*

transition phenomena to relative scale ratio, Kn, between molecular mixing length, λ, and continuum spray length, L; i.e., $Kn = \lambda/L$. This suggests that the conventional diesel spray may fall into the diffusion dominated mixing category. As the ambient gas condition comes into more LTC-like conditions, however, the phase transport is more predominantly governed by liquid atomization process as illustrated by the left-bottom snapshot in Figure 1.2. Thus, this finding provides consistent context that has emphasized the importance of non-equilibrium phase transport found in the previous scaling law analysis.

1.2.1.2 Spray Atomization

Based on the observations addressed above, one can hypothesize that, under some degree of LTC-like conditions, the local phase transport rates of mass, momentum, and energy between gas and liquid may become more considerable relative to turbulent mixing rate; hence local interphase phenomena, such as liquid jet and droplet breakup, need to be carefully considered. Under the notion that a liquid jet emerging from an injector nozzle initially constitutes a continuum body at high velocity, disintegration of the turbulent liquid jet is appreciated as a key process of atom-

ization forming a cloud of ligaments and small-scale droplets. Such a disintegration of continuum liquid mass is often referred to as primary breakup. The subsequent event of single droplet bursting into smaller droplets in dispersed phase nature is then termed secondary breakup. In this regard, this section outlines in-depth background knowledges centered on liquid spray atomization process.

Many literatures have been devoted to discovering the physics in liquid spray breakup mechanism. Some of literatures in early period were primarily focused on the effect of hydrodynamics on the atomization. Schweitzer [22], McCarthy and Molloy [23] identified the strong influence of nozzle flow velocity profile and provided the first qualitative description of hydraulic mechanisms on emerging turbulent jet disintegration. Sterling [24] further detailed the jet breakup phenomenon in concerns of laminar jet velocity profiles as well as in the presence of nozzle-generated turbulent fluctuation. Both studies noted the combined influence of gas-liquid surface friction and surface tension forces on the disintegration of liquid jet surface. Castleman [25] established the notion that atomization is due to the aerodynamic interaction between the gas and liquid phases, which results in the growth of waves on the liquid-gas interface. The Castleman's hypothesis was later demonstrated by the high-speed photograph technique as illustrated in Figure 1.3. Systematically clarified insight of spray atomization regimes was then established by Reitz [26]. He categorized distinguished four regimes on the map of Ohnesorge (Oh) number versus Reynolds (Re) number and postulated the aerodynamic force of ambient air opposed by the surface tension force predominantly drives the primary breakup process. The idea of aerodynamically induced hydrodynamic instability for a round liquid jet surface was then kept in basis of his proposed Kelvin-Helmoltz (KH) wave breakup model [27]. The model provides linearized solution for dynamic surface wave growth rate in correlation with dispersed droplet length scale.

Several other authors have put forth relative dominance of competing multi-

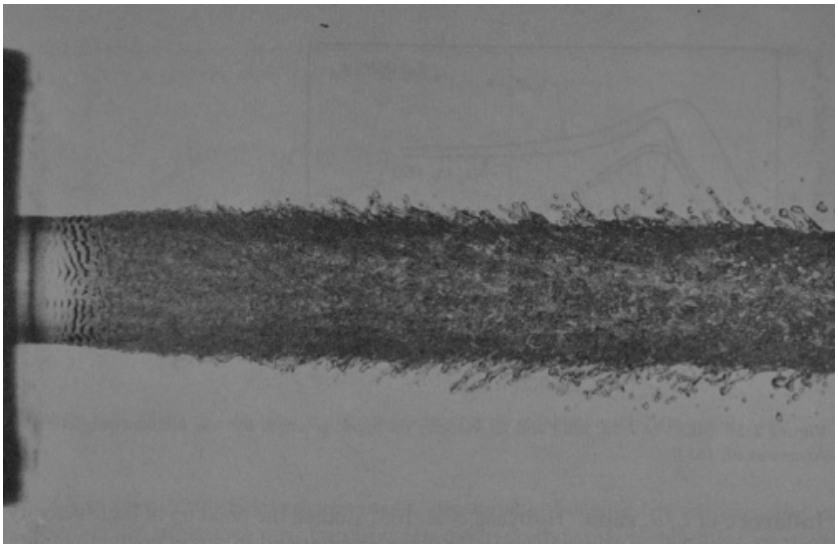

Figure 1.3: *Surface wave instability generated on water jet captured by high-speed photograph [28]*

breakup mechanisms. Reitz and Bracco [27] addressed that no single mechanism is solely responsible for the primary breakup process, suggesting that combination of multi-factors are likely involved. The relative emergence of each factor were extensively described by Wu and Faeth's series of literatures [29–31]. They especially highlighted the role of nozzle-generated liquid turbulence on the primary breakup. They further extended their study to cover broad range of ambient gas conditions and characterized the simultaneous effects of liquid turbulence and aerodynamic flow over a liquid jet surface. Through the evaluations of ligament and droplet sizes obtained by their shadowgraphy images, they characterized three different phenomenological model of turbulence-induced atomization as a function of liquid-gas density ratio, $\rho_{\mathrm{L}}/\rho_{\mathrm{g}}$ and fuel stream kinetic energy. For $\rho_{\mathrm{L}}/\rho_{\mathrm{g}}$ greater than 500, the aerodynamic effects were found to be minimized and liquid turbulent kinetic energy was then identified to be critical for the droplet formation process as sketched in Figure 1.4a. For $\rho_{\mathrm{L}}/\rho_{\mathrm{g}}$ less than 500, on the other hand, they further identified multiphysics breakup mechanisms as illustrated in Figures 1.4b and 1.4c.

Meanwhile, several researchers revealed the mechanism induced by thermo-fluid

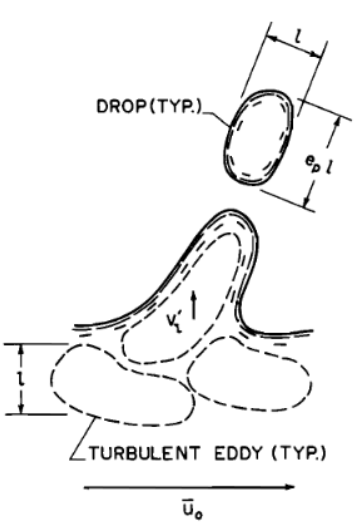

(a) *Nozzle generated turbulence induced breakup*

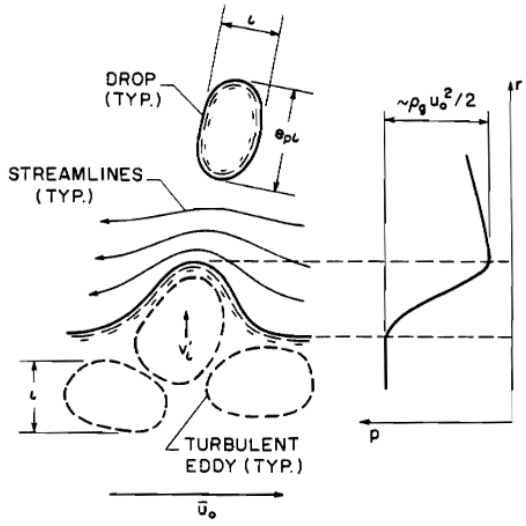

(b) *Aerodynamically enhanced turbulence breakup*

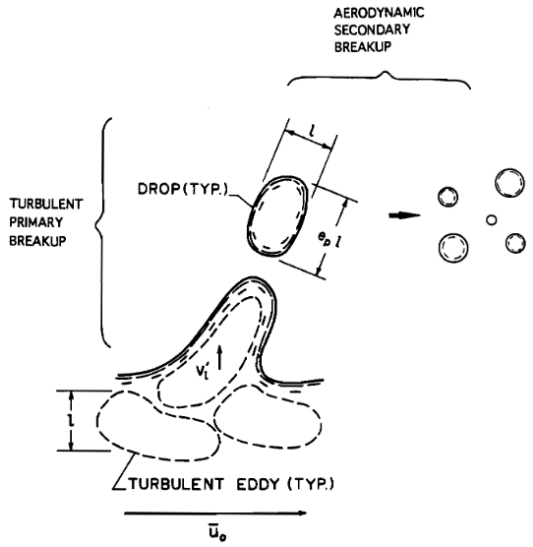

(c) *Merged primary and secondary breakup*

Figure 1.4: *Illustrative multiphysics breakup mechanisms suggested by Wu and Faeth [29–31]*

dynamics. Bergwerk [32] demonstrated an evidence of cavity formation in the corner of nozzle channel by the manner of flow photographs. In the same year, Sadek [33] also pointed out impact of cavity bubbles on atomization process. They commonly discovered that onset of cavitation reduces the discharge coefficient and downstream flow characteristics. Recent advance of optical diagnostics techniques enables to move forward with cavitating flow characterization. This type of mechanism is known to be

generated inside the nozzle flow; hence it generally prevents from directly being visualized. However, thanks to recent introduction of new x-ray radiography technique, Duke and co-workers [34,35] and Khlifa and co-workers [36] have greatly contributed to imaging high-definition cavitating flow dynamics, and identified the influence of inner-nozzle geometry on the cavitating flow features.

1.2.1.3 Ignition, Flame Stabilization, and Emissions

A classical textbook descriptions of diesel combustion were simply based on non-premixed diffusion flame model, thus it approximates the flame structure with anology of equilibrium candle flame analysis. However, advent of advanced laser diagnostics in 1990s [37–40] allowed for time-resolved detailed measurement of combustion dynamics and chemical kinetics in high-speed diesel spray flame. By combining the findings from those measurements, a conceptually well-constructed schematic was sketched by Dec [41] to describe the sequence of mixture formation, spontaneous ignition, premixed combustion followed by diffusion flame, and kinetics of major pollutant emissions as incorporated in Figure 1.5. This section overviews key fundamentals of spray flame initiation and structure in terms of fluid dynamics and chemical kinetics based on this conceptual model.

Ignition delay

Aforementioned spray process in 1.2.1.1 feeds the vapor fuel with aid of ambient hot air flux entrained along the spray trajectory. The vaporized fuel continues to develop along the sides of liquid jet and beyond the liquid penetrating length. Then it prepares the relevant thermodynamic state of fuel-air mixture within flammable range. The head portion of vapor jet in particular may contain relatively uniform premixed charge of rich-fuel mixture at equivalence ratio ranging (ϕ) from 2 to 4. Simultaneously, a series of complex chemical kinetics "*immediately*" proceeds, and initiates later

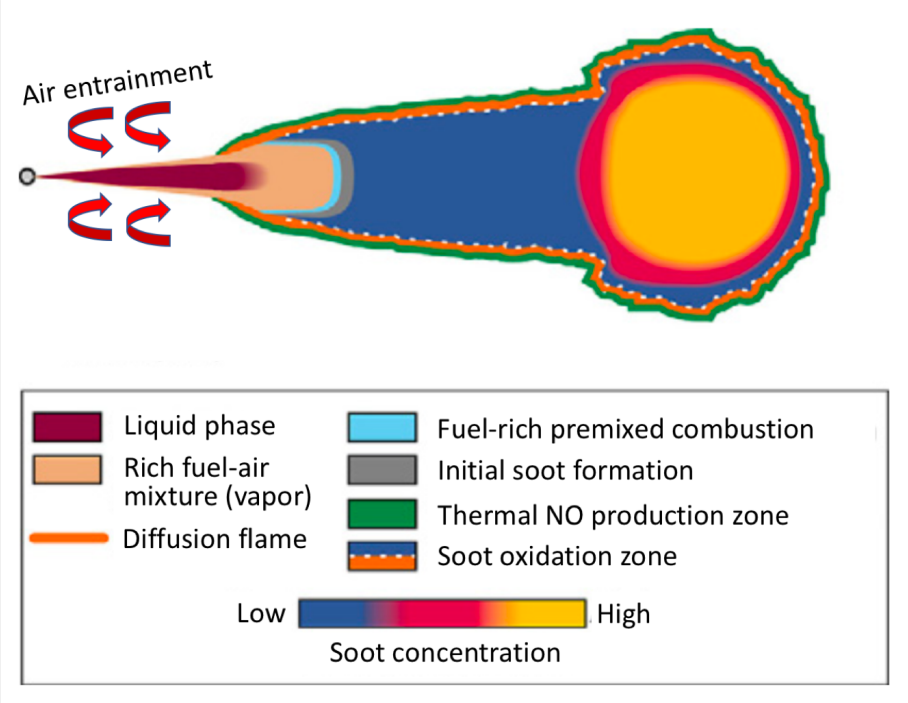

Figure 1.5: *Schematic of conceptual diesel spray flame [41]*

on "*appreciable*" exothermic heat release and maintains flame stabilization. The "*immediate*" reaction does not necessarily mean denying the presence of "*ignition delay*". Rather, it better describes the observable finite rate two-stage combustion accompanying the low-temperature kinetics and high-temperature kinetics, consecutively; i.e., ignition is a phenomenological feature noticeably observed in the second stage combustion and characterized by explosive heat release and high temperature.

Indeed, the ignition delay is considered as a combined result of finite rate of fluid dynamics and chemical kinetics; i.e., physical ignition delay and chemical ignition delay. The physical ignition delay may indicate the residence time of chemically *inert* mixture being fed by high-speed liquid spray injection. The liquid intact core formed immediately after injector needle opening is obviously *chemically frozen*; i.e., low temperature and single phase of liquid mass. The latent heat of vaporization may also significantly decrease temperature of neighbor gas; i.e., cooling effect, thus slowing down chemical reactions. In addition, turbulent mixing plays an important role in

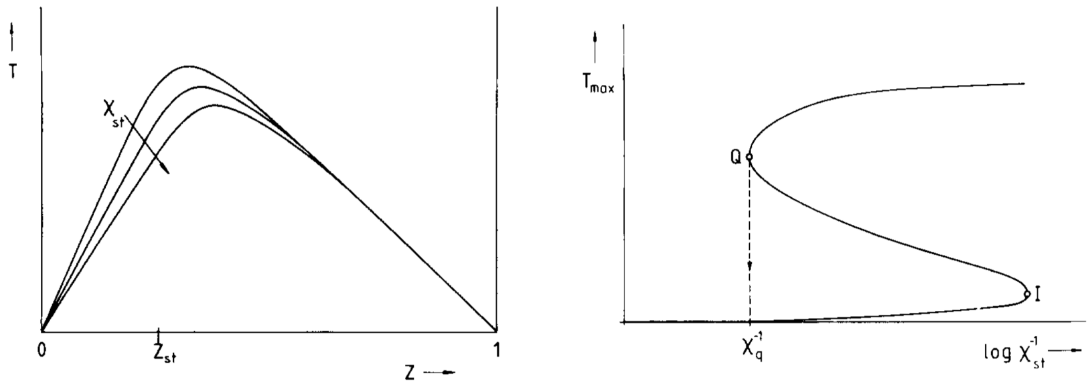

(a) *Effect of scalar dissipation rate conditioned on stoichiometric mixture on flamelet temperature solution*

(b) *S-shaped curve illustrating quenching (Q) and auto-ignition (I) as a function of scalar dissipation rate*

Figure 1.6: *Autoignition and quenching behavior of diffusion flame in correlation with scalar dissipation rate, χ [42]*

slowing chemistry in non-premixed combustion system. To be specific in configuration of a counter-flow diffusion flame, locally intense flux coming from outside the reaction zone (flamelet) may generate steep gradient of scalars (e.g., enthalpy and species) normal to the flamelet, and accordingly increase the strain rate; i.e., stretched flame. Here, the diffusion flame strain rate is well indicated by an introduction of scalar dissipation rate, χ, which is a key parameter to represent the rate of reactive scalar flux. Figure 1.6a illustrates the effect of increased χ on the flamelet temperature as a function of mixture fraction, z. This demonstrates that such a high intensity of turbulent transport may promote excessive thermal diffusion outward from the reaction zone; hence it prevents exothermic chemical reaction, leading to decrease in peak temperature. At an extreme condition, a scalar dissipation rate beyond the critical value may result in local flamelet quenching, whereas lowering χ may help mixture state transition to autoignition phase as depicted in Figure 1.6b. In the context of diesel spray, the local quantity of χ may vary significantly in time and space; e.g., the turbulent intensity is generally maximum in the near nozzle location, thus high χ induced slow chemistry may apply in this region.

The first stage combustion responsible for chemical ignition delay is an outcome of rather complex features of low temperature kinetics of hydrocarbons fuel molecule breakdown and oxidation. In this regard, many literatures have contributed to revealing governing elementary reaction steps involved in this first stage combustion phase. Kuwahara [43] put forth multi-stage processes for low temperature kinetics, including cool-flame and negative temperature coefficient (NTC), and thermal-ignition preparation. Westbrook [44] and Chen et al. [45] classified the first stage combustion phase into two regimes in terms of low and intermediate temperature ranges. Flynn and co-workers [46] also observed that the dominant reaction pathways and major intermediate species formed during the process were shared by different diesel surrogate fuels, and only difference was identified in their effect on the reaction rate. Some experimental studies [47–49] and recent DNS study [50] also revealed a strong correlation with the first stage combustion and formaldehyde (CH_2O), which is an evident indicator of unburned hydrocarbons (UHC) emissions in diesel engines.

As sketched in Figure 1.7a, the first stage combustion is initiated with the emergence of cool flame regime. The cool flame may occur at around 1,100 K or less and at very fuel-rich mixture and be indicated by weak chemiluminescence. Despite the unappreciable appearance, the cool flame plays an essential role in accelerating the formation of ignition kernels [50] by abstracting H radicals from the hydrocarbon fuel molecules. Then following combustion phase comes into the NTC regime, where the reaction rate slows down while the temperature continues to increase by a small degree of factor as seen in Figure 1.7a. The NTC regime corresponds to the time period starting 5 ms through 7 ms in the rapid compression machine (RCM) simulation in Figure 1.7b. It is also noteworthy that the NTC regime is followed by the thermal-ignition preparation regime, in which the chain branching reactions involving H_2O_2 become dominant. This so-called intermediate temperature kinetics continues until it reaches around 1,000 K, where H_2O_2 starts to decompose and OH

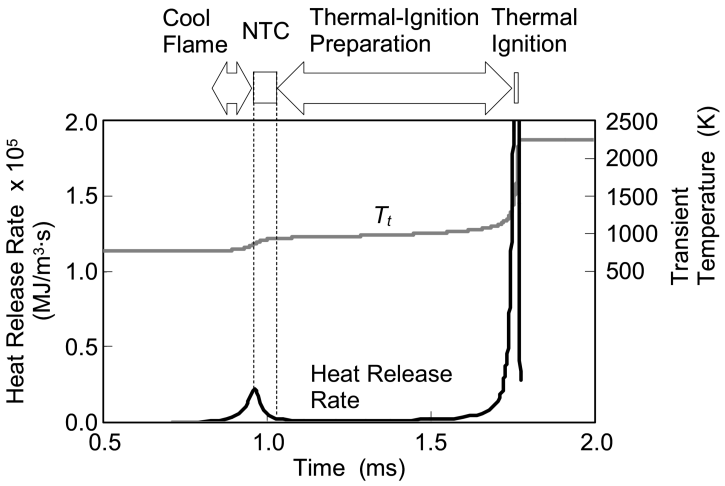

(a) *Four different stages of typical hydrocarbon oxidation process by Kuwahara and Ando [43]*

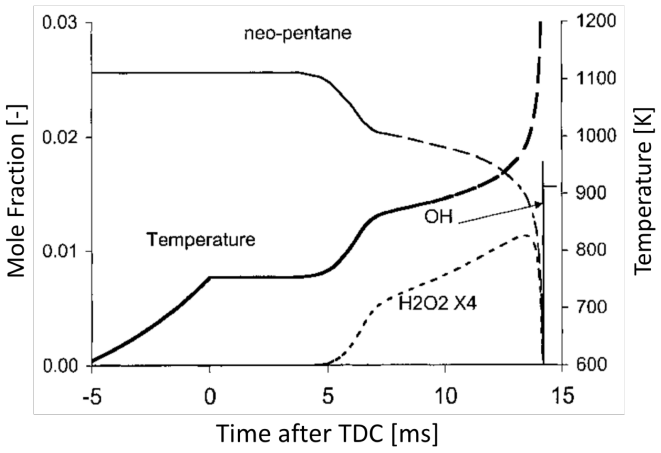

(b) *RCM simulation of temperature and fuel (neo-pentane) and major intermediate species in the first stage combustion period by Ribaucour et al. [51]*

Figure 1.7: *Multi-staged feature of low temperature kinetics for hydrocarbon fuel oxidation*

explosively increases with exothermic heat release; then reaction finalizes the first stage combustion.

Flame stabilization

The fuel-air mixtures that have undergone the first stage combustion generally stay at relatively rich equivalence ratios ranging from 2 to 4 before they reach fully burned and stabilized diffusion flame [41]. The initiation of rich mixture burning is then observable in the leading portion of the jet with a large amount of heat release. This

combustion phase is therefore featured with partially-premixed combustion regime as indicated (color-cyan) in Figure 1.5. Since the high temperature kinetics just initiates in this region, highly exothermic chemical reactions and production of OH radicals are underway across downstream of this region; hence such a high chemiluminescence feature spots the flame lift-off length for diesel spray flame. Dec and Espey [52] demonstrated this chemical activity by imaging electronically-excited OH* and CH* in their experiment. It should also be noted that due to the fuel-rich nature, there still remains high concentration of fuel fragments; e.g., C_2H_2, C_2H_4, and C_3H_3, originated from the first stage combustion [46]. Those species are accordingly consumed to notably form soot or soot precursors, e.g., polycyclic aromatic hydrocarbons (PAH), and the soot formation/oxidation proceed across the entire spray flame.

The burning mixtures downstream of the fuel-rich premixed flame (color-blue) continue to evolve as hot temperature products; e.g., CO_2, H_2O, CO, CH_4, and soot precursors [46]. Then they reach a stoichiometric condition farther downstream and form a thin reaction zone (diffusion flame) in the jet head. Then the diffusion flame extends upstream along the stoichiometric mixture to the point where the high temperature reaction can be sustained by moderate level of scalar dissipation rate, χ. Therefore, the diffusion flame encircles the cross section of soot precursors and hot products forming zone and becomes stabilized in the distance of so-called flame lift-off length (LOL) from the injector. It should also be noted that a part of soot particles is then oxidized across the diffusion flame. While the premixed combustion zone now steadily sits in the LOL distance, the jet head continues to grow until the end of injection (EOI) is met. This combustion phase is thus referred to as *mixing-controlled combustion* because the mixing (injection) keeps feeding the fuel-air mixture and therefore maintains the flame stabilization.

Emission Formation

The most significant pollutants emitted by diesel engines are NOx emissions and particulates (soot). Unlike spark-ignited (SI) engines where the reactant mixture is predominantly well-mixed (homogeneous) charge in nature, the prevailing characteristics of diesel engine emissions essentially results from burning stratified (heterogeneous) fuel-air mixture in cylinder prior to exhaust valve opening. To be specific, the spatiotemporal variance of equivalence ratio and flame temperature across the in-cylinder mixture charge is obvious; e.g., cooling effect of droplet vaporization forming rich mixture beyond flammable limit, rather low temperature of fuel-rich premixed combustion (ϕ ranging from 2 to 4), and close equilibrium temperature at diffusion flame kernel formed at local stoichiometric mixture.

In general, under conventional diesel combustion operating conditions, NOx and soot emissions are traded against each other. Soot particles, for example, start to form and grow in fuel-rich premixed combustion region and partly or mostly burn off at high temperature diffusion flame reaction zone. The diffusion flame reaction zone is the source of high concentration of OH radicals due to the excessive heat release at stoichiometric condition; hence, soot oxidation can be promoted by the OH and O radicals fed from the ambient oxidizer side [53]. On the other hand, the fuel-rich premixed combustion zone (color-blue) in Figure 1.5 is not favorable to NO production, whereas NOx emissions are unavoidable with the high temperature flame; i.e., the NOx formation kinetics is mainly attributed to the Zeldovich mechanism [54], which is strongly correlated with flame temperature. Therefore, the trade-off relationship between the two emissions are dependent on many aspects of engine design as will be further discussed in following section.

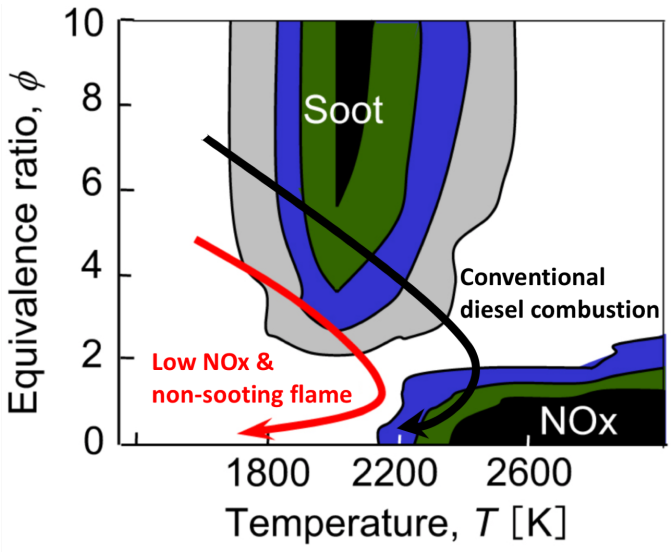

Figure 1.8: *NOx and soot formation/oxdiation for conventional diesel combustion and LTC regime on $\phi - T$ diagram [55]*

1.2.2 Low Temperature Combustion (LTC)

LTC strategies are generally used in an effort to reduce NOx and soot emissions simultaneously. In many cases, these techniques leverage advanced injection timing that introduces liquid fuel into combustion chamber at relatively low ambient temperature and density conditions. Consequently, the LTC techniques may naturally alter the primary driving physics in spray and combustion processes. The schematic of $\phi - T$ diagram in Figure 1.8 presents the path-dependent NOx and soot formation for LTC (red solid line) against the conventional HTC (black solid line) strategy; increased liquid phase residence time by the early injection may feed relatively less rich mixture prior to sooting flame, and the overall lean mixture results in relatively low flame temperature, ranging from 1,800 K to 2,200 K, which may be enough to burn off soot particles and prevent NOx from being produced significantly [55, 56].

1.2.2.1 Early-Injection Partially Premixed Compression Ignition (PPCI)

Recently, Musculus and Singh and co-workers [13, 49, 57] have extensively compiled studies of PPCI engine combustion dynamics achieved by early-injection and late-

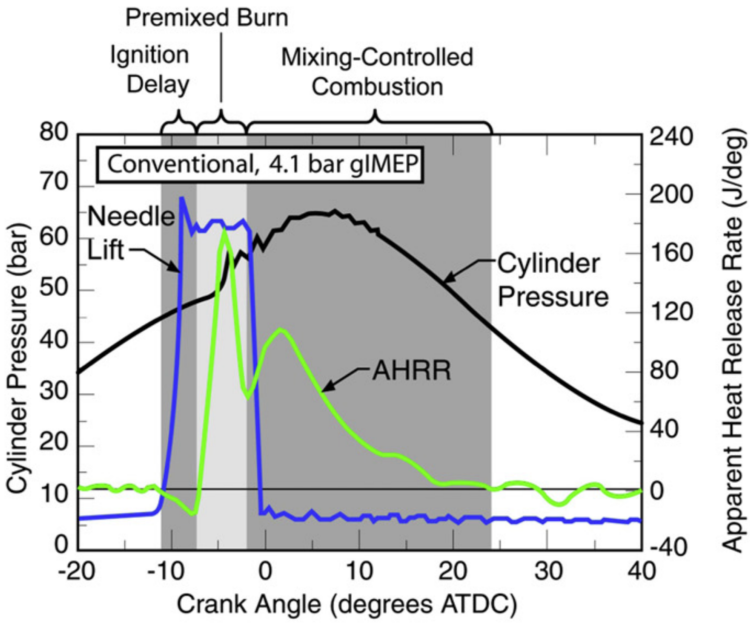

(a) *Conventional HTC engine dynamics: start of injection (SOI) at -11° after top-dead center (ATDC), low-load condition [41]*

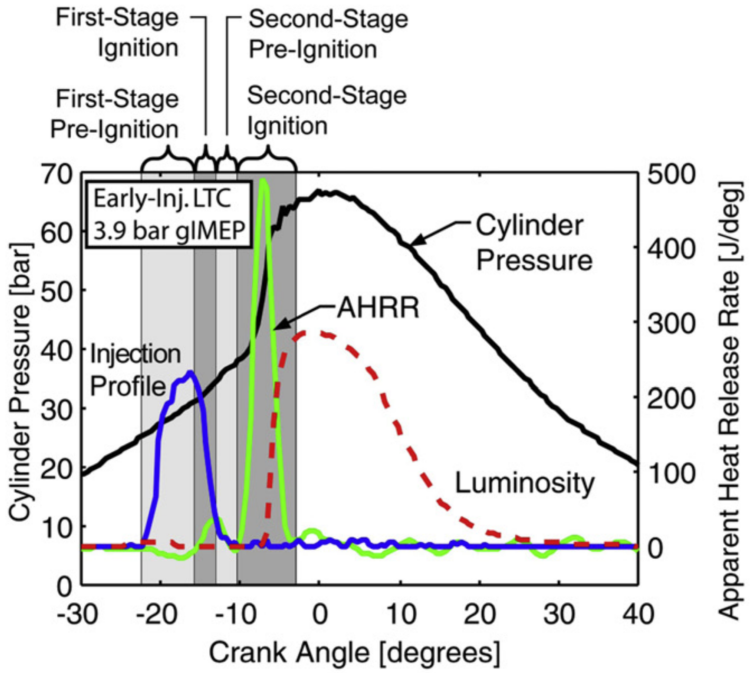

(b) *LTC engine dynamics: start of injection (SOI) at -22° after top-dead center (ATDC), low-load and EGR diluted PPCI condition [57]*

Figure 1.9: *Comparison between HTC and LTC in terms of injection profile, cylinder pressure, and heat release rate (Soot luminosity is only evaluated at PPCI condition) [49]*

injection techniques. This thesis is focused on the early-injection PPCI strategy, where the mixing-controlled combustion phase may be engaged to some extent. The distinctive feature of early-injection PPCI engine against conventional HTC engine is comprehensively illustrated in Figure 1.9. The conventional HTC engine for example exhibits three divisions of apparent heat release rate (HRR); ignition delay, premixed burn, and mixing-controlled combustion as addressed in the previous section 1.2.1.3. The cool-flame is not appreciable in the HRR trace. However, for the PPCI condition shown in Figure 1.9b, the HRR presents additional divisions pertaining to the first stage combustion and the time period for the low temperature kinetics appears to be elongated. It is notable that the first stage of positive HRR arise for short timespan peaking at -13° after top dead center (ATDC); it is considered as appearance of cool-flame. This distinctive feature of PPCI is attributed to the fact that early injected fuel with exhaust gas recirculation (EGR) is much diluted with longer residence time (i.e., longer ignition delay) and the lowered temperature also slows the rate of chemistry; thus chemical reaction undergoes temporally more extended low temperature kinetics than for HTC engines. Therefore, it can be said that the nonequilibrium chemistry effect may become substantial.

1.2.2.2 Unburned Hydrocarbons (UHC) emissions

Despite the positive potential of PPCI in reduction of NOx and soot emissions, other emissions, e.g., unburned/partially burned hydrocarbons (UHC) and CO emissions, may become an outstanding issue in the LTC engines [13, 58]. The source of those emissions were experimentally [13, 59] and numerically [12] identified by overly lean mixture and incomplete combustion associated with extended spray mixing residence time. In this regard, Musculus et al. [13] presented illustrative analysis of UHC emissions; i.e., Figure 1.10 shows the dependence of UHC emissions on "*ignition dwell*," representing the time between the end of injection (EOI) and the start of

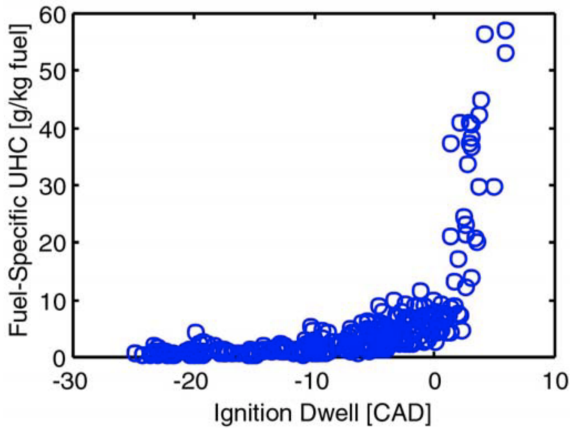

Figure 1.10: *UHC emissions for a wide span of engine operating conditions associated with ignition dwell [13]*

combustion (SOC); i.e., SOC-EOI. In extreme conditions where chemistry is very slow, ignition may begin after EOI, the ignition dwell becomes positive. In this case, the mixing-controlled combustion phase is lacking. As such, PPCI condition may likely be characterized by positive ignition dwell to some extent due to the delayed ignition and therefore extended spray mixing time. To correlate the positive ignition dwell and UHC emission in further detail, Musculus [13] hypothesized that the unburned mixture may be promptly mixed with excessive ambient air resulting in overly lean mixture out of flammable range; it may accordingly contribute to UHC emissions. This hypothesis was found to be inconsistent with his experimental study [60]. It is also noteworthy that Lachaux and Musculus [58] employed formaldehyde (CH_2O) fluorescence diagnostics for tracking UHC emissions because the formaldehyde shows the very similar dynamics to UHCs.

1.2.3 Combustion Recession

Recent literatures [13, 62, 63] have reported observation of *flashback*-like structure of soot luminosity (high temperature kinetics) after EOI certainly at conventional engine relevant conditions; i.e., HTC regime. Knowing that the term *flashback* classically refers to premixed flame propagation in gas-turbine studies, Skeen et al. [63]

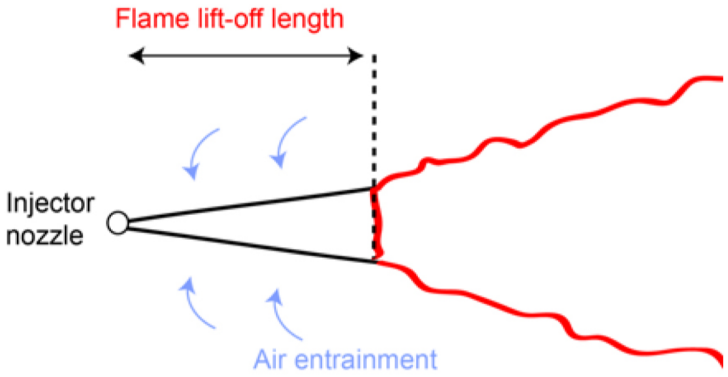

(a) *Quasi-steady lifted diesel spray flame before EOI*

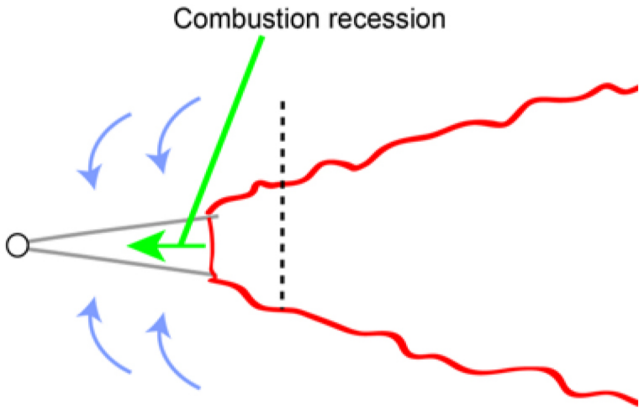

(b) *Occurence of combustion recession after EOI*

Figure 1.11: *Schematics of lifted diesel spray flame followed by combustion recession after EOI [61]*

claimed that this phenomena should not be considered "flashback" problem; instead, this chemical activity may reasonably be regarded as spontaneous ignition consuming unburned fuel molecules or low temperature intermediate species present upstream of lifted flame position as illustrated in Figure 1.11. As such, Knox and co-workers [61] adopted *combustion recession* as an appropriate term to describe this phenomenon. They demonstrated the correlation of ambient gas thermodynamic state with the likelihood of combustion recession over a wide span of conditions. Knox and Genzale [64] further explored different EOI transients significantly impacting on the combustion recession occurrence and found the potential use of this phenomenon as a UHC re-

duction technique under LTC relevant conditions. Upon the observation of decreased scalar dissipation rate after EOI simulated by Hu et al. [65], Knox postulated in his thesis [66] that turbulence-chemistry interaction (TCI) may be of less influence on the combustion recession occurrence. However, such a TCI effect on the combustion recession has not been fully demonstrated in multi-dimensional modeling approach to this date. Focusing on the dynamics of combustion recession, there have been no further extensive experimental or computational studies other than aforementioned literatures to the best of author's knowledge.

1.2.4 Ducted Fuel Injection (DFI)

Non-sooting combustion in diesel engines is known to be achievable in several ways; e.g., lean fuel-air charge combustion, use of oxygenated fuel, high injection pressure, small injector orifice, cooling ambient gas temperature, EGR and so on. The concept behind those techniques share the same goal; an enhancement of fuel-air mixing and accordingly lean mixture charge formation prior to partially premixed combustion phase where soot precursors start to form. To this end, increased mixing residence time and mitigated charge stratification level are prerequisite; i.e., lean lifted flame combustion (LLFC) is one such potential strategy as mixing-controlled combustion technique that may avoid soot forming process because it occurs at equivalence ratios less than approximately 2 [67].

Seeking a means of achieving more effective LLFC strategy, a new spray injection configuration, termed ducted fuel injection (DFI), has recently been invented by Mueller and co-workers [68, 69]. This concept of non-sooting technique was also recently examined under heavy-duty diesel engine conditions and proved its effectiveness in significant reduction of soot emissions [70]. The idea is that fuel spray is injected through a small duct installed at a nozzle offset distance (G) downstream of injector nozzle as illustrated in Figure 1.12. By doing so, the injected fuel travels

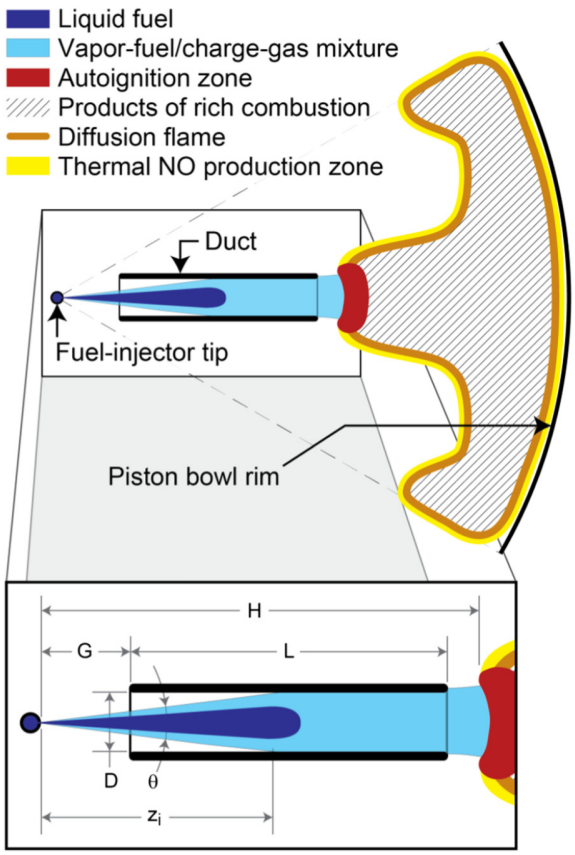

Figure 1.12: *Schematic of ducted fuel injection (DFI): a small cylindrical duct is equipped ahead of injector nozzle [69].*

through the small channel maintaining its axial momentum without being dragged down by ambient air entrainment; accordingly increased turbulent mixing through the duct channel may enhance premixing and potentially mitigate soot formation. They anticipated that the DFI technique could provide further several benefits in non-sooting diesel combustion. The presence of duct could limit over-mixing at the spray periphery and lead to cooler mixtures due to cold duct wall, resulting in less UHC/CO emissions and more premixed charge in favor of low soot level. Furthermore, the higher scalar dissipation rate (χ) potentially generated at duct exit could make it difficult for the premixed combustion to initiate at the duct outlet, thereby enabling secondary turbulent mixing with ambient air downstream of the duct exit.

Mueller and co-workers conducted initial proof-of-concept experiments on DFI and

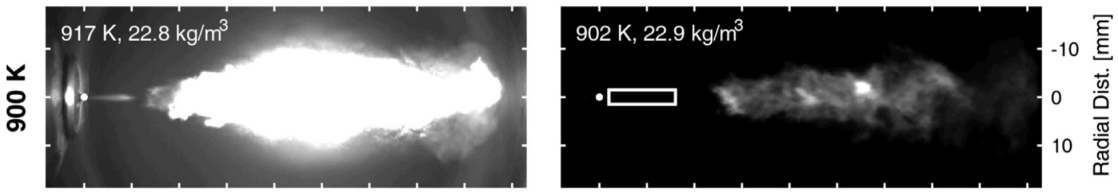

Figure 1.13: *Comparison between free-spray combustion (left) and DFI combustion (right) [69]: bright natural luminosity signal is an indicator of the presence of hot soot.*

demonstrated the potential benefits by using a constant-volume combustion vessel (CVCV) and one set of duct hardware (D = 3.0 mm, L = 14 mm, G = 2 mm as denoted in Figure 1.12), and spray flame was visualized by optical diagnostics of natural luminosity and OH* chemiluminescence. The features of more distanced lifted flame and non-sooting combustion are evidenced by hot soot incandescence within the combustion chamber as shown in Figure 1.13 as opposed to conventional free-spray combustion where high concentration soot luminosity is obvious.

Despite such a successful demonstration, Mueller et al. [69] and Fitzgerald et al. [70] were the preliminary investigations on feasibility of DFI concept. Full examinations of various DFI configurations, e.g., varying duct diameter and lengths and ambient gas conditions, have yet to be done. Thus, key knowledges of various parametric effects are still largely unknown. To further identify important physics behind this new concept, more experimental and computational studies need to be performed.

1.2.5 Diesel Engine Modeling

Multi-dimensional Computational fluid dynamics (CFD) simulations have been considered as an integral tool in the engine design sequence; however wide employment of the CFD analysis is a challenge due to high degree of non-linearity and multiscale physics governing the in-cylinder spray combustion processes. As such, adequate modeling approach accounting for predominant physics and feasibility of the model incorporation in engineering level framework of CFD tools should be properly inves-

tigated. Throughout the preceding sections, attentions to some important physics encountered in diesel engines have been drawn upon the demand for LTC engine design. In order to eventually be able to engage the attentions with a pathway towards advanced modeling methods, followings overview the literatures of spray modeling and combustion modeling in separate subsections. These reviews will help gain in-depth knowledges underpinning the physics of interest with several keyword emphasis.

1.2.5.1 Spray Atomization Modeling

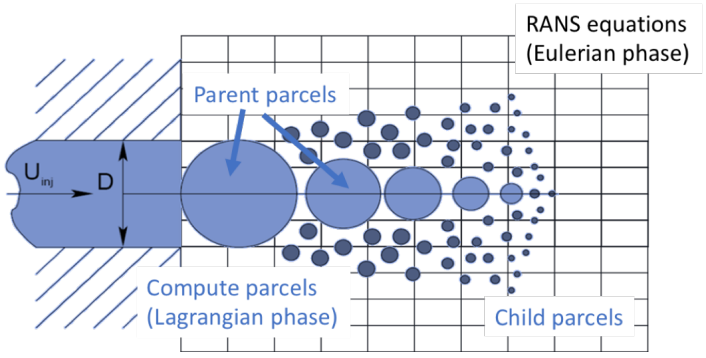

Figure 1.14: *Schemtic of Eulerian-Lagrangian (E-L) approach in spray modeling [71]; the blob injection method tracks individual computational parcels on Lagrangian coordinate.*

As per suggested importance of *atomization-controlled* spray under LTC-like conditions in section 1.2.1.1, this section outlines atomization models that have been popularly incorporated in Eulerian-Lagrangian (E-L) based engine CFD software. In this modeling framework, the Lagrangian discrete particle tracking method [71] is a preferred approach to describe a cloud of liquid particles, while the continuum gas phase flow is resolved by a set of relevant transport equations; e.g., Reynolds-Averaged Navier-Stokes (RANS) equations, on the Eulerian grid coordinate as depicted in Figure 1.14. The dynamics of droplet breakup is individually tracked down by adequate physics sub-models in the Lagrangian description. Following sections review underlying physics of the existing spray models and discuss potential sources of uncertainty.

Blob injection method

For diesel spray atomization modeling, Reitz and Diwakar [72] first introduced the *blob* injection method, which is more often called *parcel*; i.e., atomization is prescribed by injecting 'parcels' that have a size on the same order of nozzle diameter. Although the parcels conceptually represent the liquid jet which may undergo primary breakup process, their model assumes that the parcels break down in analogy to single droplet behavior under aerodynamic force impact identified by Reinecke and Waldman's experiment [73]; i.e., *bag* breakup and *stripping* breakup. The linearized breakup rate is then applied to the parcels at each CFD time step as described in Equation 1.1.

$$\frac{dr_p}{dt} = -\frac{r_p - r_c}{\tau_{bu}} \tag{1.1}$$

where τ_{bu} is breakup characteristic time considered as lifetimes of unstable droplet. (Readers are encouraged to find details of expressions in their original paper [72]) The r_p and r_c specify radius of the parent parcel and stable child parcel; r_c is then determined by $r_c = \sigma^2/2\rho_l|U_{lg}|\nu$. This model was designed to predict a intact core region near the nozzle where relatively large droplets are present; in other words, the model just updates parent parcel size dynamically; i.e., no child parcels considered, and accordingly the number of droplets represented by the parent parcel is recalculated to preserve the total mass at each time step. Reitz [74] addressed that the model prediction was found to disagree with fuel vapor measurements. However, this simple approach provided a common framework shared by subsequently proposed spray models in Lagrangian description.

Modeling aerodynamically induced breakup process

Reitz identified the deficiency of his first blob injection model as addressed above; this finding motivated him to modify his 'blob' injection model in order to accom-

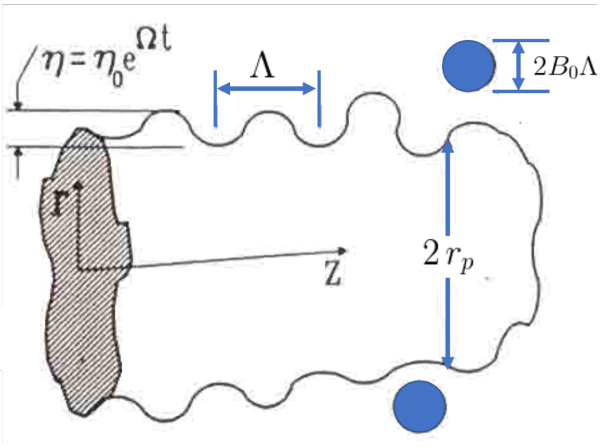

Figure 1.15: *Schemtic of Kelvin-Helmholtz (KH) instability wave growth on liquid jet surface [74]*

modate more adequate underpinning physics; i.e., aerodynamically generated Kelvin-Helmholtz (KH) wave growth on the liquid jet surface as depicted in Figure 1.15, based upon his earlier theoretical study [27]. The KH model essentially follows the same 'blob' breakup rate tracking method described by Equation 1.1; however the breakup characteristic time scale, τ_{bu}, and child parcel size, r_c, were greatly modified by the linearized solution of KH wave instability [74]. In this, so-called KH model, τ_{bu} and r_c are replaced by Equation 1.2 and Equation 1.3, respectively.

$$\tau_{KH} = \frac{3.726 B_1 r_p}{\Lambda_{KH}\Omega} \tag{1.2}$$

$$r_c = B_0 \Lambda_{KH} \tag{1.3}$$

where Ω and Λ_{KH} are the maximum growth rate and corresponding wavelength of the most unstable wave growing on the liquid jet surface. In contrary to the previous model, the KH model considers not only dynamically tracking parent parcels, but also creation of additional computational parcels representing primary breakup generated child droplets.

The KH model employs two primary empirical constants; i.e., breakup time con-

stant, B_1, and droplet size constant, B_0, which are typically calibrated by users to ensure better agreement with measured spray parameters of interest. Although many previous researchers have proposed optimized values for the constants to match their simulations with various experiment data, the value of B_1 in particular needed to range over a wide span; $1.76 \sim 40$ [75–77], whereas B_0 was typically set to 0.61 with acceptable success in predicting global spray characteristics. The need for empirically dependent and arbitrary calibrating job makes use of the model over a universal span of engine relevant conditions challenging.

Several follow-up studies [78–80] were encouraged by success of the KH model, which is relevant platform to deliver both primary and secondary breakup processes. In turn, multiple studies have combined the KH model with additional secondary breakup model; namely hybrid model. Su and co-workers [78] suggested KH-RT model that employs Rayleigh-Taylor (RT) instability theory for the child droplet breakup mechanism (secondary breakup) in addition to the KH breakup calculation (primary breakup). In their comparative analysis between KH (no secondary breakup) and KH-RT, the consideration of those consecutive breakup processes was found to be more predictive in terms of Sauter mean diameter (SMD) distribution in space, whereas solely used KH breakup in the model exhibited rather bimodal size distribution; lacking intermediate range of size. The KH-RT model is the most common default option for atomization model in most of today's engine CFD softwares, such as KIVA [81], Fluent [82], CONVERGE [83], and OpenFOAM [84].

Modeling nozzle flow induced breakup process

Most of the model validation studies until new advanced diagnostic techniques were developed in early 2000s relied primarily on shadowgraph method or phase-Doppler particle analysis (PDPA); the models were verified limitedly against measurements of, for example, spray penetrating length, spray jet spreading angle, and SMD farther

downstream of the nozzle, since measurements of flows inside or near the nozzle were extremely difficult due to the optically dense spray and high-speed flow characteristics. Therefore rigorous assessment of predictive capability of the primary breakup models in the near nozzle field was not possible.

X-ray radiography measurements [85–87] capable of quantifying the path-integrated liquid fuel mass in the optically thick region of spray became available for model validation study in mid 2000s. Som and Aggarwal [77] examined predictive capability of the KH-RT model by using x-ray radiography data [87] in the primary breakup region close to nozzle. Their study revealed that the model tends to underpredict mass dispersion evaluated at non-vaporizing conditions, which may be due to the absence of nozzle upstream (internal flow) effect on the breakup process. They postulated that such underpredicted mass distributions may be explained by the fact that the KH model assumption diminishes other potential impacts of internal nozzle flow dynamics, i.e., turbulent kinetic energy and thermodynamic state change, suggesting the need for further model development. As a result, the inclusion of additional primary atomization mechanisms was motivated.

Subsequent to KH model assessment, Som and his co-workers conducted further simulations [88, 89] that studied the impact of employed additional physics in their new model (KH-ACT model) on the predicted spray metrics extensively under non-vaporizing, vaporizing and reaction conditions. In an effort to link the internal nozzle flow development with the outstream spray, the KH-ACT model was an extended hybrid model on KH model basis; hence the model includes nozzle-generated turbulent flow effect and cavitation-induced breakup in addition to KH wave induced breakup as sketched in Figure 1.16. The turbulent breakup assumption was made on the basis of Huh-Gosman model formulation [90]. In this model, each of the breakup mechanisms is assumed to compete with others and emerge if corresponding breakup rate is superior than that of others. The right hand side of breakup rate relationship

in Equation 1.1 should therefore be reformulated as in Equations 1.4a and 1.4b.

$$\frac{dr_p}{dt} = -C_{T,CAV}\frac{L_A}{\tau_A} \tag{1.4a}$$

$$\frac{L_A}{\tau_A} = \max\left\{\frac{L_{KH}}{\tau_{KH}}, \frac{L_t}{\tau_t}, \frac{L_{CAV}}{\tau_{CAV}}\right\} \tag{1.4b}$$

where $C_{T,CAV}$ is the breakup rate calibration constant. Detailed description and formulations for individual breakup mechanisms are not repeated here; readers are encouraged to read the most representative literature of the KH-ACT model [89]. In this thesis, as per employed setup of test injectors, non-cavitating nozzle flow is to be discussed to fully characterize hydrodynamically driven mechanisms; aerodynamically induced breakup vs. nozzle-flow generated turbulence breakup. Thus, cavitating breakup is beyond the scope of the present study and neglected in the modeling platform of interest.

According to Som and Aggarwal's test results [89], using above formulation to account for multiphysics hybrid mechanism, the test metric of interest, e.g., spray dispersion, liquid/vapor length were found to be better captured by the KH-ACT model. However, predictions of the model were not universally successful across entire test conditions. Despite obvious improvement of the KH-ACT model, marginal improvements were obtained in capturing liquid and vapor penetrations in particular under very low ambient density conditions (ρ_g less than 7 kg/m^3) as shown in Figure 1.17.

In regard to the predictive capability of KH-ACT model, Magnotti [91] hypothesized that rather than aerodynamic breakup (KH), lacking accuracy in the turbulent breakup assumption may be responsible for the marginal improvement. The fact that lower ambient density condition tends to diminish aerodynamic shear stress on the liquid surface makes her hypothesis reasonable. To tackle this problem, she raised a

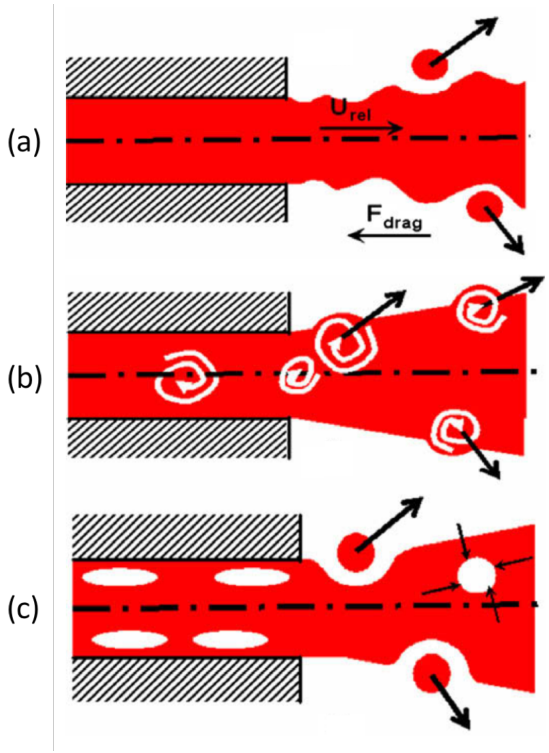

Figure 1.16: *Schematic representation of competing different primary breakup mechanisms. Follwoing three competing breakup mechanisms are incorporated in the KH-ACT hybrid model [89]; i.e. (a) Aerodynamically induced breakup based on KH model (b) The turbulence induced breakup based on Huh-Gosman model [90]. (c) The cavitation induced breakup.*

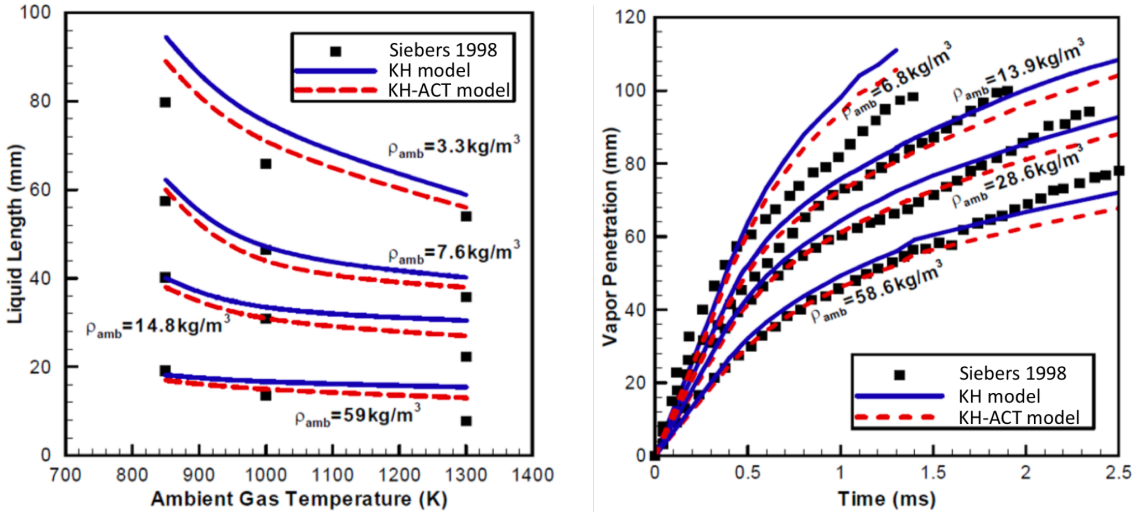

(a) *Liquid length* (b) *Vapor length*

Figure 1.17: *Comparison of predictive capability of two breakup models: KH model vs. KH-ACT model*

question on the child droplet scaling assumption of the model. Indeed, the turbulent breakup process in the KH-ACT model was assumed to create child parcel sizing in turbulent integral length scale of the internal nozzle turbulent flow. On the contrary, a body of theoretical studies by Wu and Faeth [29–31] supported the idea that turbulent eddies within *inertial subrange* must be responsible for the surface deformation and ligament protrusions forming droplets.

New primary atomization model: KH-Faeth

In an effort to make further improvement in turbulent breakup scaling, Magnotti [91] was recently motivated to put forth a new scaling method based on the KH-ACT modeling framework, suggesting to replace the turbulent characteristics length, L_t, and time, τ_t in Equation 1.4b with the new parameters derived from energy balance equations [29]. Since the model was inherited from the KH-ACT model, the KH-Faeth model can be considered as an another hybrid primary breakup model accounting for aerodynamic and turbulence effect in concept of competing multi-physics breakup mechanisms.

Recently, Magnotti [91] incorporated the KH-Faeth model in the commercially available CFD code, CONVERGE [83]. However, complete model verification with the new scaling strategy was not made yet to this date. In her study, the KH-Faeth model was once applied to simulate ECN [92] standard Spray-A injector to allow for validations at engine relevant conditions in terms of liquid length and relatively narrow span of SMD measurements with the aid of advanced x-ray diagnostics (USAXS). The test was not able to show promising improvement; the model showed worse prediction in SMDs than KH model and KH-ACT model. The reason of lacking accuracy was mainly because the employed conditions within availability at the time were not in favor of turbulent breakup dominating spray; somewhat high density, ρ_g, were considered such that aerodynamic effect was more likely to emerge over the

turbulence breakup. She performed numerous simulations to characterize the model prediction sensitivity to the spray parametric conditions, e.g., injection pressure and ambient density. However, it remains largely unknown whether the new scaling in the KH-Faeth model may apply to turbulent breakup relevant spray conditions.

1.2.5.2 Turbulent Combustion Modeling for Non-Premixed Flames

This section lays out turbulent combustion modeling strategies in regards to the physics of crucial importance discussed in preceding sections 1.2.1.3 and 1.2.3. One of the challenges encountered in diesel combustion modeling is the intrinsic complexity of the problems generally characterized by non-linear natures and multiscale physics. Such a complexity in reality barely makes direct simulation viable. Major difficulty in diesel combustion modeling has been identified by the turbulence chemistry interaction (TCI) problem, which acts as a essential role in diesel engine combustion dynamics. Therefore, it is very demanded to facilitate various ranges of TCI model strategies in engineering level CFD softwares.

A general mathematical framework for engine combustion modeling is largely based on mass-weighted averaged (called Favre average) Navier-Stokes (NS) equations. Using this averaging technique, the resulting balance equations may include several unclosed terms due to turbulent transport, which is mathematically formulated by non-linear and high order of moments of fluctuating scalars. Especially, mean reaction rate source term, $\overline{\dot{\omega}}_k$, where k denotes k-th species, in averaged species equations introduces numerous high order unclosed moments, which is numerically impossible to be integrated in CFD framework. Because of non-linearities, this reaction rate source term can also be a source of huge truncation errors when linearized model applies. Because of such a difficulty, reaction rate closures are generally derived from phenomenological simple analysis.

A specialty of turbulent non-premixed combustion modeling lies in the needs to

define mixture fraction, z, which locally measures the fuel/oxidizer ratio and defines boundaries conditions in non-premixed flame problems. It should also be noted that the mixture fraction is considered a passive scalar; by definition it is neither consumed nor produced by chemical reactions, thus it is transported only due to fluid dynamics transport phenomena. Due to this nature, the mean quantities of $\widetilde{z}$ and its variance, $\widetilde{z''^2}$, can easily be resolved by adding additional transport equations. In turn, it helps define statistical format of turbulent flow quantities by constructing a *probability density fuction* (PDF), $pdf(z)$. Accordingly, mean primitive variables, e.g., $\widetilde{Y_k}$ and $\widetilde{T}$, and reaction rate, $\overline{\dot{\omega}}_k$, can be conditionally averaged on mixture fraction space, and then the resultant turbulent mean quantities can be evaluated by first order moment of the scalar and the PDF function as expressed in Equations 1.5 [93]:

$$\overline{\rho}\,\widetilde{Y_k} = \int_0^1 \left(\overline{\rho\, Y_k|z}\right) pdf(z)dz \tag{1.5a}$$

$$\overline{\rho}\,\widetilde{T} = \int_0^1 \left(\overline{\rho\, T|z}\right) pdf(z)dz \tag{1.5b}$$

$$\overline{\dot{\omega}}_k = \int_0^1 \left(\overline{\dot{\omega}_k|z}\right) pdf(z)dz \tag{1.5c}$$

Poinsot and Veynante [93] defined two categories that non-premixed combustion modeling techniques may fall within depending on whether the species and energy balance equations are required; (1) *primitive variable method* and (2) *reaction rate approach*. In the primitive variable method, those primitive variables are not directly resolved through their balance equations. The classification can be further specified with consideration of chemical characteristic time scale; equilibrium vs. non-equilibrium. The equilibrium chemistry may simply need algebraic solution of reactive scalars, whereas the non-equilibrium chemistry yields the need of finite-rate chemistry with detailed chemical kinetics solution. Following sections summarize various range of turbulent

Table 1.1: *Classification of turbulent non-premixed combustion models [93]*

	Equlibrium (fast chemistry)	**Non-equilibrium (finite rate chemistry)**
Primitive variable method	Burke-Schumann [94]	CMC [95] Flamelet by Peters [42] RIF [96]
Reaction rate approach	EDM [97]	WSR (no model) CTC [98], PaSR [99],

combustion models in these classification as categorized in Table 1.1.

Primitive variable method

As the name implies, the *primitive variable method* is to update conditionally averaged scalars in Equations 1.5a and 1.5b through independent flame solution libraries (e.g. flamelet solution) or by solving additional balance equations. In the former case, species and energy equations are not generally considered; accordingly, determination of the mean reaction rate source terms is not necessary. The latter case, however, often requires additional reduced order source term modeling as will be discussed in the conditional moment closure (CMC) model later. This primitive variable method may obviously benefit from less computational load in absence of reaction source term evaluation, which otherwise requires very stiff ordinary differential equation (ODE) solution.

In 1928, Burke and Schumann [94] published very first theoretical description of the laminar diffusion flame structure by the assumption of laminar flow and irreversible infinitely fast chemistry (reaction sheet approximation: $Da \gg 1$). This classical approach has served an extremely straightforward approximation for counterflow mixing and diffusion flame. Earlier attempts to perform CFD simulations with Burke-Schumann flame model began in early 1990s by Mawid [100] and Park

and Aggarwal [101]. However, this approach was only able to reproduce a "steady" laminar spray flame due to the fast chemistry extreme.

Assuming infinitely fast chemistry is clearly inadequate in most of spray flame applications; thus, incorporating finite rate of chemistry into TCI models is preferred for diesel combustion modeling. Although the conditional moment closure (CMC) model has been categorized in the primitive variable method in the fact that mean species and energy equations are not resolved, the model requires additional balance equations for conditional species mass fractions, $\left(\overline{\rho Y_k|z}\right)$. This allows to include detailed chemistry to account for finite rate chemistry by high-order moments unclosed source terms. Usually, the closure of the source terms is made at the first conditional moment (reduced order source term modeling). Knowing that this approach requires balance equations for all conditional reactive scalars, additional equations are also needed for different mixture fraction, z, levels [95]. Moreover, a description of the probability density function is needed in principle; thus, CMC model may belong to the category of presumed PDF method. Due to its flexibility in unsteady non-equilibrium chemistry, the CMC model has been successfully employed over a reasonable span of diesel engine conditions [102–104]. Nevertheless, the CMC model may lead to very high computational costs since a huge number of conditional scalars and multilevel mixture fractions should be retained [105, 106].

Improved computational efficiency may be obtained by reducing number of balance equations in CFD framework. Unlike the CMC model, flamelet model approach does not necessitate to solve transport equations for all reactive scalars. Instead, a single conserved scalar, i.e., mixture fraction z, is needed to be transported by CFD methodology. By transforming three-dimensional nature of the balance equations into a one-dimensional reaction space, the flamelet model leverages a separate chemistry solution independent of CFD solution, such that it may significantly reduce the computational cost associated with highly demanded numerical algorithm for partial

differential equation (PDE) integrations. The first flamelet model was proposed by Peters [42] based on the laminar flamelet concept [107], which views a turbulent diffusion flame as an ensemble of locally undisturbed laminar diffusion flamelets. The key principle of the flamelet model is to construct a one-dimensional laminar flamelet equation in a reaction space, i.e., mixture fraction, z. From the coordinate transformation, the resulting balance equations for species mass fraction in one-dimensional reaction space (flamelet) is formulated in Equation 1.6.

$$\rho\frac{\partial Y_k}{\partial t} = \dot{\omega}_k(z) + \frac{1}{2}\rho\chi\frac{\partial^2 Y_k}{\partial z^2} \tag{1.6}$$

It is noteworthy that the flamelet equation includes a reaction source term, $\dot{\omega}_k$, and diffusive mixing term coupled with scalar dissipation rate, χ. It is also beneficial to not include non-linear convection term; thus, it is numerically stable to solve. In principle, the reaction source term as a function of z can essentially incorporate finite rate chemistry with detailed mechanisms, and the scalar dissipation rate involves local turbulent intensity in correlation with stretched flame as discussed in Section 1.2.1.3.

The original flamelet approach by Peters [42] was initially appreciated as the steady laminar flamelet model (SLFM) by the underlying assumption that the scalar dissipation rate varies slowly enough to omit the time dependent term. Earlier studies [108, 109], however, addressed the importance of time dependent flame structure, and observed that the SLFM approach failed to predict extinction and re-ignition processes. Pitsch and co-workers [110] also emphasized the importance of unsteady effects on slow chemical kinetics, such as in the formation of nitrogen oxides (NOx). In this regard, the representative interactive flamelets (RIF) [96] model put forth better platform as an efficient primitive variable method. The RIF model runs a stand-alone flamelet solver, which communicates dynamically with the CFD solver and builds a dynamic library of reactive scalar solutions at each CFD time step. A nominal scalar dissipation rate in the reaction space is determined based on conditional averaging

over the stoichiometric condition to account for local turbulent mixing intensity. To finally construct turbulent mean flame brush, the resolved solution is then integrated with a presumed PDF as described in Equations 1.5.

As a well-validated and computationally efficient approach, the RIF model has been widely applied to a broad range of diesel engine applications; e.g., flame stabilization and pollutant emissions [111, 112], and low-temperature combustion conditions [113]. Predictive capability of the RIF model has been more refined by the multiple flamelet approach [114]; so-called, multiple flamelets RIF. In this approach, more than one flamelet libraries are defined with independent pseudo time variable; so, each of libraries is representative of different history of turbulent mixing and ignition. A thorough investigations on the RIF model have been made in terms of prediction accuracy and computational efficiency against available experimental data to this date. Kim and co-workers [115] implemented the multi-flamelets RIF model into the KIVA [81] and validated the model against measurements of engine dynamics and NOx and soot emissions. Gauding and co-workers has also demonstrated applicability of the RIF model and their modified RIF model in multiple-injection strategy [116]. More recently, several literatures [117–119] have extensively presented comparative analysis between the RIF model and detailed chemistry based direct integration model, namely well-stirred reactor (WSR) model. They commonly demonstrated well-captured turbulent flame brush comparable to experiment by using the RIF model. However, predictions of ignition delay and flame lift-off length (LOL) by both models were found to be rather consistent or in marginal difference, suggesting that more comprehensive test metric may be required for better assessment of the models.

Reaction rate approach

Unlike the models described previously, general balance equations for species and energy are solved in the reaction rate approach. Accordingly any closure for the reaction source terms, $\overline{\dot{\omega}}_k$, are needed as a form of Arrhenius formulation or modeled as in Equation 1.5c. In the former case, i.e., Arrehenius form integration, computationally intensive effort should be dedicated because of non-linear and high-order moments of fluctuating quantities which are generated through the averaging technique. As such, general approach towards this method is based on linearized quasi-steady assumption of chemical reaction or simple scale analysis.

The simplest model generally assumes a one-step global reaction representing conversion from stable reactants to equilibrium products, neglecting complex chemical reaction steps and intermediate species. Such an assumption of omitting detailed reaction steps can be justified when turbulent mixing scale is greatly larger than the representative chemical time scale ($Da \gg 1$), so the burning rate of mixture is predominantly determined by the rate of mixing. In this case, turbulent mixing time scale can be considered as a primary controlling factor in the mean reaction rate. Therefore, instead of integrating Arrhenius formulation, the term, $\overline{\dot{\omega}}_k$ may reasonably be simplified to be inversely proportional to characteristic turbulent mixing time scale, $\tau_{c,m}$. In this regard, eddy breakup (EBU) model was proposed to estimate the mixing-controlled fuel burning rate, $\overline{\dot{\omega}}_{fuel}$, by Spalding [120] as the first mixing-controlled model. Later, the EBU model was extended to eddy dissipation model (EDM) to be applied for non-premixed turbulent combustion [97].

The mixing-controlled combustion model may be acceptable for quasi-steady spray flame after ignition. However, the ignition generally initiates by low temperature intermediate species and does not immediately takes place (i.e., slow chemistry); the ignition should therefore be either separately modeled or integrated into the detailed chemistry. Concerning the former approach, very early generation of diesel engine

CFD studies used multistep "Shell" ignition model developed by Halstead [121] in order to treat low temperature autoignition. To account for high-temperature combustion phase, Reitz and Bracco [122] proposed characteristics time scale combustion (CTC) model as an extended version of EDM model. The CTC model allows to consider finite rate chemistry by taking the chemical time scale, τ_{chem}, into consideration as a part of the characteristic time scale; i.e., $\tau_{c,m} = \tau_{chem} + \tau_{mix}$. The Shell ignition model was then combined with the CTC model, namely Shell-CTC model, to accommodate consecutive ignition and mixing controlled combustion and was shown to provide acceptable prediction accuracy [123, 124]. Nevertheless, the limitation of using single characteristics time is obvious since it is likely that all participant species may have different rate at which they proceed towards equilibrium. In this regards, further improved prediction accuracy was obtained by multi-time scale combustion model [125] and dynamically adjusted mixing time scale by reaction progress variable [126], suggesting that the use of detailed kinetics may be more crucial for predictive model development. However, applying detailed kinetics for engine combustion modeling was considered computationally prohibitive until late 1990s.

Knowing that both ignition and mixing-controlled combustion can be treated through the detailed kinetics, the CTC type combustion model can be extended to more refined TCI model by straightforwardly employing detailed kinetics. The partially stirred reactor (PaSR) model [99] can therefore be grouped into this category allowing for suitably captured ignition, flame stabilization and emission predictions [127]. In the PaSR model, a computational cell is *conceptually* split into two different zone; i.e., one with homogeneous reactor and another one with fresh mixture. Unlike in the CTC model, the reaction progress variable is defined from the law of mass action estimated by detailed rate coefficients for each of reaction steps, and the mixing time scale is approximated to Kolmogorov time scale [99].

The well-stirred reactor (WSR) is another straightforward approach for detailed

kinetics to be used in combustion modeling, and often named as well-mixing model, direct integration method, and non-TCI model by other authors. As the "non-TCI" indicates, this approach does not account for mixing-controlled chemistry; rather it utilizes a direct integration method to evaluate mean reaction rates, $\overline{\dot{\omega}}_k$ without modeling higher-order moments. The basic principle behind this modeling approach is an assumption of infinitely fast mixing compared to chemical reaction timescales, such that the species within each computational cell are assumed to be homogeneously distributed. The mean reaction rate is then computed directly from an Arrhenius law formulation as a function of mean scalars. In practical turbulent combustion applications, however, this approximation may be very inaccurate, with errors of up to several orders of magnitude arising due to the highly non-linear nature of turbulent reaction rates. Nevertheless, this type of moment method has often been used in engine numerous CFD simulations to date [128, 129]. Very extensive assessment on the WSR modeling approach has been made by many literatures. D'Errico and co-workers addressed that despite non-TCI considered, the WSR model can be relatively predictive if fine mesh resolution is allowed. Also, the WSR model moderately predicted the general diesel combustion test metric better than by EDM model. Another recent study of them [119] emphasized that the WSR model may be useful for engine conditions where the homogeneous mixture assumption may apply. Lucchini and co-workers [129] also mentioned that prediction accuracy of the WSR model strongly correlates with the choice of kinetic mechanism. On the other hand, a major drawback of the WSR model was revealed by the overestimation of heat release rate pertaining to very thin turbulent flame brush due to neglected TCI effect [119].

1.2.6 Research Keywords in Summary

Engineering solutions of complex fuel injections and turbulent combustion problems in diesel engines have been greatly aided by the success of engine CFD sub-model de-

velopment over the last few decades. However, continuous success of the existing CFD sub-models may be questionable as the new engine techniques, e.g., LTC, increasingly draw our attention to undiscovered engine operating conditions. Nonetheless, the adequate choice of sub-models as well as new model development can be made according to comprehensive understandings of the physics representing the engine conditions of new interest. To this end, previous sections presented several keywords of physics identified along the LTC operating condition as highlighted in *italics* in the following summary; these research keywords are to be used to guide model assessment and ultimately determine pathways towards improving the CFD sub-physics models.

- As engine operating conditions transition to LTC regime, fuel spray more likely undergoes *atomization-dominated spray* rather than diffusion-dominated spray;
- hence contribution of spray *primary breakup* to mixture formation should be considerable,
- and nozzle generated *turbulence breakup* emerges more than aerodynamically-induced breakup due to increased liquid-gas density ratio, $\rho_{\mathrm{L}}/\rho_{\mathrm{g}}$.
- By advancing injection timing, *ignition delay (ID)* and *flame lift-off length (LOL)* are elongated;
- accordingly *turbulent mixing* with ambient air is sustained longer; i.e., increase in mixing residence time.
- The autoignition is also determined by local *scalar dissipation rate*, which is critical in ignition and quenching phenomena of local *laminar flamelet*.
- The role of *low temperature kinetics* and *finite rate chemistry* may significantly contribute to flame stabilization and *unburned hydrocarbons (UHC)* emissions that mainly originates upstream of LOL.

- *Combustion recession* can therefore be used as a UHC reduction technique by controlling *end-of-injection (EOI)* transient.
- Also, the combustion recession was found to be spontaneously igniting flame kernels and correlated with *air entrainment* during EOI transient.
- *Soot emissions* start to form in the fuel-rich *partially-premixed combustion* flame, which is generally stabilized at LOL distance away from the injector;
- therefore, *lean lifted-flame combustion (LLFC)* is in favor of non-sooting flame condition.
- And the LLFC can be obtained by enhancing local turbulent intensity, i.e., scalar dissipation rate level, upstream of LOL.
- In an effort of achieving LLFC, *ducted fuel injection (DFI)* has recently been introduced in order to enhance turbulent mixing prior to ignition.

It is noteworthy that different keywords representing each of various physics are potentially associated with each other. For example, the nature of ignition involves low-temperature kinetics, finite rate chemistry, and local scalar dissipation rate level, and eventually determines LOL and UHC emissions. The soot emission is strongly related to LOL level and fuel-rich partially-premixed combustion flame, which can be mitigated by enhancing upstream scalar dissipation rate level. Above all, from the beginning of entire process, the rate of spray atomization may alter the progress of mixing, determining major characteristics of combustible mixture state and consequently flame stabilization and emissions in the end; thus, many of the keywords in this discussion are in comprehensive relationships pertaining to spray combustion problems of LTC diesel engines. The coupled physics should therefore be taken into account to enhance predictive capability of the engine CFD modeling. Towards the end goal, it is essential to identify lacking physics in the conventional models from the

perspective of the keywords discussed here; then the gap needs to be properly filled in the new modeling approach and the choice of CFD sub-models in diesel engine simulations.

1.3 Research Objectives

Predictive engine simulations may still remain in questions due to lacking physical representation in the existing sub-models in today's engine CFD tool packages. Thus, the central aim of this thesis is to identify lacking physics in the common modeling approach, and then ultimately seeks to find better answers for predictive modeling pathways towards LTC engine design. The major objectives outlined in this thesis are threefold: 1) provide a validation of the multi-physics related spray primary breakup models, and propose a new advanced spray model, and 2) validate the aspects of previously discussed keywords in the employed TCI models and elucidate the challenges in capturing unsteady combustion dynamics, and 3) lastly provide fundamental insights into new diesel engine combustion test metrics (i.e., combustion recession and DFI lifted flame) with consideration of TCI model application. Specific research objectives are addressed within different research interests as provided below:

Multi-physics primary atomization modeling

- Examine validity of recently proposed hybrid primary breakup model (i.e., KH-Faeth) fully examined under various range of ambient thermodynamic conditions with aid of recently developed droplet sizing techniques using x-ray diagnostics.

- Propose a new hybrid primary breakup model that can address multi-physics mechanisms; i.e., turbulence induced breakup, aerodynamically-enhanced turbulence breakup and merged primary and secondary breakup mechanisms.

- Provide further detailed insights into the nozzle-generated primary breakup modeling strategies and its impact on predicted spray structures. Elucidate further considerations that need to be addressed in the future advanced spray modeling approach.

Turbulence-chemistry interaction (TCI) modeling

- Provide comparative analysis on direct integration method (WSR) versus runtime based unsteady flamelet (RIF) modeling in capturing general diesel combustion dynamics, and sub-grid scale ignition kernels observable during combustion recession. Discuss the predicted spray flame structure in terms of turbulent flame intermittency and local turbulent mixing intensity.

- Verify the keywords employed in the RIF modeling against the non-TCI model (WSR); thus identify validity of the RIF model assumptions and discuss a possible pathway toward model improvement in simulating unsteady diesel combustion dynamics.

Effect of turbulent mixing on lifted spray flame

- Provide physical insights into combustion recession phenomena and its correlation with end-of-injection transient.

- Evaluate experimentally observed soot reduction technique using ducted fuel injection (DFI) strategy and further support the effect of locally enhanced turbulent mixing on the lean lifted-flame combustion (LLFC) and consequent result of non-sooting flame.

CHAPTER 2

METHODS

In the works presented in this thesis, two different CFD softwares; i.e., i) conventionally available CFD software, CONVERGE v2.2.0 [83] developed by Convergent Science, and ii) C++ object oriented programming (OOP) based open-source CFD toolkit, OpenFOAM v4.1.0, [84] were used to simulate diesel spray and combustion dynamics. For the use of OpenFOAM, the author identified major defects and debugging issues in the original source packages; thus, a separate C++ source library for spray and combustion modeling, namely GTFOAM, has been developed by the author. The following sections describe general CFD methodologies and sub-physics model formulations implemented in both softwares.

2.1 Multiphase Flow Modeling

In engineering research level studies for multi-scale multiphase flows, general methodologies of computational models for separate phases are incorporated in different system of coordinates; i.e., Eulerian coordinate for continuum phase and Lagrangian coordinate for dispersed phase. Such a combination of different coordinate systems is termed Eulerian-Lagrangian (E-L) method. Due to renown computational efficiency and relevance of physical representation, the majority of direct injection engine CFD modelings have been formulated in this framework; i.e., the turbulent gas flow can be described as a continuum phase in the Eulerian manner by using a set of balance equations, while the dispersed liquid phase can then be modeled in the Lagrangian manner.

2.1.1 Gas-Phase Governing Equations

In this section, the approach of Reynolds-averaged Navier-Stokes (RANS) equations for modeling turbulent flows and required closured models used in this study are briefly described.

2.1.1.1 Reynolds-Averaged Navier-Stokes (RANS) equations

General balance equations for the turbulent mean quantities are obtained by taking average of the instantaneous balance equations based on Reynolds decomposition, which is a general mathematical technique used to split any turbulent instantaneous scalars, q, into the expectation (mean) value and its fluctuations; i.e., $q = \overline{q} + q'$.

In many applications of variable density flows (e.g., reacting flows), however, the simple Reynolds averaging technique introduces many other double correlations involving density fluctuation and any turbulent scalars (e.g., $q\,\overline{\rho' q'}$) resulting in additional undesired closure problems [130]. To eliminate such a modeling huddle, Favre averaging is usually preferred; i.e., quantities are weighted by instantaneous density before averaging; $\widetilde{q} = \overline{\rho\, q}/\overline{\rho}$, and any flow quantity q may be expressed in terms of its Favre averaged quantity and fluctuation: $q = \widetilde{q} + q''$ with $\widetilde{q''} = 0$. Using this averaging technique, the Favre averaged balance equations for mass, momentum, chemical species, and sensible enthalpy may be formulated in conservative form as followings:

$$\frac{\partial \overline{\rho}}{\partial t} + \frac{\partial \overline{\rho}\widetilde{u}_j}{\partial x_j} = \dot{\rho}_s \tag{2.1}$$

$$\frac{\partial \overline{\rho}\widetilde{u}_i}{\partial t} + \frac{\partial \overline{\rho}\widetilde{u}_i\widetilde{u}_j}{\partial x_j} = -\frac{\partial \overline{p}}{\partial x_i} + \frac{\partial}{\partial x_j}\left(\overline{\tau}_{ij} - \overline{\rho}\widetilde{u_i'' u_j''}\right) + F_{s,i} \tag{2.2}$$

$$\frac{\partial \overline{\rho}\widetilde{Y}_k}{\partial t} + \frac{\partial \overline{\rho}\widetilde{u}_j\widetilde{Y}_k}{\partial x_j} = -\frac{\partial}{\partial x_j}\left(\overline{\rho V_{k,j} Y_k} + \overline{\rho}\widetilde{u_j'' Y_k''}\right) + \overline{\dot{\omega}}_k + \dot{\rho}_{s,k} \quad \text{for} \;\; k = 1, N_{spc} \tag{2.3}$$

$$\frac{\partial \overline{\rho}\widetilde{h}_s}{\partial t} + \frac{\partial \overline{\rho}\widetilde{u}_j\widetilde{h}_s}{\partial x_j} = \overline{\dot{\omega}}_T + \overline{\frac{Dp}{Dt}} + \frac{\partial}{\partial x_j}\left(\overline{\lambda\frac{\partial T}{\partial x_j}} - \overline{\rho u_j'' h_s''}\right) - \frac{\partial}{\partial x_j}\left(\overline{\rho\sum_{k=1}^{N} h_{s,k}Y_k V_{k,j}}\right) + \overline{\tau_{ij}\frac{\partial u_i}{\partial x_j}} + H_s \tag{2.4}$$

where V_k is the diffusion velocity of species k, and $\overline{\tau}_{ij}$ is mean viscous stress tensor estimated by Boussinesq approximation as:

$$\overline{\tau}_{ij} = \left(\mu' - \frac{2}{3}\mu\right)\frac{\partial \widetilde{u}_k}{\partial x_k}\delta_{ij} + \mu\left(\frac{\partial \widetilde{u}_i}{\partial x_j} + \frac{\partial \widetilde{u}_j}{\partial x_i}\right) \tag{2.5}$$

Here, μ is molecular dynamic viscosity estimated by a separate transport property model, and μ' represents the bulk (dilatational) viscosity, which is generally set to zero assuming monatomic gas molecules for most practical cases. The mean reaction rate of species k, $\overline{\dot{\omega}}_k$ in Equation 2.3, will be later described in terms of turbulent combustion modeling. The Lagrangian net energy transport by pressure work in Equation 2.4 can be reformulated in conservative form again:

$$\overline{\frac{Dp}{Dt}} = \frac{\partial \overline{p}}{\partial t} + \overline{u_i\frac{\partial p}{\partial x_i}} = \frac{\partial \overline{p}}{\partial t} + \widetilde{u}_i\frac{\partial \overline{p}}{\partial x_i} + \overline{u_i''\frac{\partial p}{\partial x_i}} \tag{2.6}$$

To incorporate multiphase flow correlation, each of balance equations contains spray induced source term denoted by *subscript s*, which will be discussed later.

2.1.1.2 Turbulent Closure Problems

Meanwhile, the averaged balance equations require closure rules for the unknown quantities (turbulent fluxes) represented by covariance (also called second order moment) of two fluctuating quantities such as Reynolds stress ($\widetilde{u_i''u_j''}$), turbulent fluxes of species ($\widetilde{u_i''Y_k''}$) and enthalpy ($\widetilde{u_i''h_s''}$). In general, the turbulent momentum flux (Reynolds stress) is resolved by a separate turbulence model. Other turbulent scalar fluxes q (e.g., species and enthalpy) are closed by a turbulent scalar gradient assump-

tion in Equation 2.7 for simplicity.

$$\overline{\rho}\widetilde{u_i''q''} = -\frac{\mu_t}{Sc_t}\frac{\partial\widetilde{q}}{\partial x_i} \tag{2.7}$$

where the turbulent viscosity μ_t is provided by a turbulence model, and the turbulent Schmidt number Sc_t defining the ratio between eddy viscosity and eddy diffusivity is kept in unity for all simulations in this thesis.

Several unclosed terms in above equations may often be neglected against turbulent transport, assuming a sufficiently high turbulence level. This may apply to laminar diffusive fluxes for species $\overline{\rho V_{k,j} Y_k}$ in Equation 2.3 and enthalpy $\overline{\lambda\,\partial T/\partial x_j}$ in Equation 2.4, as well as pressure-velocity correlation $\overline{u_i''\partial p/\partial x_i}$ in Equation 2.6. Nevertheless, the laminar diffusive fluxes for scalars are retained in the CFD codes employed for this study, and the terms are modeled by the following approximations:

$$\overline{\rho V_{k,i} Y_k} = -\overline{\rho}\overline{\mathcal{D}}_k\frac{\partial\widetilde{Y}_k}{\partial x_i} \tag{2.8}$$

$$\overline{\lambda\frac{\partial T}{\partial x_i}} = \overline{\lambda}\frac{\partial\widetilde{T}}{\partial x_i} \tag{2.9}$$

where $\overline{D}_k$ and $\overline{\lambda}$ denote mean species molecular diffusion coefficient and mean thermal diffusivity, respectively.

As aforementioned, the turbulent viscosity μ_t is provided by a separately defined turbulence model; in turn the Reynolds stress tensor can be estimated by the eddy viscosity concept for Newtonian fluids:

$$\overline{\rho}\widetilde{u_i''u_j''} = -\mu_t\left(\frac{\partial\widetilde{u}_i}{\partial x_j} + \frac{\partial\widetilde{u}_j}{\partial x_i} - \frac{2}{3}\delta_{ij}\frac{\partial\widetilde{u}_k}{\partial x_k}\right) + \frac{2}{3}\overline{\rho}k\delta_{ij} \tag{2.10}$$

where turbulent kinetic energy is expressed by

$$k = \frac{1}{2}\widetilde{u_k'' u_k''} \tag{2.11}$$

Here the role of turbulence model is to evaluate the turbulent viscosity μ_t. To this end, this study employs a standard *two-equations* model called k-ϵ model that provides descriptions of turbulent kinetic energy (k) and turbulent energy dissipation rate (ϵ) by means of additional balance equations. Using resolved quantities of k and ϵ, the turbulent viscosity is estimated as:

$$\mu_t = \overline{\rho} C_\mu \frac{k^2}{\epsilon} \tag{2.12}$$

The balance equations for k and ϵ are incorporated in conservative form as formulated below:

$$\frac{\partial \overline{\rho} k}{\partial t} + \frac{\partial \overline{\rho} \widetilde{u}_j k}{\partial x_j} = \frac{\partial}{\partial x_j}\left[\left(\mu + \frac{\mu_t}{\sigma_t}\right)\frac{\partial k}{\partial x_j}\right] + P_k - \overline{\rho}\epsilon \tag{2.13}$$

$$\frac{\partial \overline{\rho} \epsilon}{\partial t} + \frac{\partial \overline{\rho} \widetilde{u}_j \epsilon}{\partial x_j} = \frac{\partial}{\partial x_j}\left[\left(\mu + \frac{\mu_t}{\sigma_\epsilon}\right)\frac{\partial \epsilon}{\partial x_j}\right] + C_{\epsilon 1}\frac{\epsilon}{k}P_k - C_{\epsilon 2}\overline{\rho}\frac{\epsilon^2}{k} \tag{2.14}$$

where,

$$P_k = -\overline{\rho}\widetilde{u_i'' u_j''}\frac{\partial \widetilde{u}_i}{\partial x_j} \tag{2.15}$$

The Reynolds stress tensor $\overline{\rho}\widetilde{u_i'' u_j''}$ appears in the source term P_k given by Equation 2.15; thus it can be determined by the eddy viscosity relationship in Equation 2.10. The default model constants used in this study are listed below:

$$C_\mu = 0.09\ ,\ \ \sigma_k = 1.0\ ,\ \ \sigma_\epsilon = 1.3\ ,\ \ C_{\epsilon 1} = 1.44\ ,\ \ C_{\epsilon 2} = 1.92 \tag{2.16}$$

2.1.1.3 Passive Scalar Transport

Several modeling features of the most CFD codes requires to transport passive (or conserved) scalars. The core assumption of so-called *passive scalar analysis* is that the quantities of scalars are transported by the flow transport phenomena due to only convection and diffusion but not chemical reaction; thus they are conserved throughout the flow field and do not affect the solution of other quantities in the flow (e.g., mass, momentum, energy and other scalars). The passive scalar concept allows to greatly simplify the solution of reacting flow problems, especially involving non-premixed combustion or soot modeling.

Knowing that chemical elements are conserved in nature, one can limit the discussion to *mixture fraction* z as a best representative passive scalar. In principle, the mixture fraction measures the mass fraction of fuel mass in the mixture. In chemically reacting flows, however, the quantity of fuel is not conserved due to fuel molecule break-down; the mixture fraction is no longer passive scalar in such cases. Instead, alternate definition of the mixture fraction can be constructed using atomic elements conservation rule, which yields conserved l-th element mass fraction, Z_l, in the mixture:

$$Z_l = \sum_{k=1}^{N_{spc}} Y_k \frac{N_{l,k} W_l}{W_k} \tag{2.17}$$

where W_l and W_k are molecular weights of l element (atom) and k-th species, respectively and $N_{l,k}$ denotes the number of l element in the k-th species. For reacting flame burning hydrocarbon fuel, the element mass fraction of carbon (C) and hydrogen (H), denoted as z_{CH}, can be constructed as:

$$z_{CH} = Z_C + Z_H \tag{2.18}$$

The quantity of z_{CH} may be normalized by the values in the fuel stream (F) and

oxidizer (O) stream, yielding mixture fraction z as in Equation 2.19, such that it constructs boundary conditions: $z = 1$ in the fuel stream and $z = 0$ in the oxidizer stream for non-premixed flames.

$$z = \frac{z_{CH} - z_{CH}^{O}}{z_{CH}^{F} - z_{CH}^{O}} \tag{2.19}$$

Knowing that the passive scalar is conserved by flow transport phenomena, i.e., convection and diffusion, a general iinstantaneous transport equation for mixture fraction z can be constructed as:

$$\frac{\partial \rho z}{\partial t} + \frac{\partial \rho u_j z}{\partial x_j} = \frac{\partial}{\partial x_j}\left(\rho \mathcal{D} \frac{\partial z}{\partial x_j}\right) \tag{2.20}$$

Taking Favre average of above equation yields:

$$\frac{\partial \overline{\rho}\widetilde{z}}{\partial t} + \frac{\partial \overline{\rho}\widetilde{u}_j\widetilde{z}}{\partial x_j} = \frac{\partial}{\partial x_j}\left(\overline{\rho \mathcal{D} \frac{\partial z}{\partial x_j}}\right) - \frac{\partial}{\partial x_j}\left(\overline{\rho}\widetilde{u_j'' z''}\right) \tag{2.21}$$

Here, the first and second terms on the right hand side of the Equation 2.21 represent molecular transport and turbulent mixing transport, respectively. The molecular transport term can be linearized by averaging technique as in Equation 2.8. It is also general practice in turbulent flow to apply the gradient transport assumption for the turbulent transport term:

$$-\widetilde{u_j'' z''} = \mathcal{D}_t \frac{\partial \widetilde{z}}{\partial x_j} \tag{2.22}$$

where the turbulent diffusivity $\mathcal{D}_t$ is determined with presumed turbulent Schmidt number Sc_t and turbulent viscosity μ_t provided by the turbulence model:

$$\mathcal{D}_t = \frac{\mu_t}{\overline{\rho} Sc_t} \tag{2.23}$$

As addressed previously, in high Reynolds turbulent flow configurations, the molec-

ular transport (laminar diffusive fluxes) is relatively negligible compared to turbulent transport. Nevertheless, the term is included in the GTFOAM library, but neglected in CONVERGE code [83].

2.1.2 Liquid-Phase Governing Equations

Fully resolving liquid phase spray behavior in Eulerian description is considered computationally prohibitive due to intrinsic nature comprising multi-scale and multi-physics problems. Typical diesel spray is fed through nozzle orifice on the order of 100 μm or less; then high-speed atomization process drives the characterizing length scale of droplets down to a few micrometers, resulting in fast evaporation. The atomization process also leads to rapid increase of discontinuous (dispersed) interphase surface. Hence, it is challenging to numerically treat such a dynamical change in interphase boundary where phase interactions occur in much smaller length scale, since it often requires dynamically adjustable and refined discretized domain at CFD run-time, yielding computationally cost-consuming issues. Therefore, an alternate cost-effective approach is preferred. Following sections describe affordable modeling techniques for dispersed spray solution described in a Lagrangian coordinate.

2.1.2.1 Discrete Droplet Model (DDM): Single-Droplet Equations

A computationally affordable method can be employed by describing the dispersed spray elements as a cloud of "computational parcels" in Lagrangian manner. This method, so-called "discrete droplet model (DDM)" [71], has become the standard method in numerous engine simulations. In this method, each of parcels therefore represents a group of droplets in identical properties sharing same dynamics and thermodynamic state; therefore, the spray is statistically described by a large number of stochastic computational parcels.

Mathematical formulations of the computational parcels are constructed in a La-

grangian coordinate; hence they differ from the conserved scalar balance equations explained in the previous section. However, since the Eulerian description and the Lagrangian description share the same physical coordinate, (x, y, z, t), phase interactions are allowed by coordinate mapping; i.e., parcel-to-cell matching in space. The presence of parcel can therefore affect the gas flow properties defined at the nearest cell through the appropriate source term evaluation; inversely the influence of gas phase on the parcels can be accompanied by directly referring the gas properties represented by the cell volume encompassing the parcels. This method of interphase coupling method is termed *two-way coupling*; i) droplet contribution to gas phase, and ii) gas phase contribution to droplet.

Based on the DDM approach, following descriptions present the *single-particle equations* responsible for gas phase contribution to droplet (one-way coupling); hence, mass, momentum, and energy conservation due to phase interactions.

Continuity Equation

The particle continuity equation essentially states that the rate of change in particle mass $\dot{m}_p$ is balanced with the mass flux through the particle surface boundary due to evaporation for most practical cases:

$$\dot{m}_p = \frac{dm_p}{dt} = -\rho_p \, \omega A_{sp} \tag{2.24}$$

where ω stands for the characteristics velocity of vapor release outward through particle outer surface area A_{sp}; thus $\rho_p \, \omega$ represents average mass flux due to evaporation.

The above equation can be recast for mass change due to evaporation as given below:

$$\frac{dm_p}{dt} = -\pi D_p \mathcal{D} Sh \rho_v ln \frac{p - p_{v,\infty}}{p - p_{v,s}} \tag{2.25}$$

where D_p is the diameter of spherical particle, and $p_{v,s}$ and $p_{v,\infty}$ are partial pressure of vapor at particle surface and far ambient gas. The Sherwood number is estimated by $Sh = 2.0 + 0.6Re^{1/2}Sc^{1/3}$ by the Ranz and Marshall's drop evaporation model [131], where Sc is the laminar flow Schmidt number estimated at the mean temperature $T_m = 1/2(T_p + T_g)$.

Momentum Equation

The trajectory $x_{p,i}$ of parcels is dynamically tracked in three-dimensional space (x, y, z) and time by the particle equations of motion in tensor notation:

$$\frac{dx_{p,i}}{dt} = u_{p,i} \tag{2.26}$$

$$\rho_l V_p \frac{du_{p,i}}{dt} = F_{p,i} \tag{2.27}$$

$$F_{p,i} = F_{drag,i} + F_{g,i} = C_D A_p |\widetilde{u}_i - u_{p,i}|(\widetilde{u}_i - u_{p,i}) + \rho_l V_p g_i \tag{2.28}$$

where the droplet drag coefficient C_D is determined by

$$C_D = \begin{cases} 0.424 & Re > 1,000 \\ \frac{24}{Re}\left(1 + \frac{1}{6}Re^{2/3}\right) & Re \leq 1,000 \end{cases} \tag{2.29}$$

In Equation 2.27 known as droplet momentum conservation equation, liquid density is denoted by ρ_l, V_p is the volume of parcel, and $F_{p,i}$ indicates external forces acting on the parcel volume. In Equation 2.28, A_p is the cross-sectional area normal to the relative velocity vector $(\widetilde{u}_i - u_{p,i})$. The droplet Reynolds number (Re) in Equation 2.29 is based on droplet diameter and the relative velocity. In many practical cases, the external forces are only considered for drag force, $F_{drag,i}$, and gravitational force, $F_{g,i}$. It is also worth noting that the gravitational force is several order of magnitude

smaller than the drag force; hence it is often neglected.

Energy Equation

The rate of change in energy contained in droplet volume is determined by the total rate of the external kinetic energy and the internal energy. The internal energy mainly changes by the heat transfer through the interphase surface. The kinetic energy is produced and/or consumed by the flow work due to the surface boundary change, which is typically very small order of magnitude compared to heat transfer energy. The surface energy associated with the surface tension is also often neglected; instead, it is considered in the spray atomization modeling as will be discussed later. Thus, the form of droplet energy change considered in this study may reduce to following equation:

$$m_p c_p \frac{dT_p}{dt} = \dot{Q}_p + \dot{m}_p h_L \tag{2.30}$$

where c_p is the specific heat of the droplet material, and h_L is the latent heat. The rate of heat transfer $\dot{Q}_p$ between droplet and ambient gas can be estimated from followings:

$$\dot{Q}_p = \pi D_p \, k_g Nu f (T_g - T_p) \tag{2.31}$$

$$f = \frac{z}{z-1} \quad , \quad z = -\frac{c_{p,v} \, \dot{m}_p}{\pi D_p k_g Nu} \tag{2.32}$$

Here, k_g is the thermal conductivity of the adjacent gas mixture, and f is a correction factor that accounts for the impact of mass transfer on the heat exchange rate [132]. $c_{p,v}$ is the fuel vapor specific heat. The Nusselt number Nu is usually calculated by the Ranz-Marshall's correlation [131]:

2.1.2.2 Closures for Spray Source Terms

To complete the two-way coupling between two phases, the source terms; e.g., $\dot{\rho}_s$, $F_{s,i}$, H_s, in Equations 2.1 through 2.4 accounting for droplet contribution to gas phase need to be evaluated. For given arbitrary source term $\dot{S}$ in the balance equations, the time rate of contribution $\dot{s}$ by N_p parcels (N_d droplets in each) encompassed by the control volume (cell volume; CV) over the infinitesimal time ($\Delta t \to 0$) can be expressed by:

$$\dot{S} = \lim_{\Delta t, \delta V \to 0} \frac{1}{\Delta t \, \delta V} \int_{CV} \left(\sum_{p=1}^{N_p} \int_{t}^{t+\Delta t} N_d \dot{s}_d d\tau_s \right) dV \tag{2.33}$$

Provided that the finite volume method (FVM) is used, the source terms in the PDEs are converted to the volume integral form over the cell volume. Thus, in Equation 2.33, Δt and dV are equivalent to CFL (Courant–Friedrichs–Lewy [133]) time step and cell volume. The individual droplet contribution $\dot{s}_d$ may be substituted by any of previously defined contributions; e.g., evaporation rate in Equation 2.25, drag force in Equation 2.28, and heat transfer in Equation 2.31. Lastly, the sub-scale time level τ_s characterizes the relaxation time of the corresponding quantity transfer as listed below [134], and those time scales can be incorporated for the sub-time integrations within every CFL time step.

Mass transfer (evaporation) relaxation time:

$$\tau_{evap} = \frac{\rho_l D_p^2}{6 \mathcal{D} Sh \rho_v ln \frac{p - p_{v,\infty}}{p - p_{v,s}}} \tag{2.34}$$

Momentum (droplet drag) transfer relaxation time:

$$\tau_{mom} = \frac{3 \rho_l D_p}{4 \rho_g C_D |\widetilde{u}_i - u_{p,i}|} \tag{2.35}$$

Energy (heat) transfer relaxation time:

$$\tau_{heat} = \frac{\rho_l D_p^2 c_p}{6 k_g Nu} \tag{2.36}$$

2.1.2.3 Spray Atomization Models

Previously, the surface energy engaged in energy conservation was suggested to be neglected; instead, discussion of such a type of energy was reserved for the spray atomization modeling. The atomization refers to the disintegration of liquid bulk mass forming a larger number of smaller droplets by means of external force and/or internal force. Since the breakup process results in rapid increase of interphase surface area, one can postulate that the surface energy subject to surface tension (σ_l) must be highly involved as an opposing force. As such, when the external and/or internal forces are not balanced with the opposing force, the liquid surface disruption and subsequent breakup process will initiate.

As aforementioned, the driving forces governing the breakup process may be due to external force and internal force. The external force is rather obvious; the aerodynamic force may disturb the liquid surface promoting atomization process, while the internal force may likely involve internal turbulent flow kinetic energy or thermodynamic state change. It is also possible that multiple forces may arise simultaneously and augment the breakup process at higher rate. In the previous literatures, many of spray breakup sub-models have been developed in regard to detailed breakup mechanisms; so that they can take adequate driving forces into account for diesel engine relevant conditions.

KH model: aerodynamically induced breakup model

Adopted as the external force driven mechanism, aerodynamically induced primary breakup is considered in this study by employing the Kelvin-Helmholtz (KH) wave

instability model [74]. Further detailed descriptions of the model are not repeated in this section. Readers are encouraged to see Section 1.2.5.1.

KH-Faeth model: a new hybrid primary breakup model

Earlier descriptions of the nozzle generated turbulent flow impact on the primary breakup (namely *turbulence breakup* hereafter) in the Lagrangian modeling framework were first attempted by Huh-Gosman model [90]. Then, Som and Aggarwal [89] extended the Huh-Gosman model by putting together with the KH model and their new formulations of cavitation induced breakup model, suggesting KH-ACT model as a hybrid primary breakup model accounting for three competing breakup mechanisms. In these models, the size of child droplets generated from the primary breakup is assumed to be scaled within integral length scale range of the internal flow turbulence energy spectrum, which was recently questioned by Magnotti's study [91].

To tackle the child droplet scaling problem, Magnotti [91] put forth a new hybrid breakup model named KH-Faeth model on the basis of the KH-ACT model platform (see Equations 1.4a - 1.4b) without inclusion of the cavitation breakup regime. Based upon the extensive studies of Wu and Faeth [29–31], the scaling of inertial sub-range of the turbulent flow was found to be relevant for the child droplet sizing. Hence, newly defined characteristic length L_{Faeth} and time τ_{Faeth} were incorporated in her new KH-Faeth model in combination with the KH model breakup rate:

$$\frac{L_A}{\tau_A} = \max\left\{\frac{L_{KH}}{\tau_{KH}}, \frac{L_{Faeth}}{\tau_{Faeth}}\right\} \tag{2.37}$$

where,

$$L_{Faeth} = C_{sx}\Lambda\left(\frac{x}{\Lambda We_{f\Lambda}^{1/2}}\right)^{2/3} \tag{2.38}$$

$$\tau_{Faeth} = C_\tau \sqrt{\rho_f \frac{L_{Faeth}^3}{\sigma}} \tag{2.39}$$

The scales defined above were characterized at the onset of turbulent breakup; hence the time required to form a droplet, τ_{Faeth}, was assumed to be proportional to the time required for a droplet to form from a ligament of size L_{Faeth} due to the Rayleigh instability mechanism. According to the theoretical basis developed by Wu and Faeth [29], the Equation 2.38 correlates L_{Faeth} with the axial location, x, where droplets are formed from the turbulent breakup process. The Weber number $We_{f\Lambda}$ is the Λ-based liquid weber number where Λ denotes the radial integral length scale and is usually set to the nozzle diameter. The empirical constants C_{sx} and C_τ were suggested to be set to 0.65 and 1.0, respectively in Magnotti's first study of the KH-Faeth model.

Magnotti [91] investigated prediction accuracy and parametric sensitive with the KH-Faeth model against KH model and KH-ACT model However, the model has not been fully examined over a range of conditions where the turbulence breakup may stand out; that is, the KH-Faeth model has not been moderately validated yet.

Secondary breakup model: Rayleigh-Taylor (RT) instability breakup

Once the primary breakup occurs, a cloud of child droplets is generated along the liquid core trajectory; then the droplets continue to undergo subsequent event of droplet mass disintegration (secondary breakup) and/or droplet-droplet interaction (e.g., collision). In this study, the droplet collision is assumed to be less influential than the breakup process.

Such a consecutive breakup process is usually modeled using the widely adopted hybrid model which considers the primary breakup (KH wave instability) and another aerodynamically augmented breakup for child droplets by Rayleigh-Taylor (RT) wave instability theory [76]. The secondary breakup is thus described by the RT model;

then the formation of secondary droplets through the RT wave disruption is governed by the following length and time scales:

$$r_{RT} = \pi \frac{C_{RT}}{k_{RT}} \tag{2.40}$$

$$\tau_{RT} = \frac{1}{\Omega_{RT}} \tag{2.41}$$

where r_{RT} is the stable secondary droplet size by the RT breakup, and τ_{RT} is the breakup time scale which represents time required to form the secondary droplet once the RT wave initiates. Ω_{RT} is the wave growth rate with the wave number k_{RT}, and C_{RT} is the model constant that users may empirically calibrate.

2.2 Turbulent Combustion Modeling

The highly non-linear and multi-scale nature of diesel engine combustion gives very limited allowance to deterministic analysis; thus, modeling techniques are necessary in many practical combustion research activities. Of many modeling strategies, difficulty in turbulent combustion modeling has particularly been emphasized because turbulent-chemistry interaction (TCI) and finite rate chemistry are very likely to dominate unsteady flame stabilization, autoignition as well as pollutant formation process. In this regard, various TCI modeling strategies have already been reviewed in Section 1.2.5.2. To help gain in-depth knowledge basis about widely accepted approaches detailed chemistry assisted TCI modeling and ultimately guide the model improvement, this study is dedicated to further examine two approaches to modeling TCI; thus, the following sections describe the basic principles of (i) kinetics-controlled combustion model and (ii) turbulent mixing-controlled combustion model.

2.2.1 Well-Stirred Reactor (WSR) Model: Kinetics-Controlled Combustion Model

Adopted as a reaction rate approach coupled with finite rate chemistry (detailed chemistry), the well-stirred reactor (WSR) model has been popularly implemented in most today's CFD codes for diesel engine simulations. Therefore, the WSR model is generally incorporated within CFD integration loop in order to directly evaluate turbulent mean reaction rate terms $\overline{\dot{\omega}}_k$ in species transport equations in Equation 2.3. As the name explicitly implies, the underlying assumption of this model is to apply homogeneous mixture (often called perfectly-stirred reactor, well-mixing by other researchers) assumption in control volume before chemical reactions initiate; thus effect of finite rate of turbulent mixing is not taken into account, rather chemically detailed kinetics is considered.

The WSR model utilizes a direct integration method to evaluate the reaction rate source terms without consideration of high order moments of turbulent fluctuating scalars so that the species mass fractions within each computational cell are assumed to be homogeneously distributed (i.e., infinitely fast mixing). The mean reaction rate is then computed directly from the Arrhenius law formulation, $f_k(Y_{i,cell}, T_{cell})$, as a function of reactive scalars defined in the control volume. Such a calculation is conducted considering only first order moment, or mean, of the scalars within cell volume. In practical turbulent combustion applications, however, this approximation may be very inaccurate, with errors of up to several orders of magnitude arising due to the highly non-linear nature of the Arrhenius law formulation. Nevertheless, this type of moment method is often used in many engineering level research. To account for turbulent mixing effects, a segregation factor, α_s, is often introduced to account for modeling the higher order terms, which have been neglected. As such, sub-grid

heterogeneous mixture and temperature variations can be considered.

$$\overline{\dot{\omega}}_k = f_k(\widetilde{Y}_n, \widetilde{T})(1 + \alpha_s) \tag{2.42}$$

In the WSR model, therefore, the segregation value is set to 0.

As a direct integration method for the terms $\overline{\dot{\omega}}_k$, the WSR model is to directly integrate the production rate of k-th species as in the form below:

$$\overline{\dot{\omega}}_k = \frac{\widetilde{Y}_k(t + \Delta t) - \widetilde{Y}_k(t)}{\Delta t} \tag{2.43}$$

where,

$$\widetilde{Y}_k(t + \Delta t) = \widetilde{Y}_k(t) + \int_t^{t+\Delta t} \left[f_k \left(\widetilde{Y}_k(t), \widetilde{T}(t) \right) \frac{W_k}{\overline{\rho}} \right] dt^* \tag{2.44}$$

In Equation 2.44, Δt stands for CFL time step, and dt^* denotes sub-integration time step based on characteristics time scale of corresponding reaction rate. To this end, an ordinary differential equation (ODE) solver takes a part in integrating the chemical reaction problem, providing the closure of reaction rate source terms. As such, this direct integration method is known to be computationally time-consuming problem.

2.2.2 Unsteady Flamelet Model: Turbulent Mixing-Controlled Combustion Model

In a general effort to achieve computationally efficient TCI modeling, the primitive variable method is often preferred because the turbulent mean scalar variables can be resolved from reduced-order manifold of TCI solution libraries rather than integrating numerically stiff ODE problems. To this end, the flamelet model approach was initially proposed suggesting to generate post-processing purposed solution libraries, i.e., laminar flamelet concept [107].

2.2.2.1 Laminar Flamelet Solution

The flamelet modeling approach leverages a separation of the chemistry computation from the CFD solution, such that it significantly reduces the computational cost associated with the resolution of small time and length scales in combustion. In addition, the species transport equations need not be solved in such a flamelet approach. The basic principle of the flamelet model approach is to view a turbulent diffusion flame as an ensemble of locally undisturbed laminar diffusion flamelets. This assumption may apply when the reaction proceeds relatively faster than mixing within asymptotically thin layer, which is referred to as laminar flamelet. Under this hypothesis, it can be stated that the combustion takes place in this thin layer in the vicinity of an iso-surface of stoichiometric mixture (z_{st}) with the locally high gradient of mixture fraction across this layer. In order to generate a reduced-order manifold (mixture fraction z-space) of flamelet structure, important implication of the flamelet structure in z-space can be summarized as:

- Chemical reaction occurs in a thin layer across a surface defined at $z = z_{st}$.
- The structure of flame can be transformed in one-dimensional reaction space z coordinate from the species and energy balance equations defined in a three-dimensional physical coordinate system: i.e., *coordinate transformation* [135].
- Thus, the flamelet structure is locally one-dimensional normal to the flame front.

The coordinate transformation may begin with combining *instantaneous* mass balance (Equation 2.45) and species balance equations (Equation 2.46) and consequently giving Equation 2.47 as written below; to this end, the variables denoted below are not described in Favre-averaged mean quantity.

$$\frac{\partial \rho}{\partial t} + \frac{\partial \rho u_j}{\partial x_j} = 0 \tag{2.45}$$

$$\frac{\partial \rho Y_k}{\partial t} + \frac{\partial \rho u_j Y_k}{\partial x_j} = \frac{\partial}{\partial x_j}\left(\rho D_k \frac{\partial Y_k}{\partial x_j}\right) + \dot{\omega}_k \tag{2.46}$$

$$\begin{aligned} \rho\frac{\partial Y_k}{\partial t} + Y_k\left[\frac{\partial \rho}{\partial t} + \frac{\partial \rho u_j}{\partial x_j}\right] + \frac{\partial Y_k}{\partial z}\left[\rho\frac{\partial z}{\partial t} + \rho u_j \frac{\partial z}{\partial x_j} - \frac{\partial}{\partial x_j}\left(\rho D \frac{\partial z}{\partial x_j}\right)\right] \\ - \rho D\left(\frac{\partial z}{\partial x_i}\frac{\partial z}{\partial x_i}\right)\frac{\partial^2 Y_k}{\partial z^2} = \dot{\omega}_k \end{aligned} \tag{2.47}$$

where the two terms in brackets on the left hand side vanish due to continuity and passive scalar equation (Equation 2.20). Assuming same diffusivities for all species $\mathcal{D}_k = \mathcal{D}$, the coordinate transformation of reactive scalar equations yield:

$$\begin{aligned} \rho\frac{\partial Y_k}{\partial t} &= \dot{\omega}_k + \rho D\left(\frac{\partial z}{\partial x_i}\frac{\partial z}{\partial x_i}\right)\frac{\partial^2 Y_k}{\partial z^2} \\ &= \dot{\omega}_k + \frac{1}{2}\rho\chi\frac{\partial^2 Y_k}{\partial z^2} \end{aligned} \tag{2.48}$$

Similarly, the temperature solution in the flamelet structure can also be formulated beginning with instantaneous energy balance equation, which is not repeated here. Following hypotheses are considered in the derivation of temperature equation:

- Second derivative with respective z is considered predominant from an order of magnitude analysis.
- Spatial pressure gradient and dissipation terms are negligible in low speed (low Mach) flow, but time change in pressure may be considerable.
- Temporal change of pressure may be neglected for diesel spray flame applications.
- Constant heat capacities $c_{p,k} = c_p$ for all species are assumed.

The final form of transformed temperature equation can be expressed as shown below. For further details of coordinate transform and mathematical manipulations,

readers are encouraged to read the previous literatures [42, 93, 135].

$$\rho c_p \frac{\partial T}{\partial t} = \dot{\omega}_T + \frac{1}{2}\rho c_p \chi \frac{\partial^2 T}{\partial z^2} \tag{2.49}$$

Here, the scalar dissipation rate, χ, appears in both Equations 2.48 and 2.49, and can be evaluated as the square of mixture fraction gradient in Equation 2.50.

$$\chi = 2\mathcal{D}\left(\frac{\partial z}{\partial x_i}\frac{\partial z}{\partial x_i}\right) \tag{2.50}$$

The χ plays an essential role in coupling the turbulent mixing field defined in physical space (x_i) and local laminar flamelet solution in z-space. In a counter-flow diffusion flame configuration, for example, the scalar dissipation rate is indicative of flamelet strain rate. In such a flame configuration, a strain rate beyond the critical value results in local flamelet quenching due to excessive thermal diffusion out of the reaction zone. Such a burning diffusion flame lies in the upper branch of the S-shaped curve as depicted in Figure 1.6b. The lower branch of the curve corresponds to a steady mixing problem prior to autoignition. Therefore, the scalar dissipation rate can be considered as an eigenvalue for unsteady flamelet quenching and auto-ignition.

As stated in Equation 2.50, the scalar dissipation rate is defined in the physical space as a function of local mixture fraction $z(x_i)$; therefore a transport equation for mixture fraction variable needs to be defined in the form of passive scalar equation. Particularly for the diesel spray simulations, a source term for the mixture fraction accounting for droplet evaporation is required; hence, Equation 2.21 with inclusion of the source term is reformulated as:

$$\frac{\partial \overline{\rho}\widetilde{z}}{\partial t} + \frac{\partial \overline{\rho}\widetilde{u}_j\widetilde{z}}{\partial x_j} = \frac{\partial}{\partial x_j}\left(\overline{\rho\mathcal{D}\frac{\partial z}{\partial x_j}}\right) + \frac{\partial}{\partial x_j}\left(\overline{\rho}\mathcal{D}_t\frac{\partial \widetilde{z}}{\partial x_j}\right) + \dot{S}_{evap} \tag{2.51}$$

where the source term $\dot{S}_{evap}$ is evaluated utilizing Equations 2.25 and 2.33.

In addition, the influence of turbulent scalar fluctuating quantities (z'') may gen-

erate variance of the quantity in statistical point of view; such a variance of scalar is also indicative of local turbulent intermittency and mixing intensity. To address such an impact, additional transport equation is required to define the local variance of mixing field scalar; namely, mixture variance transport equation as expressed below:

$$\frac{\partial \overline{\rho}\widetilde{z''^2}}{\partial t} + \frac{\partial \overline{\rho}\widetilde{u}_j\widetilde{z''^2}}{\partial x_j} = -\frac{\partial}{\partial x_j}\left(\overline{\rho}\widetilde{u''_j z''^2}\right) + 2\overline{\rho}\left(-\widetilde{u''_j z''}\right)\frac{\partial \widetilde{z}}{\partial x_j} - \overline{\rho}\widetilde{\chi} \tag{2.52}$$

where there are three unclosed terms on the right-hand side. The first two terms are representative of *turbulent transport* of mixture fraction variance and *production of scalar fluctuation*, respectively; they are modeled by:

$$\widetilde{u''_j z''^2} = -D_t \frac{\partial \widetilde{z''^2}}{\partial x_j} \tag{2.53}$$

$$\widetilde{u''_j z''} = -D_t \frac{\partial \widetilde{z}}{\partial x_j} \tag{2.54}$$

Lastly, the third term measures the scalar dissipation due to molecular diffusion; i.e., decay of mixture fraction fluctuations, and thus the Favre averaged scalar dissipation rate is formulated by:

$$\widetilde{\chi} = 2D\widetilde{\left(\frac{\partial z''}{\partial x_j}\right)^2} \tag{2.55}$$

However, since scalar dissipation happens in very small scale compared to typical computational grid scale, the square of mixture fraction gradient is difficult to be captured. Therefore, this unclosed term has to be modeled typically by scale analysis shown below or some dynamic model.

$$\widetilde{\chi} = c_\chi \frac{\widetilde{\epsilon}}{\widetilde{k}}\widetilde{z''^2} \tag{2.56}$$

Here, C_χ is a free parameter that is typically set to 2.

$$\widetilde{\chi} = 2D\widetilde{\left(\frac{\partial z''}{\partial x_j}\right)^2} \tag{2.57}$$

2.2.2.2 Representative Interactive Flamelet (RIF) model

The representative interactive flamelets (RIF) model [96, 111] is an extended version of the flamelet model that executes the flamelet solver (i.e., RIF solver) dynamically and allows the flamelet solution to be interacted with the CFD mixture field solutions. The RIF model utilizes a dynamically computed flamelet library and turbulent mean scalars (e.g., $\widetilde{Y}_k$ and $\widetilde{T}$) are calculated by weighting the laminar flamelet solutions with a relevant choice of statistics, described by a presumed probability density function (PDF). The basic principle of the RIF model is identical with this approach except that it incorporates the unsteady history of flamelets that would otherwise be unable to follow the rapid change of mixing field, especially in the high-pressure diesel spray problem [109]. In order to capture the unsteady nature of injection and following ignition processes, the flamelet code solves the flamelet equations in parallel with the CFD code, such that the flamelet parameter (i.e., conditioned scalar dissipation rate) is tracked from the CFD solution.

Determination of mean species mass fraction

In this modeling approach, the essential feature of turbulence-chemistry interaction is obtained by the statistical description of the laminar flamelet solution with respect to a random variable of the mixture fraction, z. Thus, a mean value of the turbulent reactive scalar, $\widetilde{Y}_k$, in physical space, can be determined by the first order moment of the instantaneous scalar, Y_k, which is derived in reaction space using a presumed PDF, as expressed in Equation 2.58. This study solely employs the beta PDF formulation

as written in Equation 2.59.

$$\widetilde{Y}_k(x_i,t) = \int_0^1 Y_k(z,t) pdf(z,\widetilde{z},\widetilde{z''^2};x_i,t)dz \tag{2.58}$$

$$pdf(z,\widetilde{z},\widetilde{z''^2};x_i,t) = \frac{z^{\alpha-1}(1-z)^{\beta-1}}{\Gamma(\alpha)\Gamma(\beta)}\Gamma(\alpha+\beta) \tag{2.59}$$

where Γ is a gamma function and two parameters α and β are associated with the mean mixture fraction and mixture fraction variance as:

$$\alpha = \widetilde{z}\gamma \ , \quad \beta = (1-\widetilde{z})\gamma \ , \text{ and } \quad \gamma = \widetilde{z}(1-\widetilde{z})/\widetilde{z''^2} - 1 \tag{2.60}$$

As expressed in the PDF formulation, the local statistics is determined by the mean mixture fraction, $\widetilde{z}$, and its variance $\widetilde{z''^2}$, which are solved in Equations 2.51 and 2.52. In other words, once these variables are determined at given time and spatial coordinate by the CFD solution, the statistics of the local flamelets can be determined, consequently providing mean species concentrations, $\widetilde{Y}_k$.

Determination of mean temperature: CONVERGE vs. GTFOAM

Indeed, the originally proposed flamelet model by Peters [42] is to provide the entire reactive scalar solutions; i.e., species mass fractions and temperature resolved from the flamelet species equation 2.48 and the flamelet temperature equation 2.49. However, in the RIF model incorporated in the CONVERGE code, the temperature equation in reaction space is not solved. Instead, the turbulent mean temperature, $\widetilde{T}$, in physical space is evaluated once all turbulent mean species concentrations, $\widetilde{Y}_k$, are determined by PDF integration of Equation 2.58; thus, from the definition of the total enthalpy, the mean temperature field $\widetilde{T}$ is obtained by Equation 2.61. The total enthalpy $\widetilde{H}$ is

provided by the CONVERGE CFD solver.

$$\widetilde{H} = \sum_{k=1}^{N_{\text{spc}}} \widetilde{Y}_k h_k(\widetilde{T}) \tag{2.61}$$

On the other hand, the GTFOAM library for OpenFOAM simulations follows different approach from the CONVEGE code. In the CFD application packages for flamelet modeling provided by GTFOAM, the run-time RIF solver executes species equations 2.48 and temperature equation 2.49 with respective to sensible enthalpy conservation, providing reaction space solutions for $Y_k(z)$ and $h_s(z)$. In turn, sensible enthalpy in physical space, $\widetilde{h}_s(x_i, t)$, is calculated by the PDF integration method directly as expressed below:

$$\widetilde{h}_s(x_i, t) = \int_0^1 h_s(z, t) pdf(z, \widetilde{z}, \widetilde{z''^2}; x_i, t) dz \tag{2.62}$$

Therefore, the RIF-CFD solution mapping technique in the GTFOAM is more biased towards the post-processing method of the classical flamelet model strategy. A possible deviation from such a difference in the model implementation in two codes will be discussed in the results section.

Flamelet parameter: domain-averaged scalar dissipation rate

It should be noted that the mean scalar dissipation rate, $\widetilde{\chi}$, from Equation 2.56 does not substitute the place of χ in Equations 2.48 and 2.49, because $\widetilde{\chi}$ is a locally resolved mean quantity by the CFD solver, whereas the parameter χ in the flamelet equations is uniquely defined in the reaction space. With a fast chemistry assumption [42], the quantity χ is generally evaluated conditionally over the stoichiometric condition, and is thus replaced with $\langle \chi_{st} \rangle$. Since the turbulent mixing intensity is conveyed through the scalar dissipation rate in the flamelet equation, it requires a relevant modeling approach. Pitsch et al. [110] assumed the local flamelet structure can be

described by counterflow diffusion flames and proposed analytic expressions for the scalar dissipation rate as a function mixture fraction:

$$\chi(z) = \langle \chi_{st} \rangle \frac{f(z)}{f(z_{st})} \tag{2.63}$$

where $f(z) = \exp[-2(erfc^{-1}(2z))]$ with an error function, $erfc$. The domain-averaged scalar dissipation rate conditioned over the stoichiometric condition is then calculated:

$$\langle \widehat{\chi_{st}} \rangle = \frac{\int_V \overline{\rho}_g \langle \chi_{st} \rangle^{3/2} pdf(z_{st}) dV}{\int_V \overline{\rho}_g \langle \chi_{st} \rangle^{1/2} pdf(z_{st}) dV} \tag{2.64}$$

And the scalar dissipation rate conditioned over the stoichiometric mixture only at given location is expressed by:

$$\langle \chi_{st} \rangle = \frac{\widetilde{\chi} f(z_{st})}{\int_0^1 f(z) pdf(z) dz} \tag{2.65}$$

2.2.2.3 Eulerian Particle Flamelet Model (EPFM)

The RIF model has been known to exhibit shortcomings for highly unsteady turbulent diffusion flames. Indeed, the use of a single flamelet library with a single domain averaged scalar dissipation rate may not properly reflect the unsteady nature and spatial variations of flamelet parameters. Barths and co-workers [114,136] suggested a new flamelet model utilizing multiple flamelets to account for different histories of the scalar dissipation rate for different mixture elements. In this model, a mass-weighted fraction of Eulerian particles is tracked as a marker solution of injected mixtures that correspond to each flamelet history. The marker trajectory is achieved by constructing a passive scalar transport equation identically with Equation 2.51. The fraction of markers over the total mixtures denoted as $\widetilde{z}_l$, for l-th flamelet takes the place of $\widetilde{z}$ in

Equation 2.51 and simultaneously should satisfy the following condition:

$$\widetilde{z} = \sum_{l=1}^{N_f} \widetilde{z}_l \tag{2.66}$$

where N_f means the total number of flamelets employed. Each flamelet is sequentially initiated during the injection event and covers only a certain range of domain and time history. This way of specifying the partial domain allows for spatially varying scalar dissipation to be taken into account. The modified domain-averaged scalar dissipation rate is therefore rewritten as:

$$\langle \widehat{\chi_{st}} \rangle = \frac{\int_V \left(\widetilde{z}_l / \widetilde{z}\right) \overline{\rho}_g \left\langle \chi_{st} \right\rangle^{3/2} pdf(z_{st}) dV}{\int_V \left(\widetilde{z}_l / \widetilde{z}\right) \overline{\rho}_g \left\langle \chi_{st} \right\rangle^{1/2} pdf(z_{st}) dV} \tag{2.67}$$

CHAPTER 3

ASSESSMENT OF NOZZLE GENERATED TURBULENCE PRIMARY BREAKUP MODEL

Although the classic Kelvin-Helmholtz model accounting for aerodynamically driven primary breakup has been widely incorporated in many engine CFD codes for the last three decades, use of this model has been limitedly meaningful at conventional engine operating conditions, which is dominated by high-temperature combustion dynamics. Thus the influence of atomization may not be substantial in mixture formation process; i.e., diffusion-dominated mixing discussed in Section 1.2.1.1. This lack of predictive capability may point to the likelihood of an incorrect physical basis for the model formulation. As such, there have been more recent spray-model development efforts that incorporate additional sources of jet instability and breakup, including nozzle-generated turbulence and cavitation (e.g., KH-ACT model [89] and Huh-Gosman model [90]), but predictive capabilities still remain questionable.

As aforementioned in the previous section 2.1.2.3, the KH-Faeth model was conceptually proposed by Magnotti [91] under the notion that the primary breakup is mainly governed by nozzle-generated turbulence particularly under low ambient density conditions. In this new modeling approach, termed KH-Faeth model, two different primary breakup models are combined to allow for the hybrid breakup modeling approach, i.e., Kelvin-Helmholtz instability breakup mechanism and turbulence-induced breakup are competed via dominant breakup rate evaluation. Despite the strong basis of experimental observation by Wu and Faeth [29], the model was rather limitedly examined; meaning the model has not been fully assessed in terms of prediction capability and applicability over various range of engine relevant conditions.

3.1 Test Methods

For model assessment purpose, detailed atomization measurements across a wide span of engine-relevant conditions are needed to both confirm appropriate physical formulation of models and to accurately validate the model predictions. Particularly, as diesel engines increasingly operate under low-temperature combustion (LTC) conditions, where ambient densities and aerodynamic forces are much lower than under conventional diesel conditions, further consideration of extended measurement range is needed.

The open-source CFD tool package, namely OpenFOAM, used for the present spray modeling study is integrated with a user-defined library developed at Politecnico di Milano, called Lib-ICE, which includes a set of solvers and Lagrangian modeling libraries [127]. The proposed KH-Faeth breakup model is implemented into the Lib-ICE library to enable the model to run test simulations. Then, the results are validated against detailed droplet sizing measurement techniques stemming from recent collaborative experiments between co-workers at Georgia Tech and Argonne National Laboratory.

3.1.1 Engine Combustion Network (ECN) Injectors and Test Conditions

To help gain in-depth insights into the nozzle-generated turbulent flow effect on atomization process, it is desired to suppress the contribution of cavitating bubble formation throughout the flow trajectory inside the injector nozzle. To this end, careful selection of working fluid and injector is needed.

Cavitation can be suppressed by preventing the liquid fuel pressure from dropping down below the fuel vapor pressure along the flow trajectory [137, 138]. One way to achieve this effect is to adopt an injector nozzle having a converging geometry in the sac volume with a rounded corner shape and minimal surface imperfec-

Table 3.1: *ECN injector test setups for vaporizing and non-vaporizing inert spray injections; n-dodecane is employed as a non-cavitating working fluid.*

ECN injector (serial #)	**Spray A (210675)**	**Spray D (209133)**
Orifice diameter [μm]	89.4	186
Discharge coefficient	0.86	0.9
Nozzle K-factor	1.5	3.7
Ambient gas temperature [K]	303 (non-vaporizing) 900 (vaporizing)	303 (non-vaporizing) 800 (vaporizing)
Ambient gas composition [% by volume]	N_2: 89.71% CO_2: 6.52% H_2O: 3.77 %	N_2: 100%
Ambient gas density [kg/m^3]	22.8	1.2 / 2.4 / 22.8
Nominal ambient gas pressure [bar]	60	1 / 2 / 20
Liquid/gas density ratio [-]	33.7	674 / 337 / 33.7
Injection pressure [bar]	1500	500 / 1000 / 1500

tions [139–141]. Through the Engine Combustion Network (ECN) [92], single-hole research-grade diesel injectors with well-characterized internal nozzle geometries have been standardized, and two different ECN injectors, e.g., Spray A and Spray D injectors, are available for such a non-cavitating nozzle flow. In addition, a selection of well-informed fuel, such as *n*-dodecane [142], can minimize the likelihood of cavitating bubble formation. In this study, therefore, non-cavitating *n*-dodecane fuel injections using the Spray A and Spray D injectors are considered for measurements and simulations.

In order to fully examine the KH-Faeth model, two classes of non-reacting test conditions; (i) vaporizing spray and (ii) non-vaporizing spray, are considered in this study as listed in Table 3.1. Especially in the setup for non-vaporizing conditions, a set of ambient gas density conditions is defined to examine the model predictive ability over a range of different primary breakup regime governing regions such as

aerodynamic breakup and turbulence breakup as discussed in section 1.2.1.2.

3.1.2 Setups for OpenFOAM Simulations

In this test, two different primary breakup models are mainly evaluated in comparison; i.e., the classical aerodynamic primary breakup described by KH model and the new hybrid breakup description of KH-Faeth model. For the ambient gas flow modeling, continuum phase turbulence flow was resolved by Reynolds-Averaged Navier-Stokes (RANS) equation set with coupled standard k-ϵ turbulence model without further calibration for round-liquid jet configuration. Sufficiently large CFD domains (10x10x10 ~ 18 mm^3), allowing to vary in dimension in z-direction for different ambient test conditions to ensure no spray-wall inteference. The computational domain was initialized with 4 mm static hexahedral structured grids. Then, a run-time based dynamic mesh refinement was applied to allow for CFD mesh size reduction to minimum grid size of 0.25 mm to improve prediction accuracy. One million computational parcels were consecutively introduced into computational domain over the injection duration of 2.5 ms. However, actual simulations were performed until it reaches 1 ms of physical elapsed time, which may ensure converged drop sizing statistics. Time averaged drop sizing solutions were obtained through the simulated time frame.

The injector boundary conditions and operating conditions for the modeled sprays are prescribed based on Engine Combustion Network (ECN) Spray A/D experiments [92], with the rate of injection (ROI) profile generated by a virtual injection rate calculator [143].

3.1.3 X-Ray Diagnostics Techniques

X-ray diagnostics can provide a unique capability in quantifying liquid spray mass and surface area distributions especially in optically thick regions of the spray, where a big challenge has been identified when using traditional optical diagnostics. In this

regard, a collaborative experimental campaign has recently been established starting in 2016 in order to combine existing visible-light extinction measurements taken at Georgia Tech and x-ray measurements from the Advanced Photon Source (APS) at Argonne National Laboratory. The x-ray radiography measurements collected are an absorption-based technique, which quantifies the path-integrated liquid mass within a spray plume, commonly referred to as projected mass density (PMD). In this technique, the time-resolved beam intensity incident on the fuel spray, I_0, and beam intensity transmitted through the spray, I, are measured for multiple spray events and ensemble averaged. Then, the PMD of the liquid spray was determined from the absorption measurement using the Lambert-Beer law. Detailed experimental setup for this spray radiography used for the present data validation study are fully described in the literature [144].

Additionally, a recent advanced x-ray beamline technique leverages existing PMD measurements to evaluate droplet statistics utilizing the ultra-small angle x-ray scattering (USAXS) diagnostic [145]. The USAXS measurements were carried out using the beamline of APS facility in order to characterize the total surface area per sample volume of the spray. By combining the surface area measured with USAXS and the PMD measured with radiography, the Sauter mean diameter (SMD) of the droplets in the probed volume can be determined.

Researchers at Georgia Tech performed diffuse back-illumination (DBI) experiments to quantify the optical thickness of the spray. The optical thickness is found by relating the incident and attenuated light intensity via the Beer-Lambert law. This technique was also utilized to quantify the liquid spray penetration rate by tracking the time evolution of the leading edge of the liquid-phase boundary.

The scattering absorption measurement ratio (SAMR), developed by researchers [91, 146] at Georgia Tech was employed to quantify the line-of-sight projection of the spray's ensemble-averaged SMD at the peripheral regions of moderate optical den-

sity. The SAMR technique combines a light scattering measurement of optical thickness (DBI) with an absorption measurement of projected density (x-ray radiography) from the same spray, but from separate experimental facilities at Georgia Tech and Argonne National Lab, respectively. Using Mie theory, the optical thickness can be related to the mean extinction cross-section and liquid volume fraction of droplets within the probed spray volume. The projected density measurement also quantifies the liquid volume fraction of droplets within the same probe volume. The ratio of these two measurements then yields a theoretical relationship to the SMD of the droplet size distribution.

3.2 Validation of KH-Faeth Model Against Measurements

In this study, recent USAXS and SAMR measurements are compared with model-predicted SMD to investigate the importance of primary breakup model formulation and governing breakup mechanisms. Specifically, a new hybrid primary breakup model recently proposed by Magnotti [91] named as the KH-Faeth model, is evaluated especially in terms of relevance of three distinctive breakup regimes proposed by Wu and Faeth [29–31] (i.e., turbulent breakup, aerodynamically-enhanced turbulent breakup, and merged turbulent-aerodynamic secondary breakup). This study ultimately will provide a guidance to further improve the model accuracy as will be discussed in the next section 3.3.

3.2.1 Model Validation in Momentum Exchanging Sprays

Validation of the predicted liquid and vapor penetrations is useful for assessing the accuracy of the modeled momentum transfer between the liquid phase and ambient gas phase. Details of the predicted breakup process also very likely govern the momentum transfer rate because the droplet size statistics will also affect spray inertia. Evaluations of predicted spray penetration at non-vaporizing conditions and vapor-

izing condition have been conducted over various range of ECN injector setups as illustrated in Figures 3.1a and 3.1b for Spray A injector, and Figures 3.1c and 3.1d for Spray D injector.

For Spray A injector setup (upper row of Figure 3.1) where relatively high temperature and high ambient density are characterized (vaporizing condition), overall accuracy from the model considered is acceptable and there is no noticeable deviation between the different model setups. This may suggest two possible reasons. First, the details of primary breakup process may not be heavily influential on the overall spray mass distribution along the trajectory under such a highly evaporating condition. Second, it is also possible that the considered condition is not in favor of promoting turbulent-induced breakup; note that the ambient density is rather high, therefore the aerodynamic shear stress may be more predominant. In this case, the rate of emerging KH breakup regime over KH-Faeth breakup competition may be outstanding; thus, it diminishes the effect of Faeth's turbulence breakup rate in the model.

For another non-vaporizing and vaporizing test cases using Spray D injector (borrom row of Figure 3.1), both the KH model and KH-Faeth model also provide fairly good agreement with the experiments. For potentially same reason, the vaporizing condition test provides close agreement between measurement [148] and the simulation of the two models considered in this study. However, it is noticed that the models display an under-prediction of the liquid penetration rate between $0.2 \sim 0.4$ ms under non-vaporizing conditions at high ambient pressure ($p_{amb} = 20$ bar) in Figure 3.1c. There may be several possible reasons for this discrepancy during the transient period. One possibility is that the primary breakup physics is inaccurately represented in these models. To explore this idea, a simulation was performed with the KH model deactivated in the KH-Faeth model setup, as indicated by a cyan dashed line in Figure 3.1c, forcing the turbulent breakup model to act in isolation.

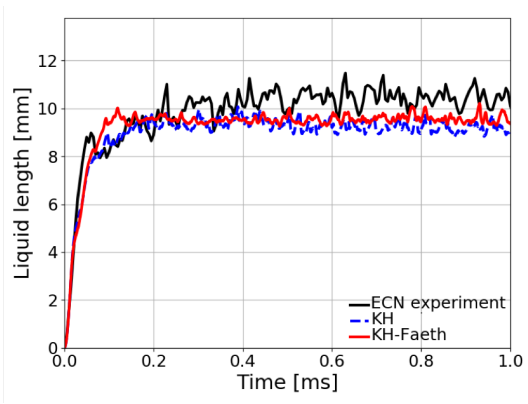

(a) *Liquid penetration at ECN Spray A: vaporizing condition, T_{amb} = 900 K, P_{inj}=1500 bar, P_{amb} = 60 bar (ρ_{amb}=22.8 kg/m^3)*

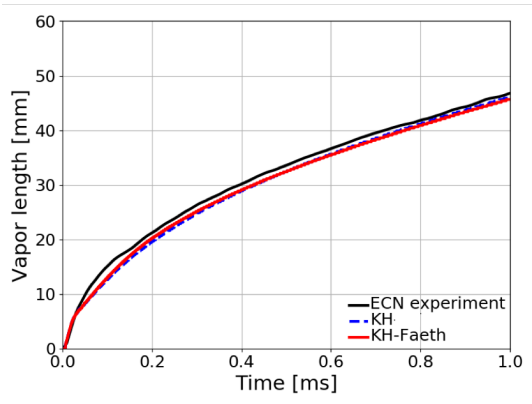

(b) *Vapor penetration at ECN Spray A: same test condition as left*

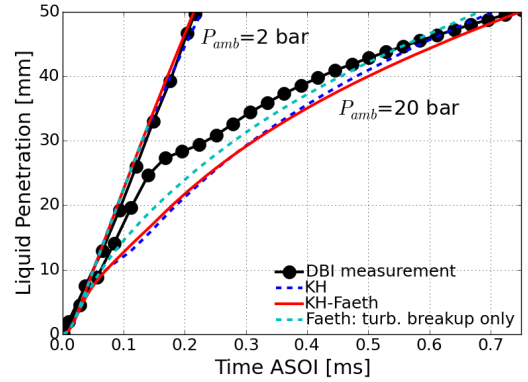

(c) *Liquid penetration at ECN Spray D: non-vaporizing condition, T_{amb} = 303 K, p_{inj}=1500 bar, p_{amb} = 2, 20 bar (ρ_{amb}= 2.4, 22.8 kg/m^3)*

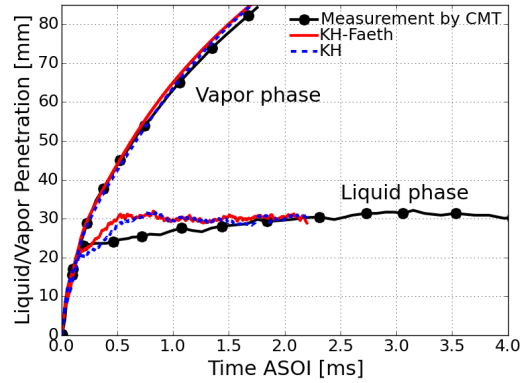

(d) *Vapor penetration at ECN Spray D: vaporizing condition, T_{amb} = 800 K, p_{inj}=1500 bar, p_{amb} = 20 bar (ρ_{amb}= 22.8 kg/m^3)*

Figure 3.1: *Evaluations of liquid and vapor penetrating lengths using ECN Spray A and Spray D injectors under non-vaporizing and vaporizing conditions. The experimental data for the Spray A injector setup was obtained from ECN data library [92], and the DBI measurement for the Spray D injector setup was conducted by researchers at Georgia Tech [147]. The liquid/vapor length data for vaporizing Spray D was obtained from CMT-Motores Térmicos's measurement [148]*

This model prediction is found to be offset somewhat closer to the measured liquid penetration curve, but still lacks the distinct two-phase transient behavior seen in the measurements. The good agreement found under quasi-steady injection conditions at later times suggests that errors are more likely due to inaccuracies in modelling the initial opening transient of the injector and effects on the nozzle flow and spray.

Indeed, the Lagrangian-Eulerian primary atomization modeling approach inherently represents the spray atomization physics at an engineering level, with simplified injection flow boundary conditions that lack the complete details of realistic injection events, which may affect the real spray measurements. In addition, liquid-gas momentum coupling in the near-nozzle regions may be especially prone to large errors since Lagrangian-Eulerian techniques are known to be highly grid dependent. These unsteady flow details are likely to play a significant role in the initial penetration rate of the jet.

3.2.2 Validation of Droplet Sizes and Dispersion

Validation of the models against USAXS measurements of SMD along the spray axis is shown in Figure 3.2 at a wide range of ambient conditions and injection pressures. Although the KH model and KH-Faeth model predict similar spray penetration rates, the predicted axial SMD distributions can strongly differ. In general, the KH-Faeth model is found to be generally predictive across all test conditions, which include a very wide span of ambient density conditions, while the KH model alone aligns well with the measured data at only a few conditions. These results suggest that the proposed hybrid breakup model may improve the predictive capabilities of engine simulations for LTC targeted conditions. Sole use of an aerodynamic breakup (KH) mechanism or model formulation appears to be especially inappropriate at lower ambient density conditions since it is noted that the largest errors are found at P_{amb} = 1 bar. This result is consistent with Wu and Faeth's experimental observations [31] that aerodynamic breakup is irrelevant at high liquid-to-gas density ratios ($\rho_l/\rho_g >$ 500).

On the other hand, the KH-Faeth model underpredicts SMD values at the highest ambient density condition (P_{amb} = 20 bar), as shown in Figure 3.2f. At this condition, the KH model is expected to have more dominant breakup rate superior to the

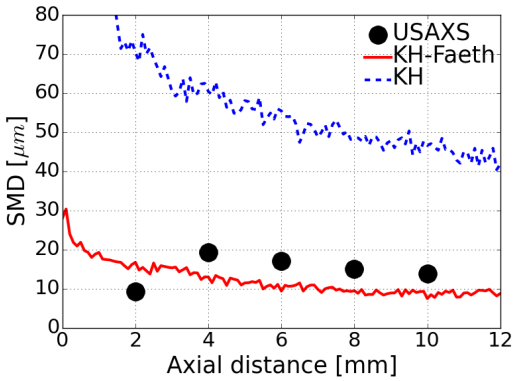

(a) p_{inj}=500 bar, p_{amb}=1 bar

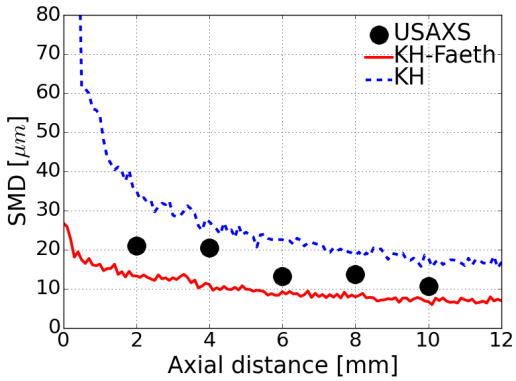

(b) p_{inj}=500 bar, p_{amb}=2 bar

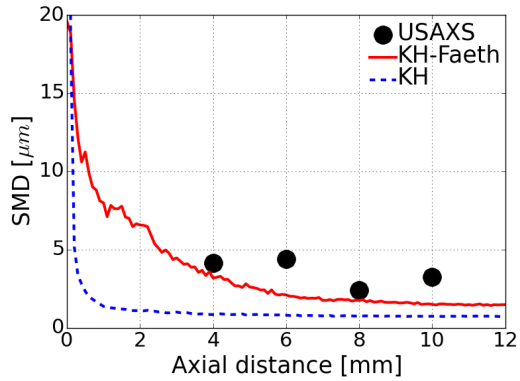

(c) p_{inj}=500 bar, p_{amb}=20 bar

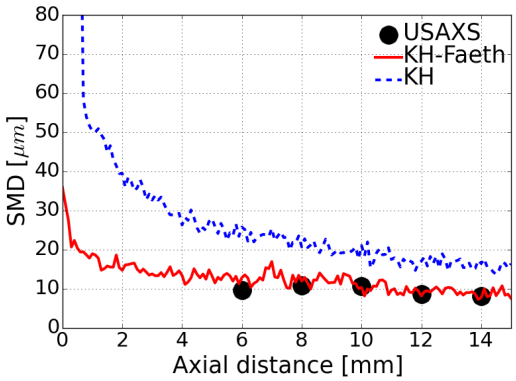

(d) p_{inj}=1500 bar, p_{amb}=1 bar

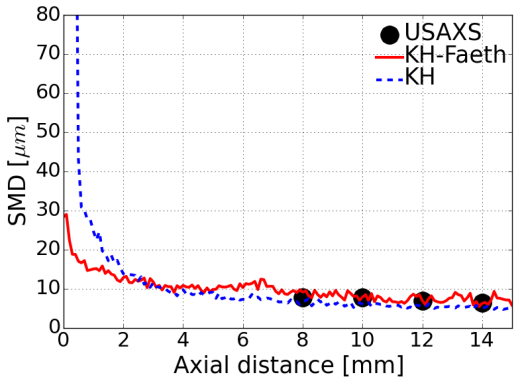

(e) p_{inj}=1500 bar, p_{amb}=2 bar

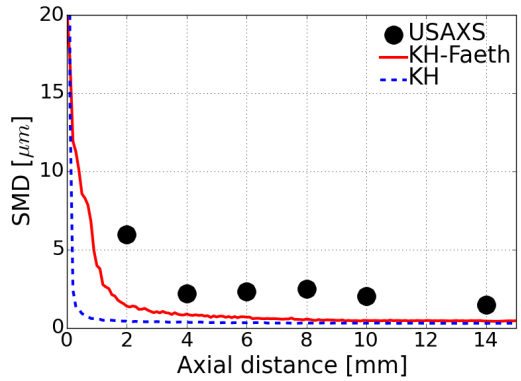

(f) p_{inj}=1500 bar, p_{amb}=20 bar

Figure 3.2: *Comparison between predicted and measured (USAXS) SMD distributions along the spray centerline of ECN Spray D*

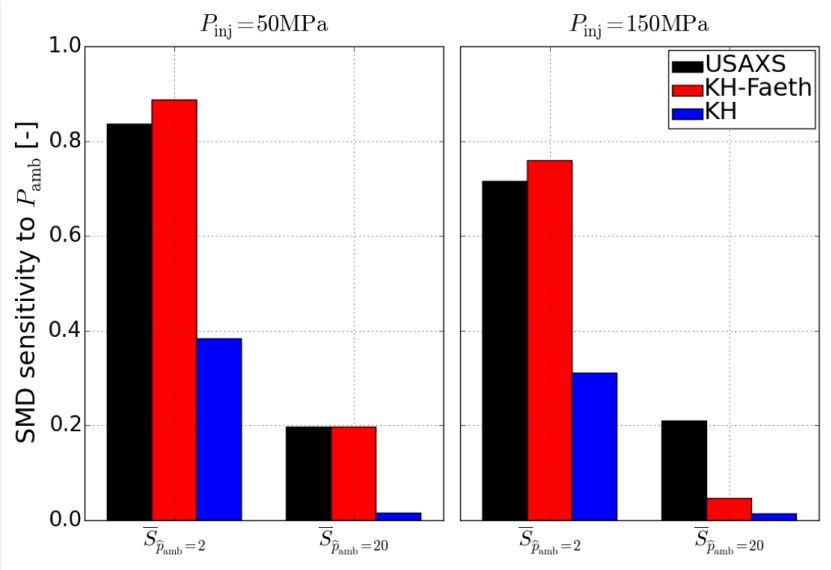

Figure 3.3: *Local SMD sensitivity to change in ambient pressure*

turbulence (Faeth breakup regime) due to the high aerodynamic force at the interphase surface. This can be observed by the nearly overlapping SMD predictions of both the KH and KH-Faeth models downstream of approximately 3 mm at this condition. This finding suggests that even under conditions where an aerodynamic breakup model is expected to be physically appropriate, the KH mechanism or formulation for aerodynamic breakup may be inaccurate.

To further assess the effect of ambient pressure on SMD and the suitability of breakup modeling approaches to capture this effect, a sensitivity analysis is conducted to compare the response of measured and predicted atomization characteristics to changes in ambient conditions. Figure 3.3 shows the relative change in SMD due to change in ambient gas density, indicated on the y-axis as SMD sensitivity to p_{amb}. Here, the sensitivity metric, $\overline{S}_{\widehat{p_{amb}}}$, is defined as the fractional change of the location-specific averaged SMD value due to ambient pressure (or ambient density) change relative to standard atmospheric pressure (p_{amb} = 1 bar). For example, $\overline{S}_{\widehat{p_{amb}}=2} = \overline{\text{SMD}}_{p_{amb}=2\,\text{bar}}/\overline{\text{SMD}}_{p_{amb}=1\,\text{bar}}$ represents a relative change in ambient pressure (or density) of two times. This test metric is calculated from the average axial

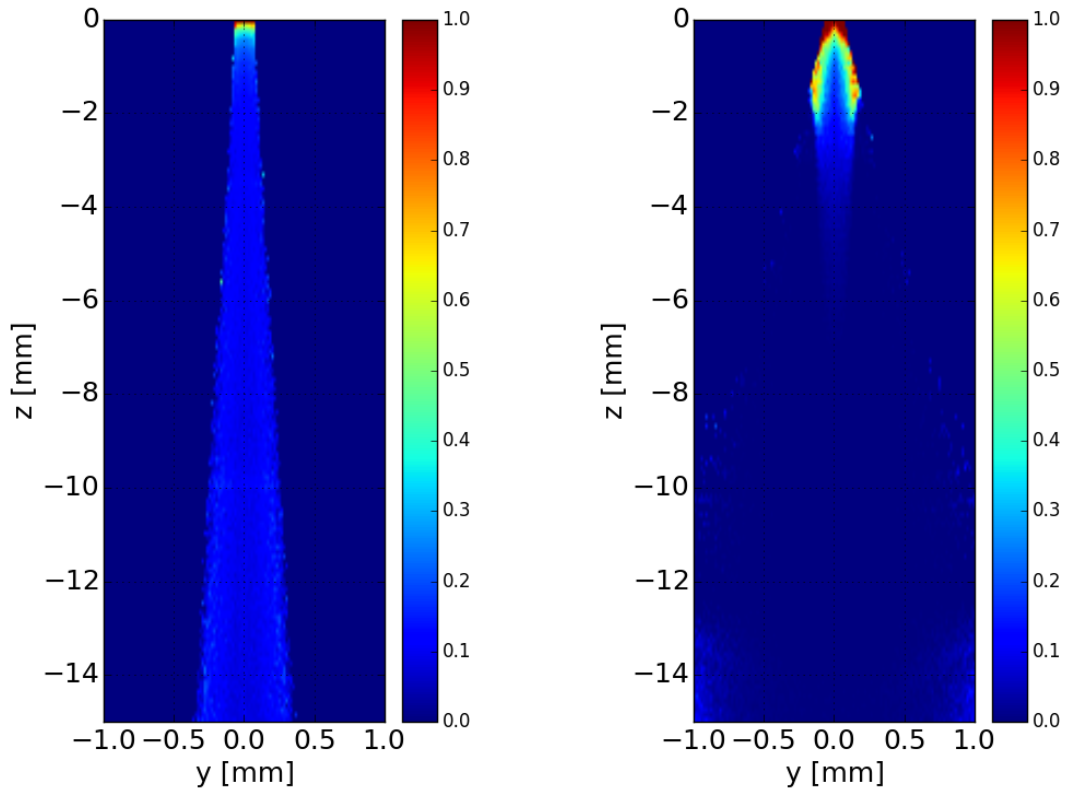

(a) p_{amb} = *1 bar* (b) p_{amb} = *20 bar*

Figure 3.4: *Probability of finding turbulent breakup in KH-Faeth model under low (a) and high (b) ambient densities.* (p_{inj} = *500 bar)*

SMD at downstream locations of $x = 8$ mm and 10 mm.

As seen in Figure 3.3, the relative SMD change predicted by the KH-Faeth model tends to better follow the experimental SMD sensitivity at all conditions. However, a larger change in SMD is predicted at the highest ambient density and injection pressure condition, ($\overline{S}_{\widehat{p_{amb}=20}}$, $p_{inj} = 1500$ bar). At this condition, aerodynamic shear stress on spray surface is highest, and the aerodynamic KH breakup mechanism is expected to control the predicted droplet sizes. Indeed, both the KH and KH-Faeth models predict a similar SMD change at this condition, indicating that the KH model is dominant in the KH-Faeth model. The incorrect magnitude of the predicted SMD change relative to the experiments suggests that the KH model may fail to accurately represent aerodynamic breakup physics in real diesel sprays.

To further illustrate the behaviour of the KH-Faeth model under the effect of ambient density, Figure 3.4 illustrates the likelihood of turbulent breakup over aerodynamic breakup based upon identification of the fastest breakup rate via Equation 2.37. The red contour represents regions of turbulent breakup at the biggest dominance, while dark blue indicates aerodynamic breakup. As shown in Figure 3.4, regions of turbulent breakup are predicted throughout the entire spray plume at $p_{amb} = 1$ bar. whereas it only appears in the near-nozzle region at higher ambient density/pressure ($p_{amb} = 20$ bar) and vanishes rapidly downstream. Thus, even at high ambient density, droplet sizes are initially controlled by the turbulent breakup model, followed by a rapid transition to aerodynamic breakup. As seen previously in Figures 3.2c and 3.2f, the KH-Faeth model also predicts an initial near-nozzle SMD decay that better matches experimental measurements at the highest ambient density/pressure. This implies that even at high ambient densities, a turbulent breakup mechanism is still likely to be of relevance.

Although the KH and KH-Faeth models present noticeably different SMD distributions along the spray centerline at many conditions, the liquid dispersion was found to be less deviated from each other. Figure 3.5 shows a comparison of the model-predicted and measured projected density, as measured from x-ray radiography experiments by experimental researchers at Argonne National Lab. These results demonstrate that measurements of projected density alone are insufficient for validation of breakup modeling approaches.

3.2.3 Validation of Radial SMD Distributions: Effect of Secondary Breakup

Figure 3.6 presents SAMR measurements [146] of SMD across Spray D and comparison to the CFD calculations. Preceding section discussed the atomization characteristics predicted by primary breakup models without inclusion of a secondary breakup model. As shown in Figures 3.6a and 3.6b, neglecting secondary breakup (solid lines)

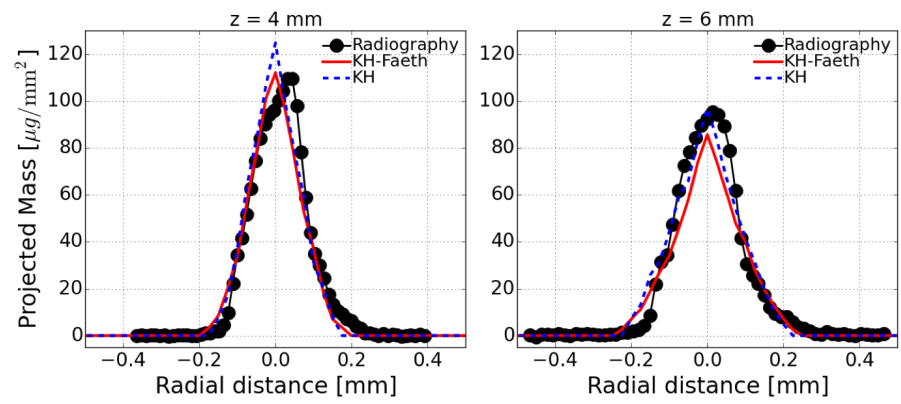

(a) $p_{inj} = 500\ bar$, $p_{amb} = 1\ bar$

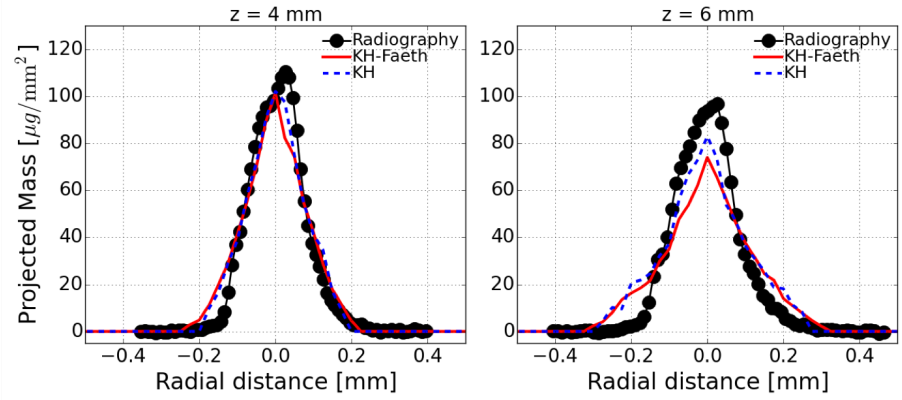

(b) $p_{inj} = 500\ bar$, $p_{amb} = 2\ bar$

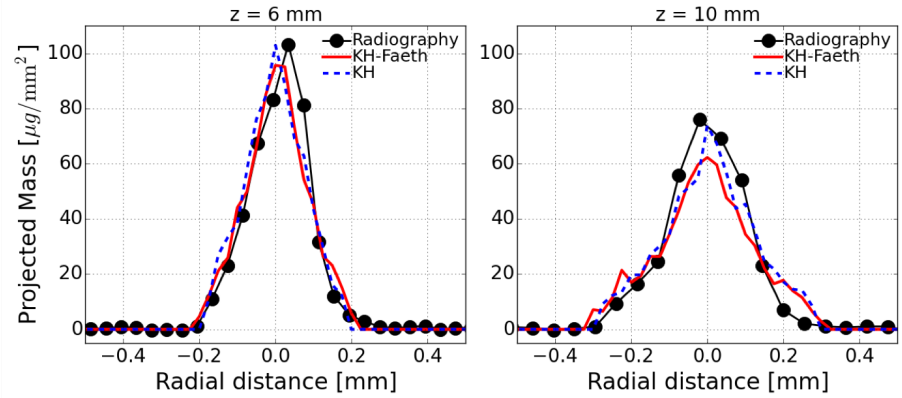

(c) $p_{inj} = 1500\ bar$, $p_{amb} = 1\ bar$

Figure 3.5: *Comparison of predicted and measured spray dispersion at multiple downstream locations as represented by the transverse projected mass density (PMD) distribution: KH model vs. KH-Faeth model*

was found to give rise to large errors in the predicted SMD at the spray periphery. Even though good prediction accuracy is observed along the spray centerline (Figure 3.2), deviation of calculated SMD values from the measurement begins to grow away from the spray axis. This observation motivated an evaluation of whether the use of a secondary breakup model would impact the peripheral droplet size distribution. The resultant SMDs with the commonly employed RT model are indicated by the dashed lines in Figure 3.6. Significant improvements in prediction accuracy are observed near the edges of the spray when the RT model is employed in conjunction with both the KH model and KH-Faeth model, with only a small effect on predicted centerline drop sizes. It is also seen that both the KH model and KH-Faeth model predict similar drop sizes across the spray width as ambient density or pressure is increased, as shown in Figure 3.6b, indicating that secondary breakup may be critical for accurate breakup predictions under higher ambient densities.

However, such an improved accuracy by the use of secondary breakup model appears to be valid under rather lower ambient density conditions; whereas effect of secondary breakup diminishes as the ambient density increases significantly (e.g., p_{amb} = 20 bar) as depicted in Figure 3.6c. In this figure, the solid line and dashed line overlap each other, suggesting that the atomization is completely governed by the primary breakup process; thus, the secondary breakup gives unnoticeable impact on the SMD predictions. This result implies that current approach of the KH instability model used as aerodynamic breakup mechanism in the KH-Faeth model tends to underestimate the droplet sizing quantification and overestimates the relative importance of turbulent breakup at elevated ambient pressure.

3.2.4 Implications of KH-Faeth Model Validations

The present study of KH-Faeth model validation was motivated from the recommendation by the earlier proposed concept for nozzle-generated turbulence primary

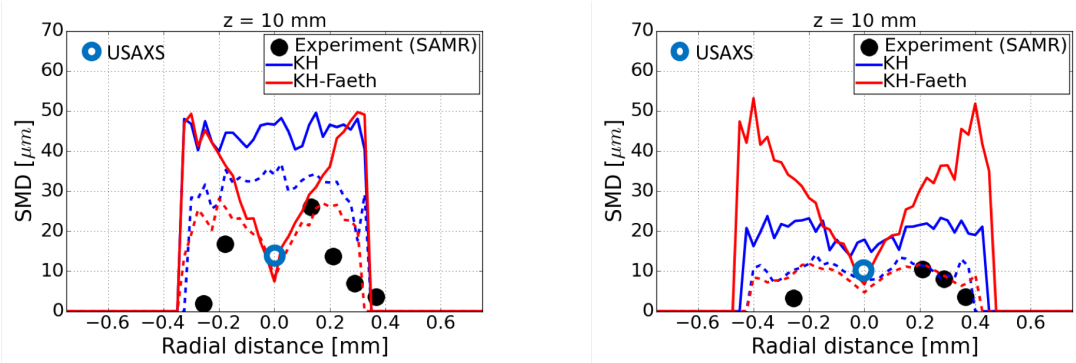

(a) p_{amb} = *1 bar*

(b) p_{amb} = *2 bar*

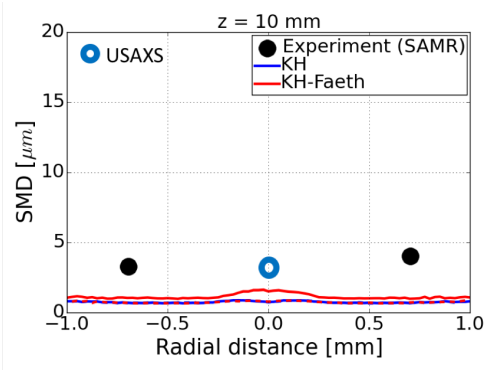

(c) p_{amb} = *20 bar*

Figure 3.6: *Simulated and measured SMD distribution in transverse direction: solid line and dashed line indicate the calculated SMD values with and without secondary breakup (RT model), respectively (p_{inj} = 500 bar)*

breakup modeling [91]; this thesis is thus the first study to extensively explore the KH-Faeth hybrid breakup model against unique diagnostics measurements at broad range of engine operating conditions spanning from LTC regime to HTC regime. The results from the previous sections informed that the KH-Faeth model shows better predictive capability under rather low ambient density conditioned aimed at LTC engines; this is attributed to the fact that the model properly represent the predominance of nozzle-generated turbulence breakup over the aerodynamically induced breakup at low ambient density conditions. However, as the ambient density increases up to the level representing HTC conditions, predictions by the KH-Faeth model give rise to some degree of deviation from the measurement. This implies that aerodynamically

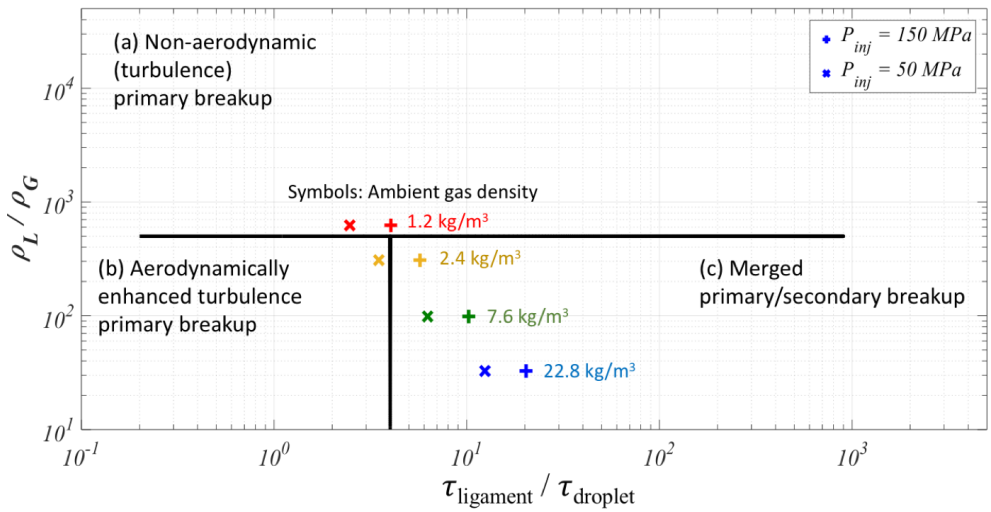

Figure 3.7: *Primary breakup regime diagram with respect to liquid-to-gas density ratio (ρ_l/ρ_g) and breakup time scale ratio ($\tau_{ligament}/\tau_{droplet}$) [30]*

induced breakup may have not been suitably represented by the model assumption; i.e., KH breakup regime may dominate the breakup process at high ambient density conditions. This is evident by finding that the KH-Faeth model and KH model yield consistent model predictions to some extent as shown in Figure 3.6c. For this reason, the aerodynamic breakup assumption by the KH model should be revisited in order to further improve the model accuracy. In addition, it is important to know that the secondary breakup process may play an influential role in SMD predictions at relatively low ambient density conditions as pointed out in Figures 3.6a and 3.6b.

As a modeling guidance to properly improve the model predictivity, therefore, the findings in this study motivate further exploration of the turbulence-enhanced aerodynamic breakup formulations by Wu and Faeth's study [29–31] rather than using KH instability mechanism as the KH model appears to be less predictive especially in drop sizing quantification.

3.3 Multi-Physics Turbulence (MPT) Breakup Model

To be continued with the KH-Faeth model study, this thesis synthesizes in-depth theories behind the breakup mechanisms relevant under a wide range of ambient density conditions in order to provide pathway towards more predictive primary breakup model. Again, in the earlier studies by Wu and Faeth [29–31], three distinctive primary breakup regimes (see Figure 1.4) were identified as a function of droplet liquid to ambient gas density ratio (ρ_l/ρ_g), and characteristics time scale ratio for ligament and secondary droplet formations, as depicted in Figure 3.7. According to their observations, *non-aerodynamic (i.e., turbulence) primary breakup* starts to overcome the breakup by the aerodynamic shear force acting on the liquid jet surface as the liquid-to-gas density ratio (ρ_l/ρ_g) goes above 500. For ρ_l/ρ_g less than 500, they hypothetically presumed that the turbulent eddies in the nozzle flow retain sufficient kinematic energy to protrude the liquid jet surface against the surface tension force. However, in this case, they assumed that the aerodynamics in the vicinity of liquid jet surface accordingly assists the turbulent eddy protrusion by dropping the local ambient pressure down; i.e., *aerodynamically enhanced turbulence primary breakup*. Indeed, they did not consider the KH wave instability phenomena for this aerodynamic effect. Lastly, Wu and Faeth also assumed that, for sufficiently large enough injection velocities, the secondary droplet formation would proceed fast (small $\tau_{droplet}$) enough to consider the secondary breakup process as a merged sub-process of the primary breakup process; i.e., *merged primary/secondary breakup*, where primary breakup (i.e., ligament breakup time by the Rayleigh instability: $\tau_{ligament}$) is the rate-controlling factor.

In this thesis, a new hybrid primary breakup model that allows for these detailed physics of primary breakup mechanisms is proposed upon the basis of KH-Faeth model framework. By incorporating aerodynamically enhanced turbulence breakup

and merged primary/secondary breakup, the new modeling approach is suggested to compensate the range for which the KH-Faeth model may have not properly applied.

3.3.1 Model formulations

The new model (hereafter MPT model) is based on the KH-Faeth model framework meaning that assumption of the nozzle generated turbulence breakup is retained as represented by the length and time scales, L_{Faeth} and τ_{Faeth}, in Equations 2.37, 2.38 and 2.39 without KH model breakup contribution. Therefore, the ligament forming and bursting into droplets by the Rayleigh breakup is assumed to be mainly responsible for onset of primary breakup process; then qualitative change in outcome of the primary breakup varies with relative importance of aerodynamic effect. According to Wu and Faeth [30], the aerodynamic effect can emerge in two different breakup regimes depending on the ligament breakup time $\tau_{ligament}$ as described in the following sections.

3.3.1.1 Aerodynamically Enhanced Turbulence Breakup Regime

As illustrated in Figure 3.8a, there is no significant impact of varying ρ_l/ρ_g from 6230 to 867 on qualitative properties of ligament formation near the liquid jet surface, suggesting that assumption of turbulence eddy protrusion forming the ligaments is still relevant under such an aerodynamic force dominating condition. However, the lowest density ratio condition ($\rho_l/\rho_g = 867$) reveals quantitatively different feature of droplet formation; e.g., droplet sizes are much smaller and number densities become higher than those of higher density ratio cases. This may indicate that the aerodynamic effect is anticipated in forming smaller droplets from the turbulence primary breakup. Wu and Faeth [30] hypothesized that the aerodynamic flow in the vicinity of liquid jet surface promotes pressure drop across the protruding hump generated by the turbulent eddies as illustrated in Figure 3.8b.

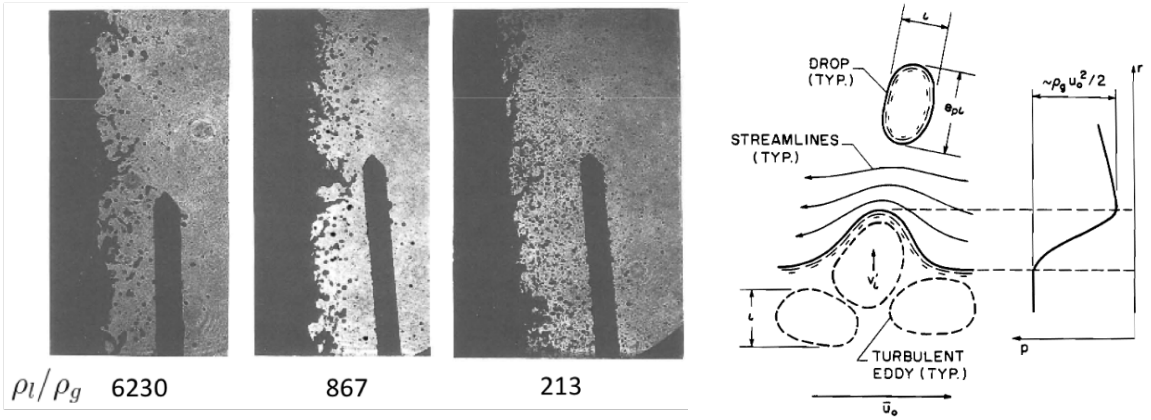

(a) *Photographs of ligaments and droplets formed by varying ρ_l/ρ_g*

(b) *Schematic of aerodynamically enhanced turbulence breakup*

Figure 3.8: *Aerodynamic effect on turbulence primary breakup by Wu and Faeth [30]*

Assuming turbulent eddies with cross-stream velocity, $\overline{v_l'}$, are convected in the streamwise direction at the local mean velocity, $\overline{u}_o$, and the droplets formed by the eddies are assumed to be order of L_{Faeth}, energy conservation responsible for a single droplet formation can be by equating the mechanical energy due to the turbulent eddy and ambient gas acceleration against the liquid surface energy as shown below:

$$\left(\rho_l \overline{v_l'}^2 + C_{sa}\rho_g \overline{u}_0^2\right) L_{Faeth}^3 = C_{sx}\sigma_l L_{Faeth}^2 \tag{3.1}$$

where the model constant C_{sa} is a new empirical value to be adjusted, and C_{sx} is the coefficient adopted in the KH-Faeth model formulation, Equation 2.38. The value of C_{sa} was optimized to 0.04 by Wu and Faeth [30]. To accommodate the effect of aerodynamic mechanical energy as well as the turbulent eddy protrusion and ligament breakup (Rayleigh breakup), the final form of the equation yields as in consistent form of Equation 2.38 with a multiplication factor β:

$$L_{Faeth}\beta = C_{sx}\Lambda\left(\frac{x}{\Lambda We_{f\Lambda}^{1/2}}\right)^{2/3} \tag{3.2}$$

where the multiplication factor β is thus expressed as:

$$\beta = \left[1 + C_{sa}\frac{\rho_g}{\rho_l}\left(\frac{\overline{u}_0}{\overline{v}_0'}\right)^2\left(\frac{\Lambda}{L_{Faeth}}\right)^{2/3}\right]^{3/5} \tag{3.3}$$

Here, Λ is the largest eddy scale, which is assumed to be diameter of liquid jet column in this study, and the protruding velocity $\overline{v_l'}$ is replaced with the characteristic velocity in the inertial sub-range of the turbulence spectrum, $\overline{v_l'} = \overline{v}_0'(L_{Faeth}/\Lambda)^{1/3}$. The turbulent intensity $(\overline{v}_0'/\overline{u}_0)$ is set to 0.058 for fully developed turbulent pipe flow based on the literatures [149, 150]. With the second term determined in bracket, the factor β greater than unity gives an extra impact representing the aerodynamically enhanced primary breakup; e.g., $\beta = 1$ implies the same effect as in Equation 2.38. It should be noted that the solution of L_{Faeth} is difficult to be obtained explicitly; thus the roots of this nonlinear polynomial can be obtained using *bisection* method.

3.3.1.2 Merged Primary/Secondary Breakup Regime

As injection pressure increases for example, aerodynamic effect on the ligament formed by the primary breakup is augmented; thus, time required for the secondary breakup ($\tau_{droplet}$ estimated by Equation 3.4) gets sufficiently short compared to Rayleigh breakup time ($\tau_{ligament}$ estimated by Equation 3.5); thus it is reasonable to assume immediate onset of secondary breakup after primary breakup ($\tau_{ligament}/\tau_{droplet} \gg 1$), therefore the Rayleigh breakup (primary breakup) is the rate controlling factor. This tendency implies that the sequence of primary breakup and secondary breakup can be viewed as a merged process; namely, merged primary/secondary breakup regime. The configuration considered within this primary breakup regime was already illustrated in Figure 1.4c.

$$\tau_{droplet} \sim L_{Faeth}\frac{(\rho_l/\rho_g)^{1/2}}{\overline{u}_0} \tag{3.4}$$

$$\tau_{ligament} \sim \left(\frac{\rho_l L_{Faeth}^3}{\sigma} \right)^{1/2} \tag{3.5}$$

Within this merged primary/secondary breakup regime, the properties of ligament breakup (Rayleigh breakup) should be maintained in the formulation of Equation 3.2 where the aerodynamic effect is already implemented in the multiplication factor β. Then, the secondarily augmented aerodynamic effect is merged into the resulting scale of child droplets from this breakup regime. According to the study by Wu and Faeth [30], the secondary breakup correlation was established by assuming that the secondary droplet size (D_c) is proportional to the thickness of boundary layer formed on the droplet surface by the convecting velocity $\overline{u}_0$. This yields following correlation between length scale ratio between ligament and secondary droplets:

$$\frac{D_c}{L_{Faeth}} = C_s \left(\frac{\rho_l}{\rho_g} \right)^{1/2} \left(\frac{\mu_l}{\rho_l L_{Faeth} \overline{u}_0} \right)^{1/2} \tag{3.6}$$

where C_s is an empirical coefficient to optimize the droplet size against measured quantities and set to unity for simulations conducted in this study. Assuming infinitely immediate onset of secondary breakup, the representative size for the child parcels in the model framework should replace L_{Faeth} with D_c when the ratio becomes less than 1.

3.3.2 Predictions of atomization by MPT Model

Knowing that KH-Faeth model performed greatly in capturing general tendency of SMD distribution with change in ambient pressure, the inclusion of nozzle-generated turbulence breakup in the primary breakup model is relevant. The MPT breakup model follows the consistent physics basis in this context. However, lacking detailed physics under high ambient pressure condition and high injection pressure condition was found to generate some degree of errors especially in predicting SMD within off-

axis regions as already discussed. Therefore, this study was motivated to improve the nozzle-generated turbulence breakup model assumption suggesting MPT model to reflect multiple physics that may be encountered across a broad engine relevant conditions.

Figure 3.9 shows comparison between KH-Faeth model and MPT model in estimating the Sauter mean diameter (SMD) distribution along the spray axis against USAXS measurements. It is obvious to find that the MPT model estimates slightly lower SMD values than those of KH-Faeth model; it is possibly due to the fact that the MPT model reflects additional aerodynamic effects on turbulence primary breakup. Indeed, the KH-Faeth model includes the KH model assumption responsible for the aerodynamic effect (wave instability) and the KH breakup regime may often take part in the atomization, whereas the MPT model does not follow the same rule; i.e., onset of primary breakup is solely promoted by the turbulence flow effect and then the aerodynamic impact is assumed to enhance the turbulence breakup or promote fast secondary breakup. In this aspect, it can be stated that the aerodynamic effect implemented in the MPT model tends to outweigh the aerodynamically induced KH breakup in general. Nevertheless, the SMD predictions exhibit acceptable agreement with the measured values by USAXS diagnostics across the conditions employed in this study. These results suggest that the proposed MPT model may improve the predictive capabilities of engine simulations as much as KH-Faeth model can do.

Recall that the KH-Faeth model produced some degree of inaccuracy in SMD predictions at radially farther locations away from the spray axis in Figure 3.6. In the same figures, the inclusion of secondary breakup model was required for better capturing the off-axis droplet statistics. However, as the surrounding gas is characterized by high density flow, the inclusion of secondary breakup become unnoticeable and both KH model and KH-Faeth model consistently underestimates the SMD values, which might be attributed to the irrelevance of KH model assumption as an

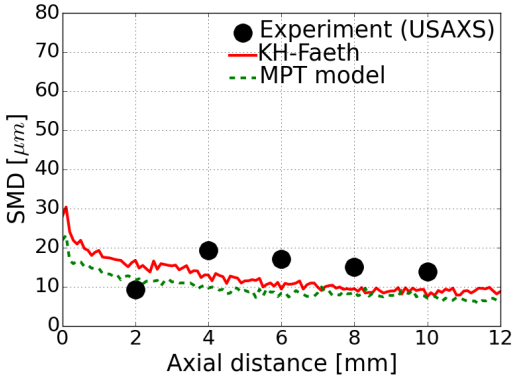

(a) p_{inj}=500 bar, p_{amb}=1 bar

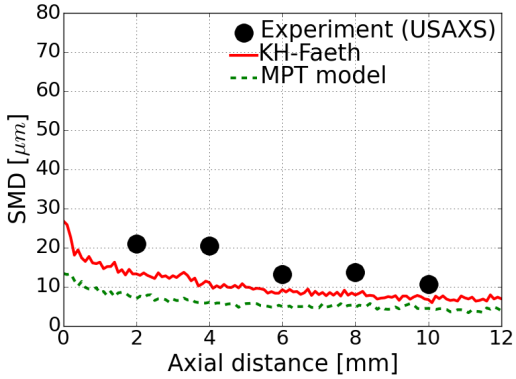

(b) p_{inj}=500 bar, p_{amb}=2 bar

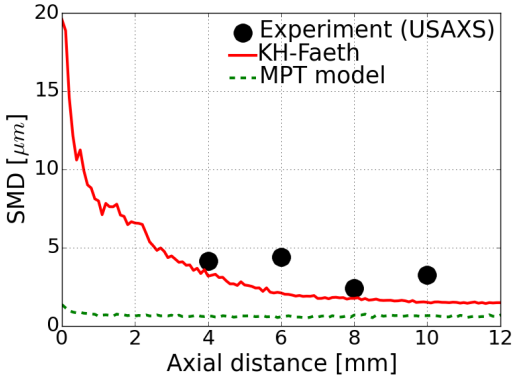

(c) p_{inj}=500 bar, p_{amb}=20 bar

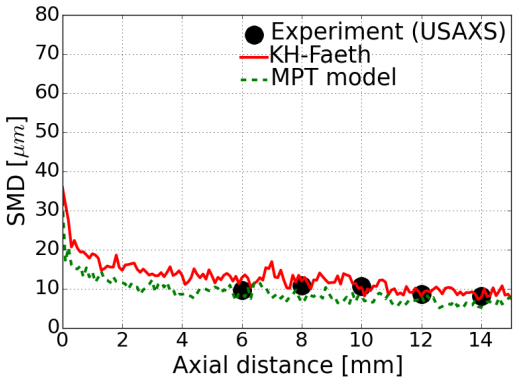

(d) p_{inj}=1500 bar, p_{amb}=1 bar

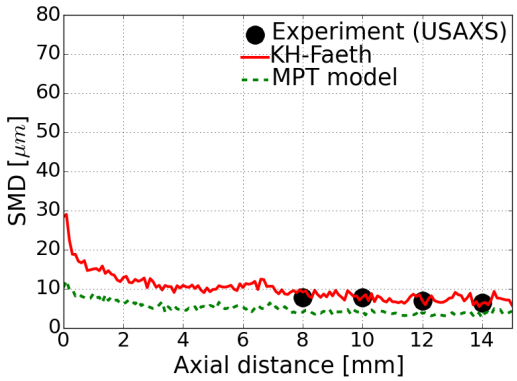

(e) p_{inj}=1500 bar, p_{amb}=2 bar

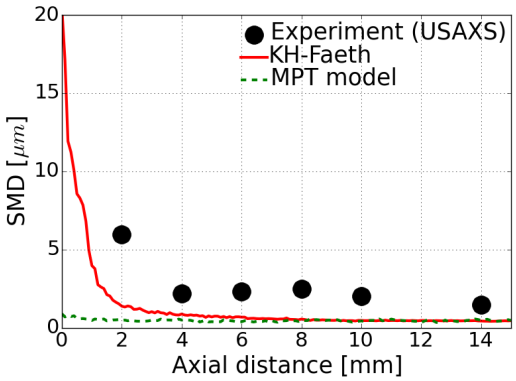

(f) p_{inj}=1500 bar, p_{amb}=20 bar

Figure 3.9: *Comparison between predicted and measured (USAXS) SMD distributions along the spray centerline of ECN Spray D*

aerodynamically induced breakup. For this reason, the MPT model is proposed to modify the aerodynamic breakup assumption; the model assumes that the primary breakup is primarily promoted by the turbulence breakup, then further consideration of multi-physics breakup regimes (e.g., aerodynamically enhanced turbulence breakup and merged primary/secondary breakup regime) allows for aerodynamic effect on the primary breakup process. As a result, the corrected SMD predictions by using the MPT model are illustrated in Figure 3.10. In this test, both models were not set up with consideration of secondary breakup modeling. A promising improvement by the MPT model can be seen in Figure 3.10c. Under the notion that major inaccuracy was found under high ambient density condition, it can be argued that the inclusion of aerodynamically assisted primary breakup regimes allows to capture moderate level of SMD predictions especially in transverse direction. However, complete verification of the model may have not been obtained yet since the results exhibit some degree of deviation of SMD predictions off the measurement. There may also be uncertainties in SAMR measurements as well inherently due to the challenge in injector alignment issue as pointed out in detailed analysis on this diagnostics [146].

It is interesting to find local minima of SMD values along the spray axis from both models, whereas the KH model did not exhibit such a pattern in Figure 3.6. Such local minima appear to be close to the values of USAXS measurements except for the high ambient density condition in Figure 3.10c. However, lack of complete resolution of measurements across the spray axis may leave this pattern of local minima still in many unanswered questions. In order to fully justify the representativeness of the primary breakup process, the models need to be further explored against spatiotemporally measured droplet statistics.

Figure 3.11 shows projected mass density (PMD) results reproduced by the KH-Faeth model and MPT model in comparison to x-ray radiography measurements conducted by researchers at Argonne National Laboratory. As previously pointed

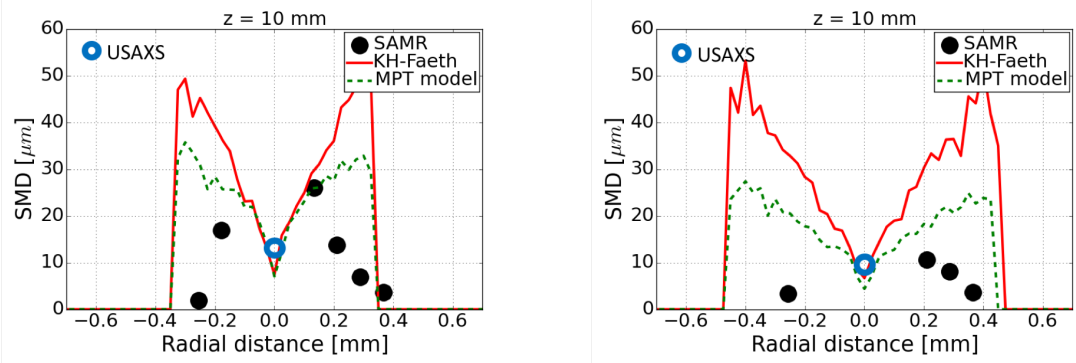

(a) p_{amb} = *1 bar*

(b) p_{amb} = *2 bar*

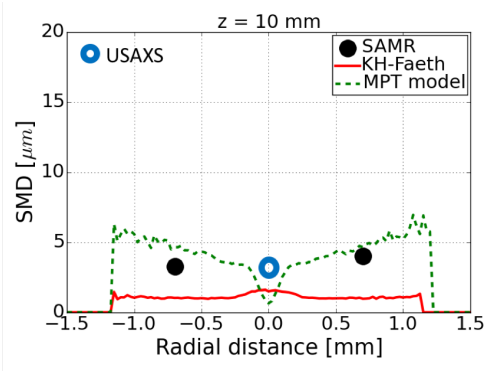

(c) p_{amb} = *20 bar*

Figure 3.10: *Model prediction comparison between KH-Faeth model and MPT model in capturing transverse SMD distributions against SAMR measurement. (p_{inj} = 500 bar); No secondary breakup model used.*

out, the PMD results alone may not be sufficient to demonstrate the model prediction capability since they exhibit somewhat consistent level of values regardless of the model choice. Nevertheless, the PMD results calculated by MPT model are found to be within closer agreement with measurements as the region of interest goes downstream; e.g., PMD values evaluated at z = 10 mm in Figure 3.11c gives best match with the experiment.

3.3.3 Implications of MPT Model Validations

This study demonstrates the predictive ability of a newly proposed primary breakup model, termed the multi-physics turbulence (MPT) breakup model, against the ex-

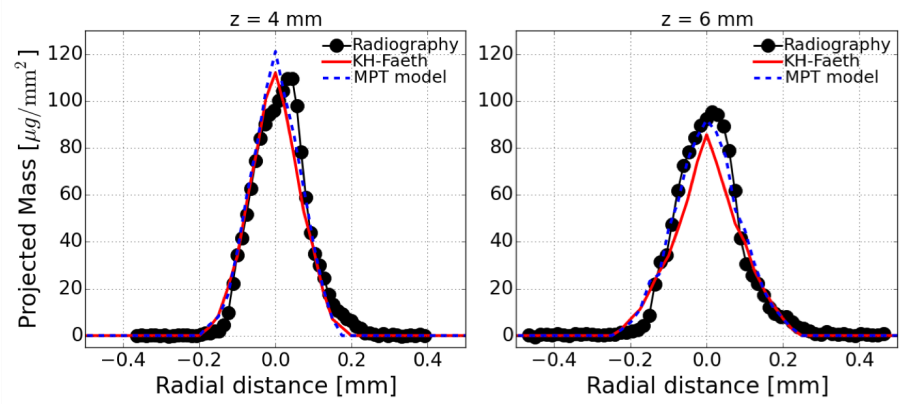

(a) $p_{inj} = 500\ bar$, $p_{amb} = 1\ bar$

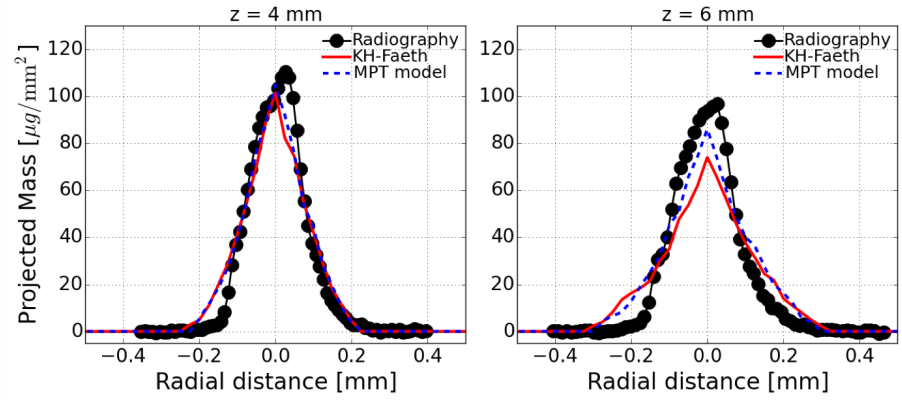

(b) $p_{inj} = 500\ bar$, $p_{amb} = 2\ bar$

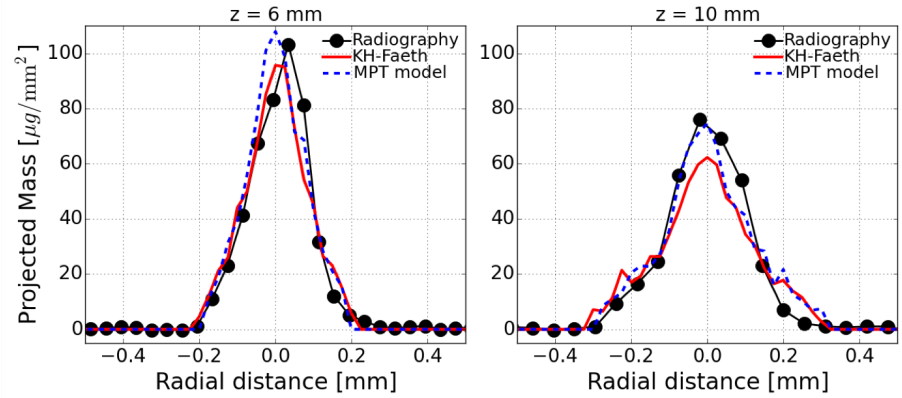

(c) $p_{inj} = 1500\ bar$, $p_{amb} = 1\ bar$

Figure 3.11: *Comparison of predicted and measured spray dispersion at multiple downstream locations as represented by the transverse projected mass density (PMD) distribution: KH-Faeth model vs. MPT model*

isting KH model and KH-Faeth model. The MPT model is an extended version of KH-Faeth model in the aspect that the nozzle-generated turbulence induced primary breakup is taken into accout for a primary mechanism of the liquid jet mass disintegration. One thing in this model that differs from the KH-Faeth model comes from the assumption of aerodynamic effect on the breakup process; MPT model integrates the aerodynamic effect into the sub-process of turbulence primary breakup; thus the aerodynamic effect plays a role in enhancing the turbulence breakup.

A major model improvement was allowed from the test under high ambient gas density condition where the impact of aerodynamic force may be significant. In the previous attempt with the KH model and KH-Faeth model, both models tend to underestimate the mean droplet size compared to the measurement and such an inaccuracy may be attributed to inability of the models for representing the relevant aerodynamic effect with sole assumption of the KH wave instability. However, additionally considered breakup regimes that were identified by Wu and Faeth's earlier study [30] are believed to enable better representativeness of nozzle-generated turbulence primary breakup process.

Despite some degree of improvement, further examinations may be required to completely justify the model predictive performance. The combination of USAXS and SAMR techniquess has provided relevant platform of model validation study. Indeed, since those techniques are relatively new and unique, sufficient experimental data set for the droplet statistics have not been established yet in satisfaction. Also, as pointed out in the recent USAXS and SAMR literatures [91, 146], some level of uncertainties may exist in regard to injector alignment and detailed measurement procedures. Nevertheless, general tendency obtained by the two new models, KH-Faeth model and MPT model, suggests that proper consideration of nozzle generated turbulence breakup process in the modeling aspect is essential for developing advanced engine simulation strategies.

CHAPTER 4

PRELIMINARY STUDY ON END-OF-INJECTION (EOI) COMBUSTION DYNAMICS

While numerous earlier literatures have focused on diesel spray and combustion dynamics during initial period of unsteady physics and quasi-steady injection period, to the author's knowledge none of multi-dimensional computational studies in the past have dealt with combustion dynamics associated with end-of-injection (EOI) transients. However, an importance of EOI transients was demonstrated in terms of enhanced turbulent mixing in the vicinity of nozzle injector by Musculus and Kattke [151], and recently only a few literatures by Knox and co-workers [61, 64] experimentally explored EOI transient impact on flame dynamics; e.g., combustion recession. The authors of these literatures also conducted reduced-order modeling analysis using one-dimensional transient gas-jet mixing model integrated with detailed n-dodecane kinetics. However, multi-dimensional unsteady characteristics of such phenomenon still remain largely unknown.

The study presented in this section is the first multi-dimensional computational analysis on the EOI transient and its impact on turbulent mixing and combustion recession behavior by using research-grade CFD tool package. The following sections present the modeling methodology used in this analysis and provide some degree of insights into the unsteady combustion dynamics during EOI transients, and ultimately provide guidance of multi-dimensional modeling strategy for combustion recession study.

Table 4.1: *Test conditions for ECN Spray A non-reactng spray and reacting spray combustion problems*

Test configuration	**Non-reacting flow**	**Reacting flow**
Fuel	n-Dodecane	
Nozzle orifice diameter [μm]	90	
Fuel temperature [K]	363	
Injection duration [ms]	1.5	
Injected fuel mass [mg]	3.5	
Injection pressure [MPa]	150	
Ambient gas temperature [K]	900	800 / 900 / 1,000
Ambient gas density [kg/m^3]	22.8	
Ambient gas composition [% by volume]	N_2: 89.71% CO_2: 6.52 % H_2O: 3.77 %	O_2: 15% N_2: 75.15% CO_2: 6.23 % H_2O: 3.62%

4.1 CFD Model Setup and Test Conditions

In this study, Eulerian-Lagrangian framework integrated in the open-source CFD software OpenFOAM (v2.4.0) [84] was deployed for three-dimensional simulations; Reynolds-averaged Navier-Stokes (RANS) with realizable $k-\epsilon$ model [152] for modeling turbulent flow in Eulerian coordinate, and a stochastic modeling for injected spray particles using a Rosin-Rammler distribution function in Lagrangian manner. For representing atomization process, KH-RT breakup model [76] was used without consideration of droplet-droplet interactions; e.g., collision and coalescence. The partially-stirred reactor (PaSR) combustion model was used to account for turbulence chemistry interactions.

Table 4.1 outlines the ECN Spray A test conditions for non-reacting and reacting single-hole diesel sprays used as a reference case for validation of the employed CFD sub-models. The non-reacting spray was used for validating spray sub-models and grid sensitivity test, and a few conditions of reacting spray were also considered primarily for combustion recession simulations. The injector orifice boundary condition for the

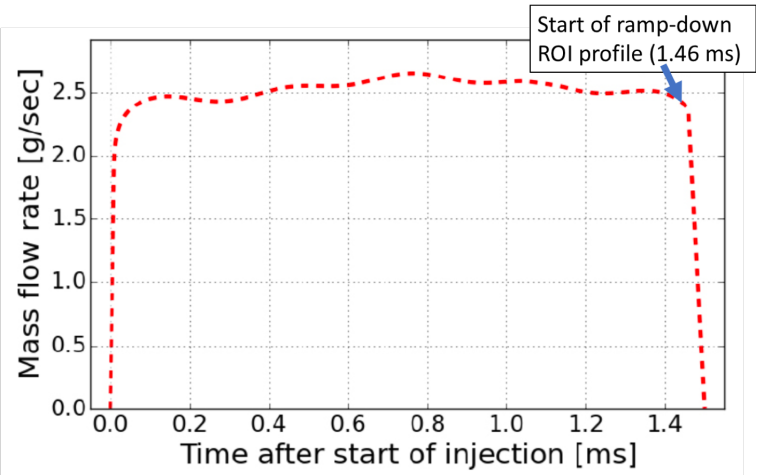

Figure 4.1: *ECN Spray A injection boundary condition: Rate of injection (ROI) profile with 1.5 ms injection duration and indicated start of ramp-down profile at 1.46 ms*

spray simulation utilizes the nominal Spray A injection profile provided by the ECN and is illustrated in Figure 4.1. The primary analysis of combustion recession will be presented with respect to the end-of-injection (EOI) transient. To this end, the start of ramp-down (SOR) profile is specified at 1.46 ms in the figure.

4.1.1 Grid Sensitivity and Spray Model Validation

The computational domain configuration used in this study is a three-dimensional non-uniform structured grid with clustering grid spacing in spray axis direction (z-direction); minimum grid scaling is applied in the vicinity of injector nozzle position then grid size gradually increases in z-direction as illustrated in Figure 4.2. Four different grid resolutions were investigated with a factor of 1.5–2 variation in the cell size, as listed in Table 4.2.

The computational modeling setup in this study was first validated under non-reacting conditions (i.e., inert gas mixture composition) against measurements of liquid length and vapor penetration length in Figure 4.3. In this analysis, the liquid length is defined as the location of 95% accumulated liquid mass and the vapor length is defined as the furthest axial location from the injector where the mixture fraction

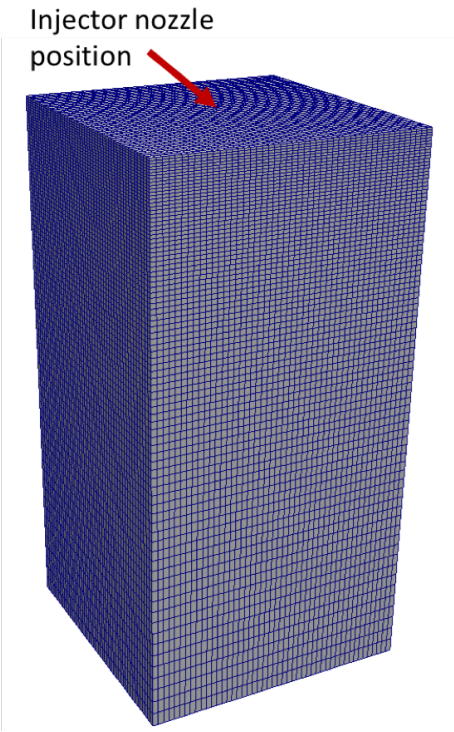

Figure 4.2: *Configuration of computational domain with baseline grid resolution*

Table 4.2: *Employed grid resolutions for grid sensitivity study (size unit [mm])*

Mesh density	**Min cell size**	**Max cell size**	**No. of cells**
Base	0.55	1.40	960,000
Fine	0.36	1.80	960,000
Intermediate	0.73	1.80	403,200
Coarse	1.0	2.70	12,000

reaches above 10^{-4}; in this non-reacting case, the mixture fraction is equivalent to fuel mass fraction as the fuel-originated hydrogen and carbon species are only contained in fuel vapor.

The predicted temporal development of the quasi-steady liquid length with the baseline grid shows a good agreement with the experimental results within some degree of error range, although some discrepancies exist during the early unsteady period of injection. Prior several attempts of simulations with varying KH-RT model constants for the baseline grid yielded the best agreement with the measurement for

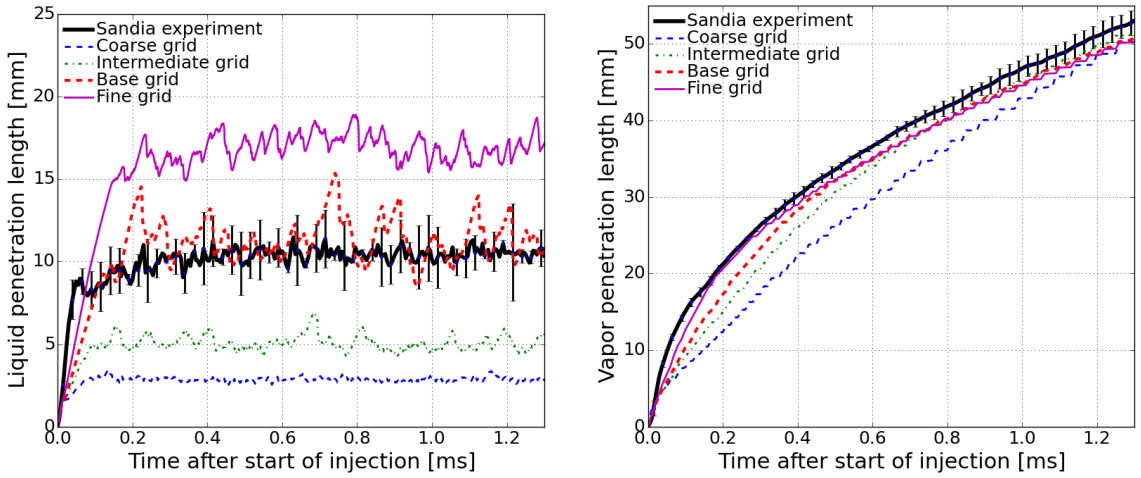

(a) *Liquid penetration length* (b) *Vapor penetration length*

Figure 4.3: *Grid sensitivity analysis and comparison of model predictions for liquid length and vapor length against ECN measurement [92] (Sandia experiment)*

$B_1 = 13$ defined in Equation 1.2 with this model setup. However, the discrepancies between the predicted liquid length and measured ones with the other mesh setups are significant. Thus, subsequent simulations for reacting diesel spray were conducted consistently with the baseline grid setup.

4.1.2 Chemical Kinetics Models in Consideration

The use of partially-stirred reactor (PaSR) model allows to use detailed chemical kinetics model for evaluating the reaction rate source terms in species balance equations. In this investigation, two reduced chemical mechanisms for n-dodecane fuel are incorporated in the simulation setup; namely Cai mechanism [153] and Yao mechanism [154]. The Cai mechanism which is a reduced mechanism from reoptimization of Narayanaswamy [155]'s detailed mechanism considers 57 species and 197 reaction steps. The Yao mechanism, which was calibrated against ECN Spray A condition, consists of 54 species and 268 reaction steps. In terms of number of species and reaction steps, these two mechanisms are considered computationally viable for the present research-level study.

Figure 4.4 compares estimated ignition time delay and flame lift-off length of the diesel spray flame by two different chemical mechanisms in consideration. In this investigation, while Cai mechanism was used for simulation with varying ambient temperature, Yao mechanism was used solely for a single temperature condition, i.e., T_{amb} = 900 K. The ignition delay time and flame lift-off length were evaluated by the time and axial location at which Favre-average OH mass fraction reaches 2% of the maximum within the computational domain after a stable flame is established according to the ECN recommendation [92]. As shown in Figure 4.4a, Cai mechanism slightly overestimates the ignition delay time for an ambient temperature of 900 K; however, it closely matches the experimental data at T_{amb} = 1,000 K. Yao mechanism underpredicts the ignition delay time at 900 K. Cai mechanism overpredicts the ignition delay time for lower ambient temperature; e.g., 800 K.

Figure 4.4b demonstrates the predicted and experimental data for flame lift-off length for consistent conditions. Similar to the trend shown in Figure 4.4a, Cai mechanism slightly overpredicts the flame lift-off length at 900 K, with a more significant over-prediction at 800 K. The lift-off length is underpredicted for the highest temperature, i.e., 1,000 K. It may be stated that Cai mechanism may not precisely predict the ignition delay time and flame lift-off length at relatively lower ambient temperatures. This might be due to the fact that eliminating and/or lumping the reactions from the detailed mechanism inversely affects the low temperature predictions of the reduced chemical mechanisms. On the other hand, both reduced mechanisms show a relatively acceptable agreement with the experiments in terms of ignition delay time and flame lift-off length at higher ambient temperatures. The predictive capabilities of both Cai and Yao mechanisms in predicting the combustion recession near the nozzle will be discussed later.

To fully characterize the chemical kinetics in terms of ignition behavior with respective equivalence ratio ϕ, several simulations of zero-dimensional constant volume

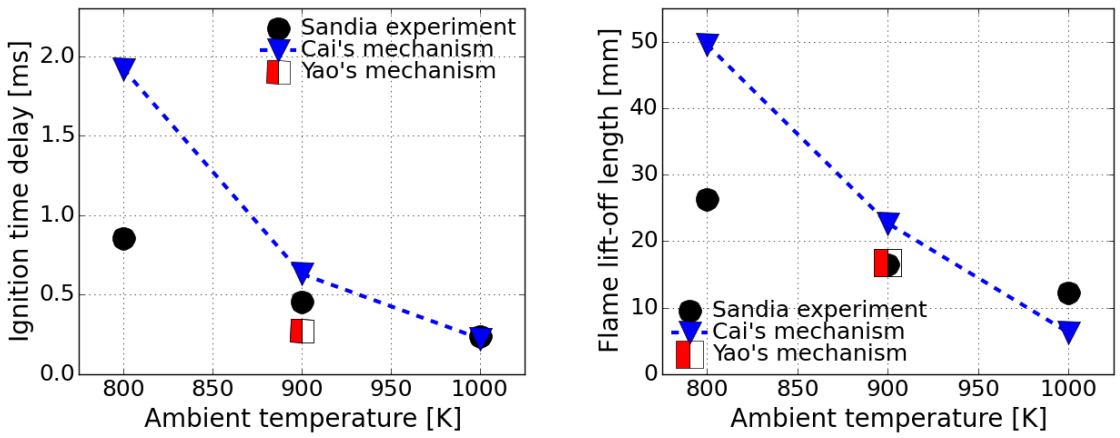

(a) *Ignition delay of spray flame* (b) *Flame lift-off length*

Figure 4.4: *Validation of predicted ignition time delay and flame lift-off length in diesel spray flame using Cai mechanism [153] and Yao mechanism [154]*

batch reactor were performed. Figure 4.5a plots ignition time for first stage (dashed line) ignition and second stage (solid line) ignition evaluated by tracking temporal temperature rise with different chemical mechanisms considered. The first order time derivative of temperature may produce two peaks for each event. The first and second peaks at which temperature rises are associated with first and second stage ignition delay times. In this calculation, it is assumed that the mixture temperature is a function of equivalence ratio for constant pressure and adiabatic mixing of fuel and oxidizer. Thus, the variation of ϕ also corresponds with a variation of mixture temperature. In the results, the Yao mechanism tends to initiate first stage ignition later than that of the Cai mechanism over all conditions, while the second stage ignition which is primarily responsible for spray flame ignition delay starts earlier than the case of Cai mechanism especially for $\phi < 2$. In the notion that diesel spray flame burning generally begins at around $\phi \sim 2$ promoting the mixture burning nearby, this finding is quite consistent with the previously observed spray ignition delay seen for Yao mechanism in Figure 4.4a.

The heat release rate and temperature versus time is plotted in Figure 4.5b based on the batch reactor simulations conditioned at $\phi = 1.5$, which is likely responsible

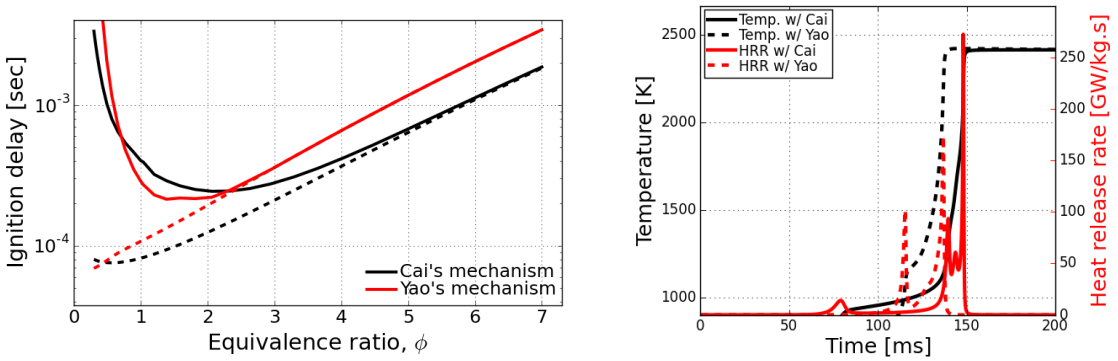

(a) *Ignition delay versus equivalence ratio (dashed: 1st stage ignition, solid: 2nd stage ignition)*

(b) *Temporally resolved heat release rate for $\phi = 1.5$*

Figure 4.5: *Results of constant volume batch reactor simulation calculations conditioned at $p = 6$ MPa, 15% Oxygen level, $T_{fuel} = 363$ K and $T_{amb} = 900$ K, Unburned mixture temperature varies with fuel-air ratio.*

for primary spray flame ignition. From the result, the Cai mechanism has a shorter first stage ignition corresponding to the first initial rise of the heat release rate (small bump found at $t = 75$ ms), whereas the Yao mechanism produces first rise of heat release at $t = 120$ ms. However, reaction from the Yao mechanism undergoes shorter time duration (120 ms - 140 ms) for the low-temperature kinetics initiating high temperature kinetics earlier than Cai mechanism, which is consistent observation shown in Figure 4.5a. However, it is important to find that heat release rate at the peak temperature rise is lower for the Yao mechanism; this behaviormay suggest important implications for the prediction of combustion recession as will be demonstrated later.

4.2 Preliminary Results of Combustion Recession Simulations

The following sections assess the ability of RANS modeling with employed chemical mechanisms for predicting unsteady characteristics of combustion recession subject to EOI transients under ECN Spray A operating conditions. Using these results, more in-depth investigations are presented to further explore the driving physics of the combustion recession behavior.

4.2.1 Analysis of Predicted Combustion Recession

Figure 4.6 compares the ground-state OH mass fractions and temperature contours from the current RANS modeling setup with Cai mechanism for chemistry against high-gain chemiluminescence snapshots of the excited state OH radical (OH*) under one of the listed conditions in Table 4.1; $T_{amb} = 900$ K. In principle, the ground-state OH and chemiluminescence OH* may not be comparable since evident differences between OH* chemiluminescence with a limited lifetime and longer lived ground-state OH planar laser-induced fluorescence (PLIF) in flame structure were identified in the experiments of Maes et al. [156]. They observed that OH appeared slightly upstream and more radially extended from the spray central axis compared to the earliest time that OH* was detected. Therefore, in general, the best practice is to include OH* in the chemistry modeling. However, since OH* is not included in the present chemical mechanism setup, the comparative contours in Figure 4.6 may be rather qualitative. Moreover, the chemiluminescence in the experimental snapshots were intentionally saturated to portray the relatively weak signal that arises during combustion recession in the region between the nozzle and the flame lift-off length (LOL). Thus, the red contour indicates chemiluminescence set to 50% of the intensity at the mean LOL. It should also be noted that the low-level speckled signal (light blue color) seen near the injector nozzle is likely due to signal noise and/or background reflections and thus should not be interpreted as chemiluminescence from high temperature ignition. In general, at comparable times after SOR, the RANS predicted behavior of combustion recession shows "qualitatively" comparable location of detecting ignition zone with experiments.

It is important to know that the RANS simulations predict Favre-averaged scalar fields, while the experimental images are single instance of projected beam shot; thus, the sub-grid scale turbulent mixing and reaction inhomogeneities that are captured in the single-shot experimental image may not be replicated in those RANS simulations.

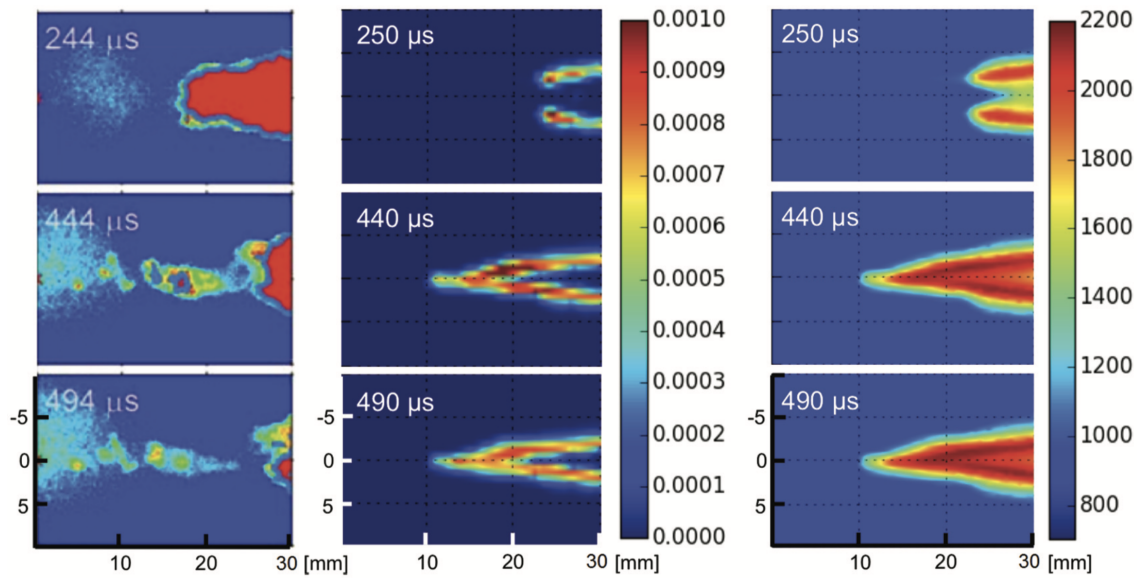

Figure 4.6: *Snapshots of experimentally observed and numerically predicted combustion recession behaviors: (left) Chemiluminescence images of Spray [61] after SOR compared with (middle) predicted OH mass fraction and (right) predicted temperature contours from RANS simulations with Cai mechanism. Ambient temperature, T_{amb} = 900 K. Spray is injected from left to right horizontally; the horizontal axis shown in the figures denotes the distance from injector (x=y=0 mm).*

Rather, the RANS simulations most closely represent the ensemble average of the measurements. From this perspective, it can be argued that the RANS simulations well replicate the statistical extents of combustion recession event characterized by multiple snapthos of flame visualization. For this reason, if such multiple experimental realizations were allowed, the ensemble average of those quantities would appear more similar to the RANS simulations, with a more uniform distribution of OH* upstream of the LOL as combustion recession process proceeds. However, tiny scale of ignition kernels (yellow to red colors from 444 μs to 494 μs upstream of $z = 10$ mm) detected by chemiluminescence were not captured by the present modeling setup, suggesting that sub-grid scale mixing and combustion physics are important subject to be considered for advanced TCI modeling strategy.

Based on this success, further investigation may provide in-depth fundamentals of combustion recession dynamics in terms of mixing and chemical kinetics. To this

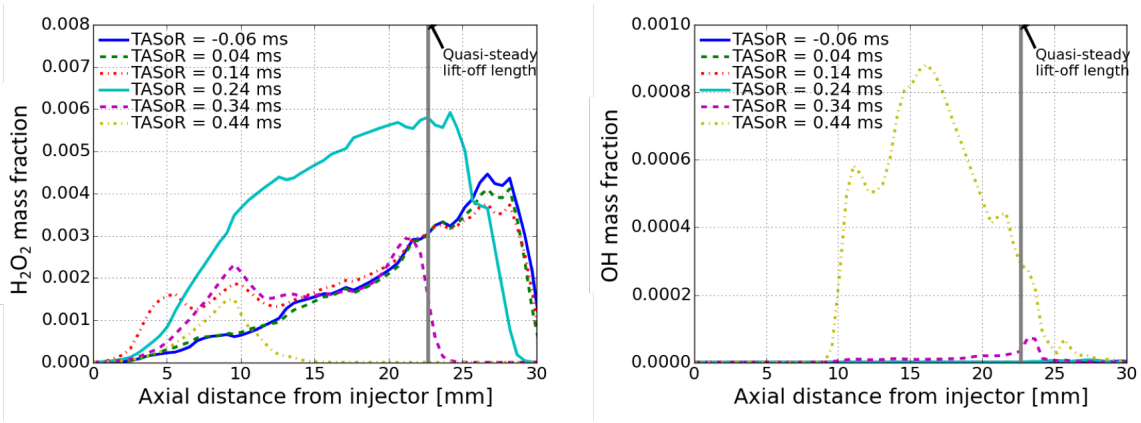

(a) *H_2O_2 mass fraction* (b) *OH mass fraction*

Figure 4.7: *Calculated mass fraction of H_2O_2 and OH along the spray axis at different time after start of ramp-down (t_{ASOR}) with Cai mechanism.*

end, Figure 4.7 further illustrates the ignition sequence during combustion recession with respect to the time instance of start of ramp-down (SOR). Prior to 0.44 ms after SOR, hydrogen peroxide (H_2O_2) is seen throughout mixture upstream of LOL, and the quantity of OH radicals is very low. Since H_2O_2 is a key species produced by cool-flame reactions [49], this suggests that mixtures upstream of LOL has undergone first stage (low-temperature) ignition process. On the other hand, at $t_{ASOR} = 0.44$ ms, H_2O_2 is almost consumed and simultaneously OH concentration immediately rises, meaning that the mixtures have reached second stage ignition and yielding combustion recession.

While the near-nozzle mixtures are leaning by air entrainment and approaching their most ignitable thermodynamic state after EOI, the competition between chemical and mixing timescales ultimately dictates whether combustion recession occurs. To gain insights into this process, values of special Damköhler number (Da) have been quantified along the spray axis and their temporal change in time are illustrated in Figure 4.8. The Da number is defined in this study as $Da = \tau_r/\tau_c$, where τ_r and τ_c are the flow residence time and chemical time scale, respectively. The chemical time scale was determined by the second stage ignition time delay of elements of mixture along

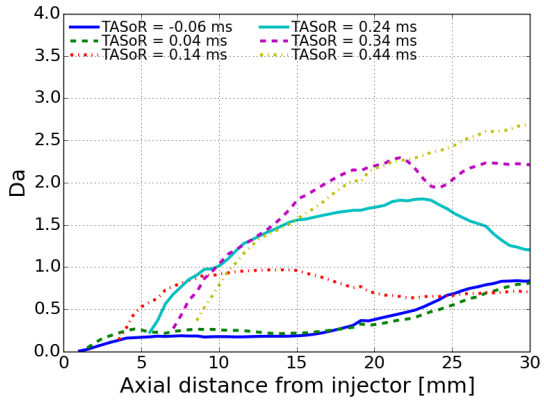

Figure 4.8: *Damköhler numbers along the spray axis modeled with Cai mechanism after SOR*

the spray axis based on their local instantaneous temperature and equivalence ratio. To quantify this value, precomputed data set of constant pressure (6 MPa) batch reactor simulations was used. The mixture temperature for these calculations was obtained by assuming adiabatic mixing between fuel and air based on the equivalence ratio. Also, the flow residence time τ_r for a given computational cell along the spray axis is quantified by estimating the required time for the given mixture to travel from the injector nozzle to the position where the equivalence ratio is measured. For simplicity, the local gas velocity is used to estimate this time as: $\tau_r = x/u_{\text{gas}}(x)$, where $u_{\text{gas}}(x)$ denotes the gas-phase velocity at that axial distance from the injector tip. This approximation assumes that the velocity is constant from the nozzle to the axial location x and may overestimate the true flow residence time. Likewise, estimates of the chemical residence time from batch reactor simulations are also likely to be overestimated since mixtures within the computational cells have already undergone the first stage ignition prior to EOI. The purpose of this simple scaling analysis is to provide estimations of local balance between chemical and mixing timescales to better understand the transient competition between EOI entrainment and ignition that controls combustion recession.

The axial locations upstream of the quasi-steady LOL (22.7 mm for Spray A

conditions with the Cai mechanism) where Da exceeds unity can be interpreted as regions that the flow residence time is long enough to promote ignition. These regions are prone to combustion recession occurring. The value of Da increases with time after SOR in the near-nozzle region and first exceeds unity at 0.24ms near 10mm from the injector nozzle. The present simulations predict that second-stage ignition within the near-nozzle mixtures first occurs downstream of 10 mm, consistent with regions where $Da > 1$. but slightly later than the time Da first exceeds unity, the value of Da for $x < 10$ mm does not reach unity again, indicating that chemistry is too slow, and/or the flow timescales are too fast to promote ignition, and combustion recession is not predicted to occur in these regions.

4.2.2 Assessment of Chemical Mechanisms In Combustion Recession Predictions

Previous literature findings [61, 64] on combustion recession suggest that primary characteristics of combustion recession is strongly driven by autoignition process of ignitable mixture, so it is expected that the chemical mechanism employed will significantly influence predictions of combustion recession. The present investigation explores the choice of chemical mechanisms in terms of predictive capabilities in capturing experimentally observed combustion recession process.

Figure 4.9 shows predicted temperature contours and superimposed flow streamlines for Spray A at different instances in time during the EOI process, given in time after SOR (ASOR). As consistent with the LOL predictions in Figure 4.4b, the very left two snapshots in upper and lower rows illustrate quasi-steady LOL captured at t_{ASOR} = -0.06 ms; the LOL by the Cai mechanisms is predicted longer than that of Yao mechanism. One possible reason behind this tendency can be explained by finding retarded ignition delay (see Figure 4.4a) and accordingly longer mixing residence time.

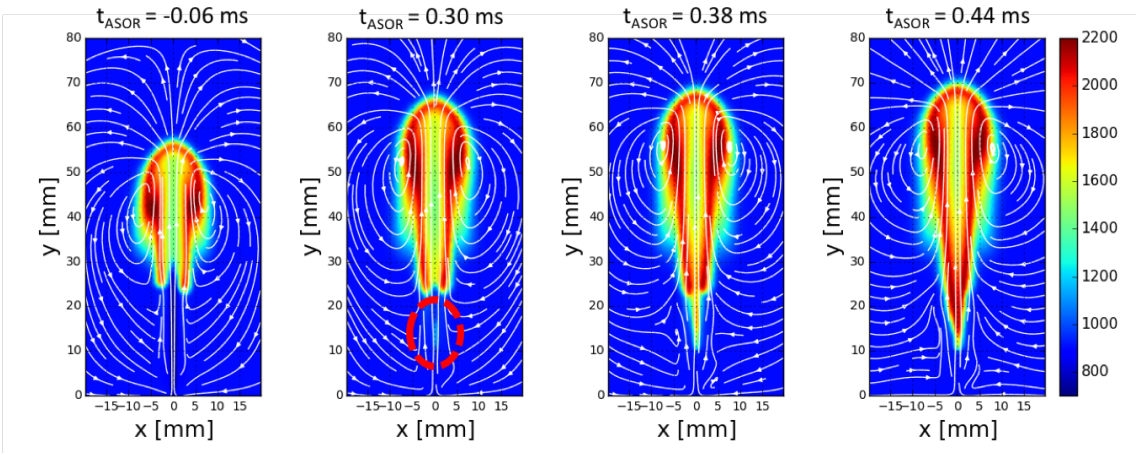

(a) *Cai mechanism*

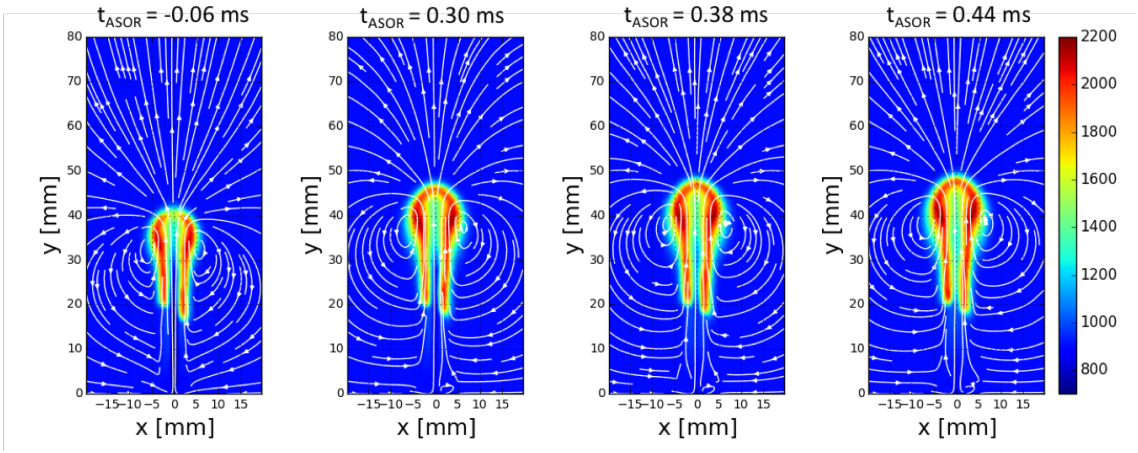

(b) *Yao mechanism*

Figure 4.9: *Predicted temperature contours and superimposed streamlines during quasi-steady injection and after SOR for Spray A using (Upper row) Cai mechanism and (Lower row) Yao mechanism under ECN Spray A condition with T_{amb} = 900 K.*

At t_{ASOR} = 0.3 ms, the simulation with Cai mechanism exhibits an initiation of high-temperature ignition (scaled around 1,300 K) in an isolated region (highlighted in red dashed line in Figure 4.9a) upstream of the lifted flame sitting at LOL distance. This prediction reproduces the separated combustion recession regime identified at the same condition by earlier experiment [64], where isolated autoignition pockets are observed during or after EOI in mixtures upstream of the LOL. Later on, the temperature of separated autoignition pocket continues to rise, indicating second stage ignition ($T >$ 2,000 K), and the ignited mixture grows radially and merges

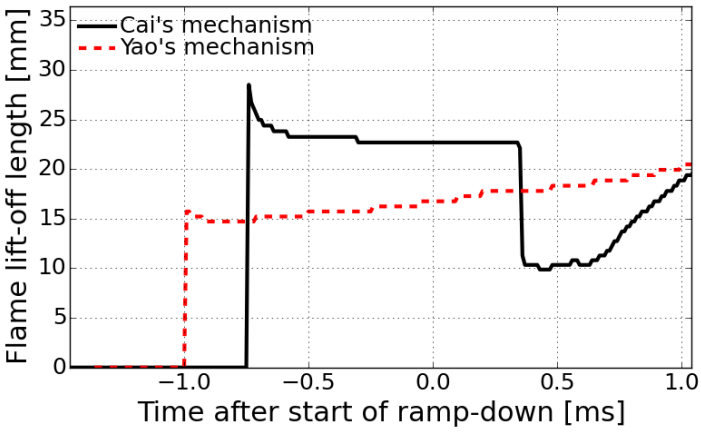

Figure 4.10: *Predicted LOL for Spray A with Cai and Yao mechanisms with respect to time after SOR*

with the lifted flame. Finally, at $t_{ASOR} = 0.44$ ms, the initially separated reaction regions are completely merged, and the shortened LOL become obvious. In contrast, simulation with Yao mechanism in Figure 4.9b indicate that the flame slightly extends axially and radially in time, but no evidence of combustion recession is detected at this condition.

Figure 4.10 temporally tracks the transient LOL throughout the entire combustion event for the condition displayed in Figure 4.9. The rapid drop of LOL from 22.7 to 10 mm for the Cai mechanism is a strong indicator of combustion recession. The extended flame towards injector sits at that position for a short period of time (~ 0.25 ms), then the flame starts to convect downward at 0.7 ms after SOR. However, as the Yao mechanism setup fails to capture combustion recession at the same condition, the LOL in Figure 4.10 remain steadily sitting at quasi-steady LOL distance and never recedes back toward the injector. Such a tendency may be explained by the observation in Figure 4.5b that the chemical reaction produced by the Yao mechanism initiates rather earlier second-stage ignition, shorter LOL, and weak heat release; thus, the high-temperature reaction may have been already merged into the main lifted flame, and the heat production may be too weak to thermally excite the neighbor gas mixture. This result emphasizes an importance of low-temperature kinetics in choice

of chemical mechanism; thus, the use of Cai mechanism appears to be relevant for combustion recession study.

4.2.3 New Lagrangian Flow Tracking Method

In the previous section, the likelihood of combustion recession with different ramp-down profiles was investigated in a Eulerian coordinate; i.e., CFD RANS modeling. In this approach, however, it is prohibited to track individual fluid element trajectory with lacking further special treatment on a set of CFD data. After CFD simulation is conducted, one can obtain temporal data set of flow properties in Eulerian description with pre-defined time resolution, i.e., CFL time step Δt.

In an effort to better understand the turbulent mixing and reaction history of fluid element after EOI, a new Lagrangian flow tracking method is developed in this thesis. A basic principle behind this technique is to find Lagrangian flow acceleration and velocity at given time set of CFD data and integrate spatial increment over the time difference between sequential data set. The idea begins with Reynolds transport theorem that is to correlate Lagrangian system with Eulerian control volume system. Based on this idea, material derivative of Eulerian velocity field suggests Lagrangian acceleration field assuming two-dimensional space:

$$a_{Lag} = \frac{Du}{Dt} = \frac{\partial u}{\partial t} + u\frac{\partial u}{\partial x} + v\frac{\partial u}{\partial y} \tag{4.1}$$

The first order time derivative term represents local acceleration. The remaining terms indicate convective acceleration, which is driven by spatial change of velocity field. A combination of two different acceleration results in Lagrangian acceleration of fluid element at given location and time. Based on this idea, following assumption is made to allow to calculate the Lagrangian trajectory of fluid elements:

- Fluid element over the time between different temporal data set is assumed to

move with constant acceleration.

- Lagrangian velocity of the fluid element at given time is equivalent to Eulerian velocity at given time and position.

Thus, this simplified assumption enables to calculate the spatial increment by using simple algebraic formulation:

$$x_{new} = x_0 + u_{Lag}dt + \frac{1}{2}a_{Lag}dt^2 \tag{4.2}$$

The Lagrangian flow tracking method is used for post-processing task in this study; i.e., after one case of CFD simulation is done, a set of temporarily resolved Eulerian fluid flow fields is obtained. Therefore, the time increment dt in Equation 4.2 is assumed to be temporal resolution of CFD output data set. Indeed, this approach may also be allowed for run-time processing purpose during CFD time integration step.

4.2.3.1 Lagrangian Fluid Element Tracking for Combustion Recession Analysis

Based on the Lagrangian tracking method described above, pseudo observer particles which are massless for Lagrangian fluid element tracking purpose are assumed to be initially released at injector location and move along the fluid element in time. Several pseudo particles are successively initialized at different time instances; i.e., start of particle release (SOPR); then they travel at velocity u_{Lag}, which is updated equivalent to the local Eulerian fluid velocity $\vec{u}$ at every post-processing time step, dt.

For the present post-processing purpose, five pseudo observer particles are set to be released (initialized) at $x_0 = 1$ mm downstream of injector successively from -0.01 ms to 0.03 ms after SOR at every 0.01 ms interval; thus the time of particle release is now denoted by T_{SOPR} with respect to start of ramp-down. Then each of particles

collects equivalence ratio, temperature, and axial velocity of the fluid element at their instant axial position, x_p with respect to injector location and every time instance as illustrated in Figure 4.11.

In Figure 4.11, the first fluid element trajectory represented by $T_{SOPR} = 0.01$ ms (blue circle symbol) follows the general path that fluid elements would go through during steady combustion period as the corresponding observer particle was initiated before EOI transient; thus, in Figure 4.11a the fluid element gets fuel-richer due to spray evaporation until it reaches some downstream location ($z = 6$ mm), and then gradually fuel-leaner due to ambient air entrainment. Note that the equivalence ratio here is determined from the mixture fraction that considers fuel-originated carbon and hydrogen; thus, its value does not vary by chemical reaction. Due to the turbulent mixing (i.e., momentum exchange) promoted by air entrainment flux, inertia of the fluid element is also found to decrease by distance from the injector as shown in Figure 4.11b. It is interesting to find a little speed-up at LOL distance. This is strongly attributed to the change in local density due to high-temperature reaction; the lower density gets the higher velocity for momentum conservation. Then the fluid element goes into high-temperature reaction zone downstream of LOL in Figure 4.11c.

It is evident that the secondly released observer particle (green square symbol denoted by $T_{SOPR} = 0.0$ ms) goes through different trajectory from the first one. Since the particle was initialized at start of ramp-down, it appears to be affected by the change in air entrainment flux; the EOI transient entrainment tends to make mixture leaner than during the steady injection period as illustrated in Figure 4.11a. It may imply that the mixture element sitting on this observer particle (green symbol) reaches in combustible thermodynamic state more rapidly than the first one (blue symbol). As such, the speed-up due to the high-temperature reaction is found about 2 mm more upstream in Figure 4.11b. Nevertheless, the fluid velocity is still high enough to push the combustible mixture into the lifted-flame reaction zone downstream of

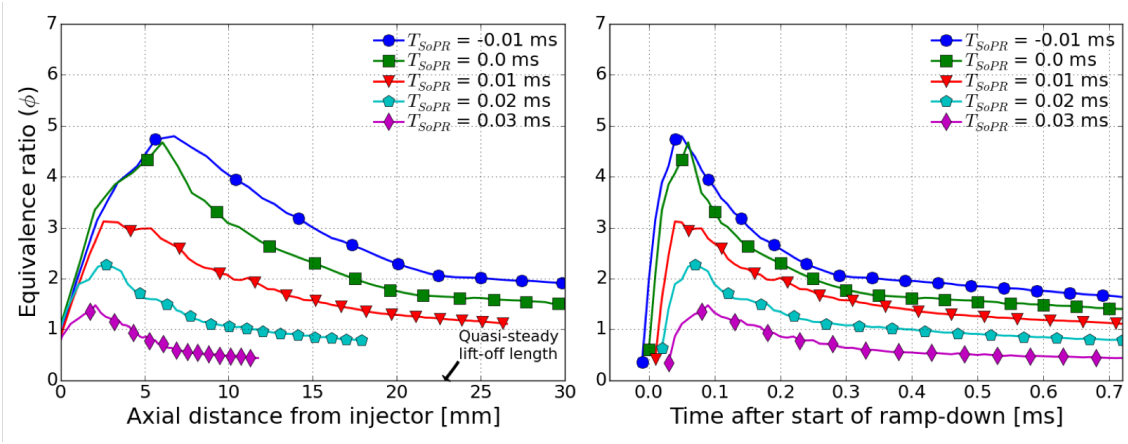

(a) *Equivalence ratio ϕ [-]*

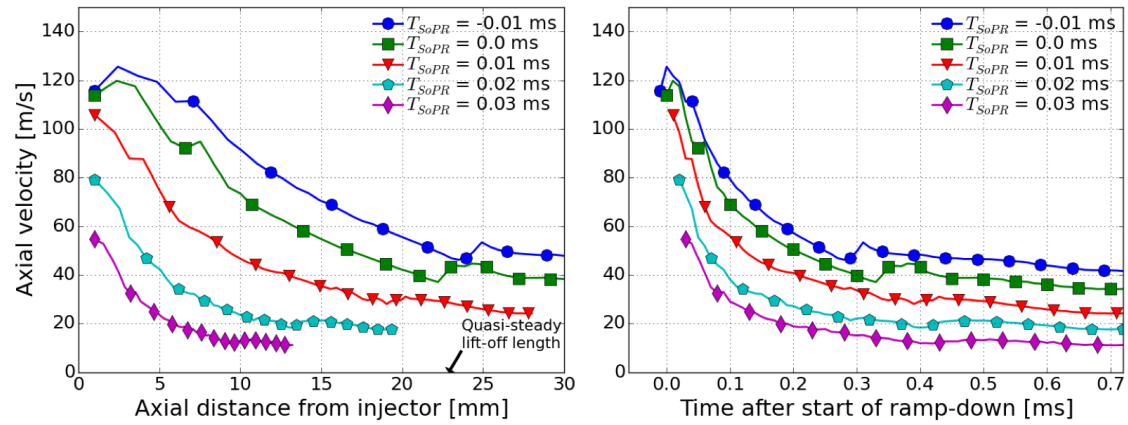

(b) *Axial velocity [m/s]*

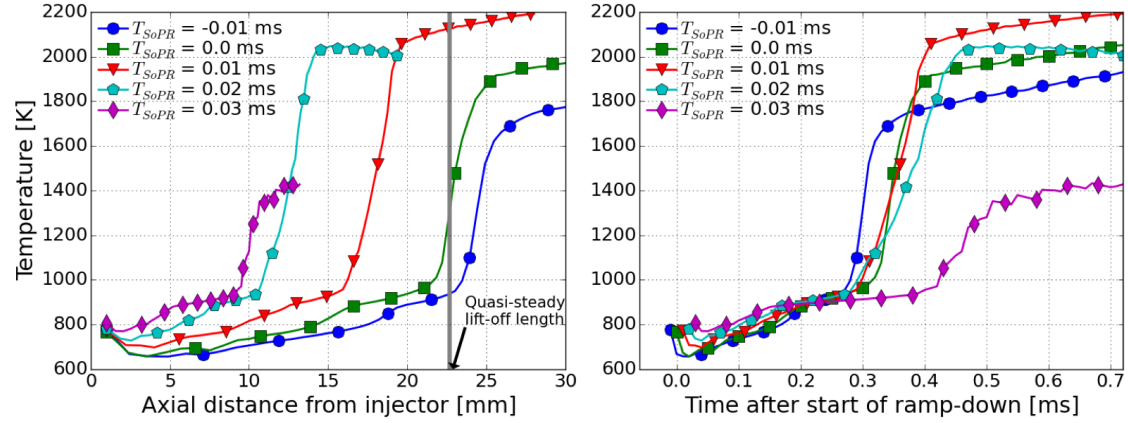

(c) *Temperature [K]*

Figure 4.11: *Spatial (left) and temporal (right) trajectory of fluid elements tracked by Lagrangian flow tracking method: Pseudo observer particles are released at different time -0.01 ms through 0.03 ms after start of ramp-down. A single simulation using Cai mechanism conditioned at ECN Spray A with T_{amb} = 900 K was post-processed.*

LOL. However, noticeable flame shifting towards the injector starts to be observed by the remainder observer particles; $T_{SOPR} = 0.01$ ms ~ 0.03 ms.

The fuel-leaning effect becomes more obvious for fluid elements that originate during the EOI period. The mixture represented by purple color symbol ($T_{SOPR} = 0.03$ ms) rapidly goes to the combustible mixture in stoichiometric state maintaining much lower velocity. Due to the slow convective velocity, the flow residence time becomes relatively long and ignition time delay gets shorter as it stays within highly ignitable mixture state; hence Da number should remain high. Therefore, the mixture begins to chemically react immediately after it is injected, and undergoes high-temperature kinetics from 10 mm downstream as illustrated in Figure 4.11c.

4.3 Implications of Preliminary Combustion Recession Study

In this chapter, a preliminary investigation on the combustion recession in consideration of chemistry and mixing has been performed using OpenFOAM CFD code (v2.4.0). Prior to the reacting ECN Spray A test, predictions of non-reacting spray were performed to assess ability of the open-source OpenFOAM CFD to ensure agreement in experimentally observable mixture formation and spray-gas interaction phenomena. For taking turbulence-chemistry interaction (TCI) and finite-rate chemistry into account, partially-stirred reactor (PaSR) combustion model was used in couple with two different chemical mechanisms; Cai mechanism [153] and Yao mechanism [154]. For detail analysis, a new Lagrangian flow tracking method is developed in this thesis. The methodology allows to track fluid elements spatiotemporally such that it helps to gain further insights about the process of combustion recession dynamics in terms of mixing and chemical reaction. Important implications from the investigation can be summarized as shown below:

- Some degree of inaccuracy was observed in the non-reacting Spray A simulation.

Noticeable deviation was found during the initial unsteady period of injection; this implies that momentum exchange process modeled by the OpenFOAM code (V2.4.0) may have not been well representative of realistic turbulent mixing process. Therefore, the original source package for Lagrangian models in OpenFOAM needs to be redefined to accomodate relevant physics governing transient spray development. This motivates further Lagrangian model improvement and modification in GTFOAM code development for accurate spray modeling.

- Although two chemical mechanisms used in this study captured spray flame ignition delay and flame lift-off length within moderate level of accuracy, Cai mechanism was only able to properly capture the combustion recession behavior as consistently as the recent experiment. Therefore, the use of Cai mechanism is the relatively right choice for tracking finite rate of chemistry and low-temperature kinetics.

- It is important to understand that the RANS modeling is to capture statistical degree of likelihood of finding certain level of scalar (e.g., OH signal in high-temperature reaction zone), whereas the experimentally detected OH signal presents instantaneous occurrence the line-of-sight combusting flame.

- Despite acceptable agreement to some extent by the use of Cai mechanism, the CFD model setup in this preliminary study may not properly accommodate the feature of sub-grid scale autoignition flame pockets which were observed in OH* chemiluminescence. Thus, sub-grid scale mixing and combustion process needs to be properly modeled. To this end, better TCI modeling as well as moderately resolved grid spacing in the region of interest need necessarily to be justified.

- The likelihood of combustion recession can be assessed by the analysis of well-defined Da number which represents the competition between chemical time

scale and flow residence time. This relationship between mixing and chemistry ultimately whether or not the mixture can undergo the second stage (high-temperature) ignition before it reaches main lifted-flame sitting at flame lift-off length (LOL). However, it should also be stated that this simple linearized specification of the Da number is just for the purposed of qualification of scaling impact between mixing and chemistry.

- This study newly proposes a method of Lagrangian fluid element tracking method based upon Reynolds transport theorem. This is helpful to understand spatiotemporal behavior of reacting fluid elements especially for spray flame stabilization and combustion recession studies. This method of algorithm can be utilized for either post-processing time or run-time analysis of reactive scalars of interest.

CHAPTER 5

FLAMELET MODELING IN END-OF-INJECTION (EOI) TRANSIENT COMBUSTION DYNAMICS

This chapter investigates the role of turbulence-chemistry interaction (TCI) in simulation of diesel spray combustion dynamics after end-of-injection (EOI), using the commercially-available CFD code, CONVERGE [83]. In addition, a newly developed C++ open-source library of CFD sub-models, namely GTFOAM, has been used for further examinations in EOI rate shaping effect on combustion recession. The GTFOAM code library, which is recently developed by author for the present TCI modeling purpose, provides essential features of redefined spray and combustion sub-models, and its predictive capability has been validated against the CONVERGE CFD code.

This study was motivated by the preliminary combustion recession study (see section 4) and recent experimental observation on this phenomenon. Accordingly, it is noted that the combustion recession occurs in the near-nozzle region, where characteristic fuel jet scales are on the order of injector nozzle diameter, typical engine CFD simulations with relatively large grid scales may not accurately capture sub-grid scale turbulent mixing and mixing-chemistry interactions in this phenomenon. Thus, in this study, CFD simulations of combustion recession coupled with mixing problem in diesel spray flames are executed to explore this topic. The representative interactive flamelets (RIF) model with a multiple flamelets approach is employed to account for the non-uniformity of reactive scalars at the sub-grid scale. The results are compared with a laminar chemistry (non-TCI) based combustion model; i.e., well-stirred reactor (WSR) model.

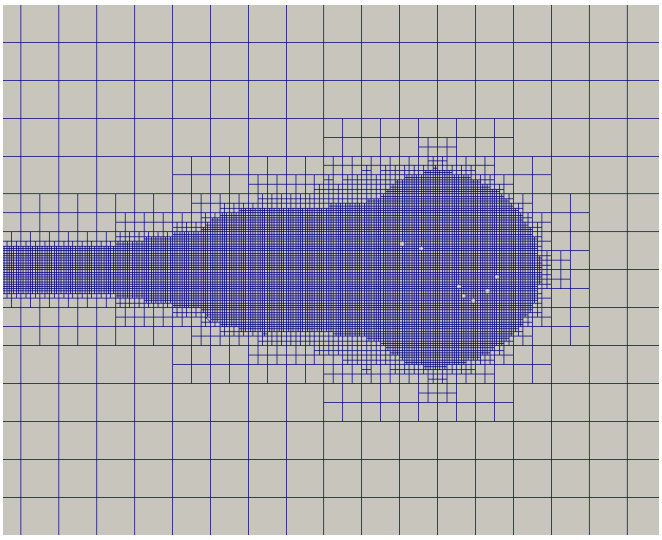

Figure 5.1: *Computational grid setup with adaptive mesh refinement (AMR) for CONVERGE simulations: Consistent grid setup was used for GTFOAM simulations.*

5.1 CFD Model Setup and Code Validation

Several three-dimensional RANS simulations have been conducted under the ECN Spray A condition listed in Table 4.1 using CONVERGE and GTFOAM as consistent setup as they allow. The Spray A condition replicates spray injection and in-cylinder ambient conditions encountered in diesel engine operation. The spray is injected into a quiescent gas within a cubic-volume test chamber ($10 \times 10 \times 10$ cm^3) and freely evolves in the chamber. The injector orifice boundary condition for the spray simulation utilizes the nominal Spray A injection profile provided by the ECN as already illustrated in Figure 4.1. Important analysis regarding unsteady combustion recession are presented with respect to the EOI transient.

Both CFD codes in consideration are capable of constructing a finite volume mesh structure with static and dynamic mesh refinements in regions where small-scale flow structure dominates turbulent mixing. This dynamic mesh refinement technique is generally called adaptive mesh refinement (AMR), and it allows the base volume of a computational cell to be split into smaller volumes at run time. This technique has been utilized in regions where any of the user-specified thresholds for particle

Table 5.1: *Calibrated model constants of KH-RT breakup model: CONVERGE setup vs. GTFOAM setup*

Variable	**CONVERGE**	**GTFOAM**	**Description**
B_0	0.61		KH primary breakup: size constant
B_1	13	15	KH primary breakup: time constant
C_1	0.188		KH primary breakup: drop forming velocity
C_{RT}	0.1		RT secondary breakup: size constant
C_τ	1.0		RT secondary breakup: time constant

presence, fuel mass fraction (10^{-5}), or OH mass fraction (10^{-6}) are reached. The base grid scale was set to 4 mm and the smallest grid scale allowed via 4 levels of AMR was 0.25 mm. Based on this grid scaling method, the resultant finite volume mesh structure constructed during the steady-state period (fully-developed spray) is shown in Figure 5.1. The selection of smallest grid scale (0.25 mm) was made based on the preliminary grid sensitivity test under chemically frozen n-dodecane spray condition.

The simulations were performed using a set of RANS equations, with further conserved scalar transport as necessary for the flamelet equations. The turbulence transport closure is modeled with a gradient transport assumption and introduction of the turbulent viscosity, which is evaluated by using a standard $k-\epsilon$ model without adjustment of model constants described in section 2.1.1.2. The physics of liquid phase, e.g. liquid particle injection, breakup and evaporation, is treated in a Lagrangian framework, while the continuous gas-phase formulations are constructed in a Eulerian framework. Two-way coupling between the Eulerian and Lagrangian phases is achieved by employing source terms in the RANS formulations. The liquid breakup and evaporation were modeled using the Kelvin-Helmholtz-Rayleigh-Taylor

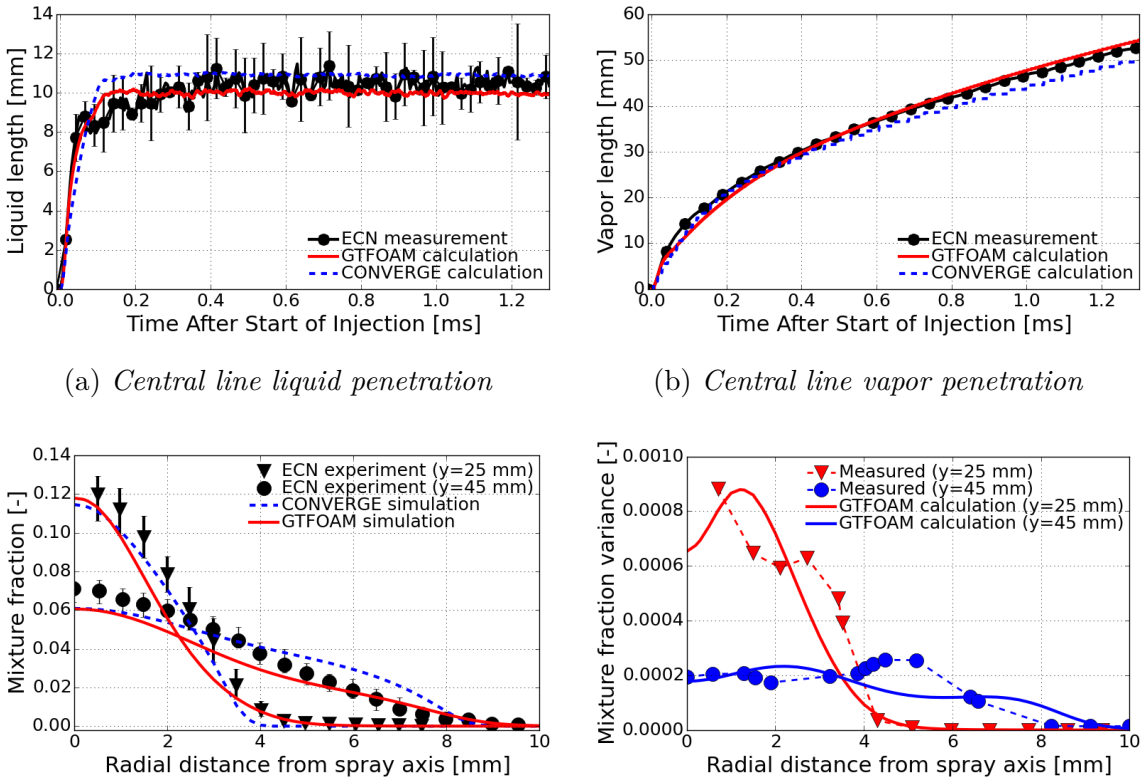

(a) *Central line liquid penetration*

(b) *Central line vapor penetration*

(c) *Radial mixture fraction (fuel mass fraction) distribution*

(d) *Radial mixture fraction variance*

Figure 5.2: *CFD code validations against ECN measurement in terms of calculated liquid length and vapor length: CONVERGE vs. GTFOAM vs. ECN measurement*

(KH-RT) model [76] and Ranz-Marshall's law [131], respectively. Particle interactions, i.e., collision and coalescence, are not considered in this study. The KH-RT model constants were calibrated to give close agreement with experimentally measured liquid and vapor penetrations, and radial mixture fraction distribution at the ECN Spray A standard condition, which will be discussed in the following section. The model constants were then fixed at these optimized values throughout the current study and are listed in Table 5.1.

In general, the use of a Eulerian-Lagrangian technique for diesel spray type simulation often introduces grid-dependent numerical sensitivities, so it is important to validate accurate momentum exchange between the two separate phases. For this reason, predictions of liquid penetration and vapor penetration in the axial and radial

directions are compared against the ECN measurement as illustrated in Figure 5.2; the simulations were performed by using two different CFD codes in consideration. A widely used metric to evaluate the simulated liquid length has been to define the axial extent at which a certain level of accumulated mass (e.g., 97% in this study) is reached in space. Vapor penetration was then quantified at the farthest location downstream where the mixture fraction reached 0.1%, as recommended by the ECN [92].

The close agreement between prediction and experiment during the initial ramp-up period of liquid and vapor penetrations in Figures 5.2a and 5.2b demonstrates that the momentum exchange between liquid particles and gas phase is well captured. Figure 5.2c also shows that the mixture fraction distribution in transverse direction lies close to the range of experimental uncertainty for both CFD codes. In addition, Figure 5.2d presents important meaning of turbulent fluctating quantities (i.e., turbulent intensity) calculated from GTFOAM simulation only; the use of standard $k-\epsilon$ can be assessed by this specific metric. Figure 5.3 presents calculated mixture fraction contour formed by quasi-steady injection and compares the model prediction by the two different codes; CONVERGE vs. GTFOAM. As quantified already in Figure 5.2b, the simulation of GTFOAM exhibits more extended vapor length than that of CONVERGE. Despite such a marginal difference, overall accuracy of the CFD code predictions are assessed to be both acceptable.

It is important to notice that the simulation with GTFOAM code in Figure 5.2 provides greater accuracy compared to the result calculated by unmodified OpenFOAM code (v2.4.0) seen in Figure 4.3. Such an improvement was allowed by enhancement of the numerical time integration regarding the detailed physics relaxation time scaling as described in section 2.1.2.2.

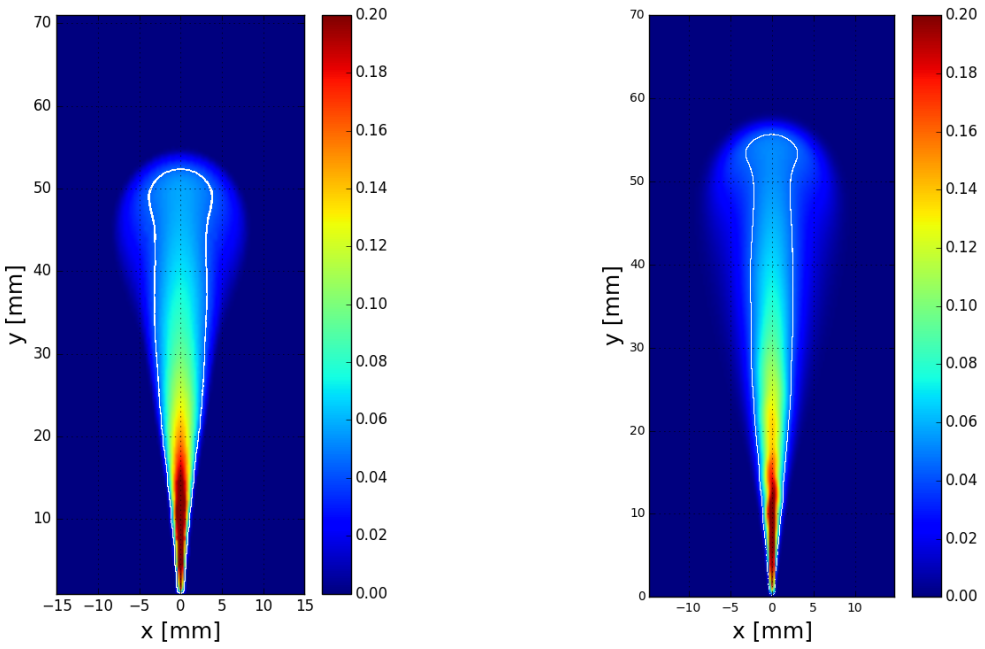

(a) *CONVERGE simulation* (b) *GTFOAM simulation*

Figure 5.3: *Contours of mixture fraction (fuel mass fraction) calculated by two CFD codes: CONVERGE vs. GTFOAM. White solid line indicates stoichiometric mixture. The snapshots were obtained at t = 1.46 ms from start of injection.*

5.2 Results of Turbulence-Chemistry Interaction (TCI) Modeling in Unsteady Diesel Combustion

The main focus of this study lies on exploration of TCI modeling effect on predictions of steady-state and transient turbulent spray flame. In pursuit of this goal, two different combustion models (WSR model vs. RIF model) are presented in comparison. These models are representative of kinetics-controlled combustion and mixing-controlled combustion, respectively. To be specific, the kinetics-controlled combustion model assumes infinitely fast turbulent mixing within grid scale; thus, it accounts for laminar chemistry reaction with no consideration of heterogeneous mixture properties, whereas the mixing-controlled combustion model takes finite rate of turbulent mixing into account for reaction progress. In general, the approach of using WSR model is known to be computationally expensive since it requires to solve stiff ODE

equation for reaction rate source term across entire grid cells. For this reason, to accelerate the solution of detailed chemistry reaction rate source term, the CONVERGE CFD code is incorporated with multizone modeling [158]. In this approach, based on the thermodynamics state of each computational cell, the cells are grouped in zones. In the CONVERGE code, the grouping zone is based on two thermodynamic variables; i.e., temperature and equivalence ratio. Details of this method can be found in CONVERGE CFD code manual [83]. However, the OpenFOAM does not have such a functionality; thus, the WSR simulation with GTFOAM was limited to a few test cases.

It should also be noted that since both modeling approach employs detailed chemistry approach it is important to select relevant chemical kinetics model. As such, the Cai mechanism is only considered for the present TCI modeling study since the previous section 4.2 demonstrated relevance of the use of Cai mechanism [153] over the other choice (Yao mechanism [154]) in better capturing the combustion recession phenomenon. Following sections explore the use of two different combustion modeling approaches in unsteady diesel combustion and provide discussions of the TCI modeling effect in engine combustion modeling as well as combustion recession behavior.

5.2.1 Exploration of Eulerian Particle Flamelet Model (MPFM) Approach: Multi-Flamelets Method

It is important to know that diesel spray combustion is in general characterized by an outcome of finite rate of chemistry along with turbulent mixing process. As a result, the flame is very likely to initiate a certain amount of time after injection begins and settle down at a certain distance from the injector. As such, researchers generally determine ignition delay (ID) and flame lift-off length (LOL) to examine diesel spray flame characterization. Those combustion test metrics are commonly

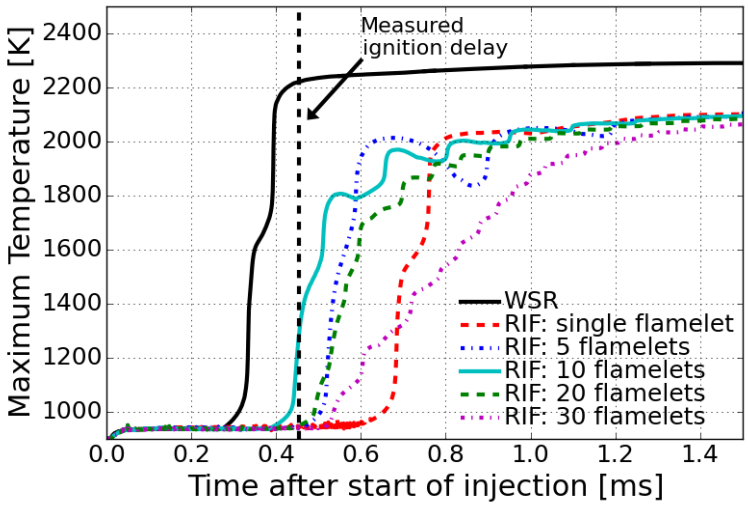

Figure 5.4: *Temporal change of maximum temperature with different flamelet setups: CONVERGE simulation using EPFM approach under ECN Spray A condition,* T_{amb} *= 900 K.*

employed for assessment of modeling accuracy against experimental data. A common way to determine ID is based on temperature rise; i.e., the ECN recommended that ID be measured at the time instance of maximum rate of maximum temperature within the computational domain. The LOL is then defined to be the length from the injector to the axial position of 2% of maximum steady-state Favre averaged OH mass fraction.

Questions may arise when the maximum rate of temperature rise is not straightforwardly defined. Figure 5.4 exemplifies the situations that use of multiple flamelets with RIF model makes a rather gradual increase of maximum temperature. For RIF model with 30 flamelets, the ID may be sensitively determined over a wide range of time (0.5 $\sim$ 1.0 ms), whereas one can find evident peak rate of temperature rise in the case of WSR model and some cases with small number of flamelets.

This limitation motivated researchers in ECN community to find an alternative way for evaluating ID. To this end, the ECN suggested to measure the ID based on OH level in the same way that the LOL is determined; therefore, the ID can be determined as the first time at which Favre-average OH mass fraction reaches 2% of

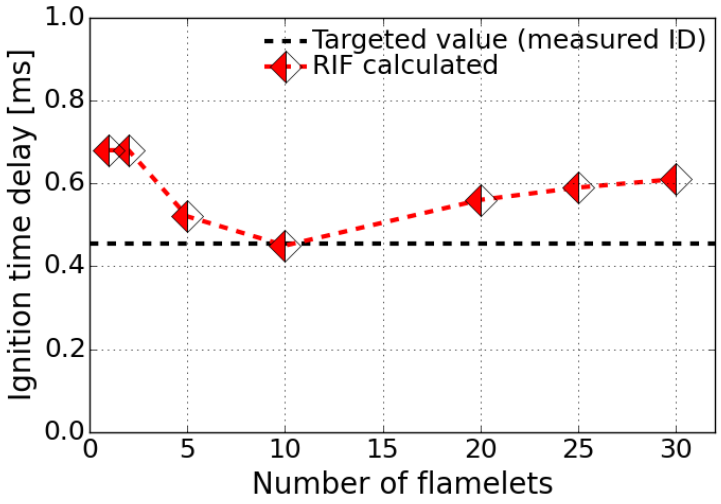

Figure 5.5: *Effects of number of flamelets on ignition delay time based on OH mass fraction trace.: CONVERGE simulation with RIF model setup using EPFM approach under ECN Spray A condition, T_{amb} = 900 K.*

the maximum in the domain after a stable flame is established. Figure 5.5 illustrates the tendency of ignition delay time according to the number of adopted flamelets in the RIF model. Although previously conducted similar study [159] stated that the prediction accuracy would become better as the number of flamelets increases, the best accuracy in the ID was achieved with 10 flamelets and the calculated ID seems to settle at around 0.6 ms as the flamelets number keeps increasing.

In Figures 5.6 that compare WSR model and RIF model approaches, some of the general features of ignition and flame dynamics predicted by the WSR model are also identified by the use of RIF model consistently including low-temperature heat release, transient spray flame development, and evidence of combustion recession. However, a very noticeable oscillatory behavior in the RIF modeling is featured in the LOL and heat release rate (HRR) profiles in comparison to the WSR model. Such oscillations are not typically observed in measurements, so this phenomenon appears to be a numerical artifact stemming from shortcomings of the RIF model. Such an numerical artifact was also pointed out in the previous study [159]. To further look into such an artifact, this section revisits the details of unsteady behavior of

the flamelet solution with various multiple flamelets condition. Figures 5.6a $\sim$ 5.6f sweep different choice of flamelet numbers and the WSR model, and illustrates the temporal change of LOL, flame length (FL) which is the furthest position of reaction zone, and domain integrated HRR. The LOL and FL were evaluated by the OH mass fraction base method. The present simulations have reproduced the previously reported oscillatory behavior in LOL and HRR with the RIF model setup; however, the flame length was very similar over the entire employed cases regardless of number of flamelets used. Therefore, further analysis needs to be made focusing on the region where the lifted flame settles down.

Overall characteristics of diesel spray combustion is observed rather consistently over the various model setup except for single flamelet model setup; i.e., success of capturing lifted diesel spray flame has solely been made by the RIF model with finite number of flamelets and the WSR model. In addition, the combustion recession is also identified by observing shortened LOL during the end-of-injection (EOI) period; i.e., after 1.46 ms. However, the single flamelet setup failed to settle the lifted flame downstream; i.e. once the very initial reaction occurs downstream at around 30 mm, the LOL then rapidly recess back towards the injector. In addition, the single flamelet solution does not exhibit the oscillatory behavior in LOL and HRR variations. The primary reason is that the scalar dissipation rate, χ in Equations 2.48 and 2.49 was determined by domain-averaged value over the entire space that the spray mixture occupies. Therefore, the domain-averaged value of χ may not convey the impact of locally intensive turbulent mixing particularly near the injector location. Consequently, it is very likely that the local quenching due to high scalar dissipation rate was prohibited in the upstream field.

On the other hand, all other solutions from multiple flamelets present the oscillating flame dynamics between the nozzle and the LOL. It is also important to note that the oscillations are observed at consistent frequency of flamelet initiation; e.g.,

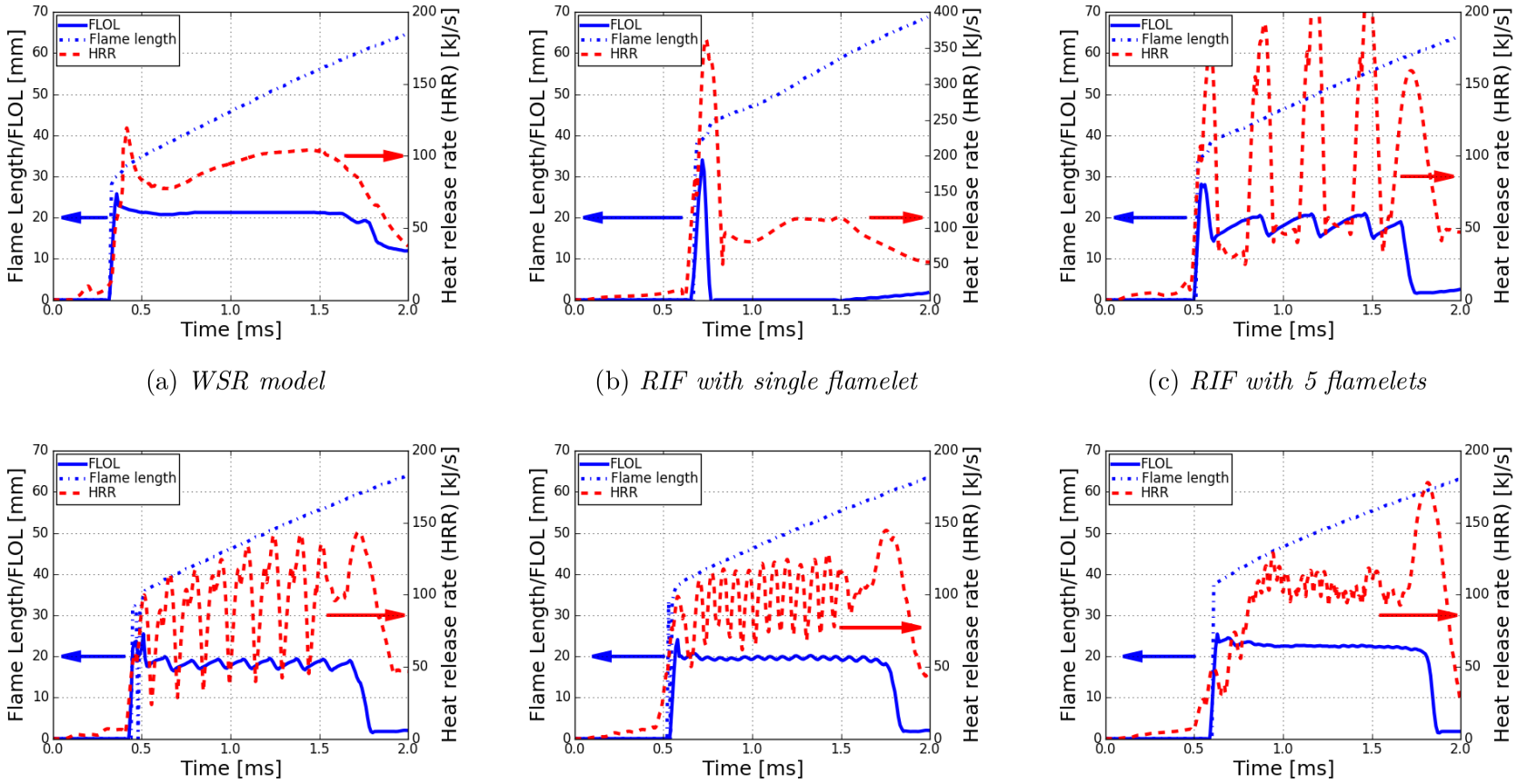

(a) *WSR model* (b) *RIF with single flamelet* (c) *RIF with 5 flamelets*

(d) *RIF with 10 flamelets* (e) *RIF with 20 flamelets* (f) *RIF with 30 flamelets*

Figure 5.6: *Temporal variation of flame lift-off length (LOL), flame length (FL), and domain integrated heat release rate (HRR): Observation of oscillatory behavior in flamelet represented solution. The quantities of FLOL and FL were evaluated at 2% of maximum OH mass fraction.*

there are five peaks of HRR and LOL with 5 flamelets setups shown in Figure 5.6c. Then, the oscillation amplitude is attenuated with further increase of flamelet number. Thus, this gives strong implication that distinct RIF solution from the subsequent flamelet libraries may cause the discontinuous solution of reactive scalars. Despite clear oscillatory behavior, the use of 20 flamelets or more seems to be reasonable. This was also recommended by the recent study [159] on RIF modeling.

Figure 5.7a further illustrates the moment at which the significant oscillatory peak appears as highlighted by yellow arrow on the figure. The sudden change in OH mass fraction also indicates discontinuous combustion process at the moment. This observation can be explained by identifying that the individual RIF solution represented by each of flamelet libraries, $\widetilde{z}_l$ in Equation 2.66, limits the spatial domain where the corresponding flamelet solution covers as illustrated in Figure 5.7b. From the consecutive marker solution contours in Figure 5.7b, it should also be emphasized that different Eulerian marker solutions may overlap together due to turbulent mixing; therefore, each of flamelet solutions is weight-averaged to determine resulting turbulent 'mean' value. Based on this idea, the sudden expansion of spray flame area found at 0.66 ms provides an evidence that the second flamelet solution has finally contributed its ignition phase to the turbulent mean quantity; consequently, yielding rapid increase of OH species production.

Figure 5.7c presents temporal variations of domain-averaged scalar dissipation rate for each of flamelet libraries. Each flamelet is initiated at uniform time intervals out of injection duration and encompasses a certain portion of injected fuel amount and domain occupation indicated by Eulerian marker solution. Based on this observation, the idea that the scalar dissipation rate can be considered as an eigenvalue for unsteady quenching and autoignition seems to hold for the present simulation. Knowing that the ignition delay time (ID) should be captured by the first flamelet solution and was found at 0.45 ms from Figure 5.5, the eigenvalue of χ for flamelet

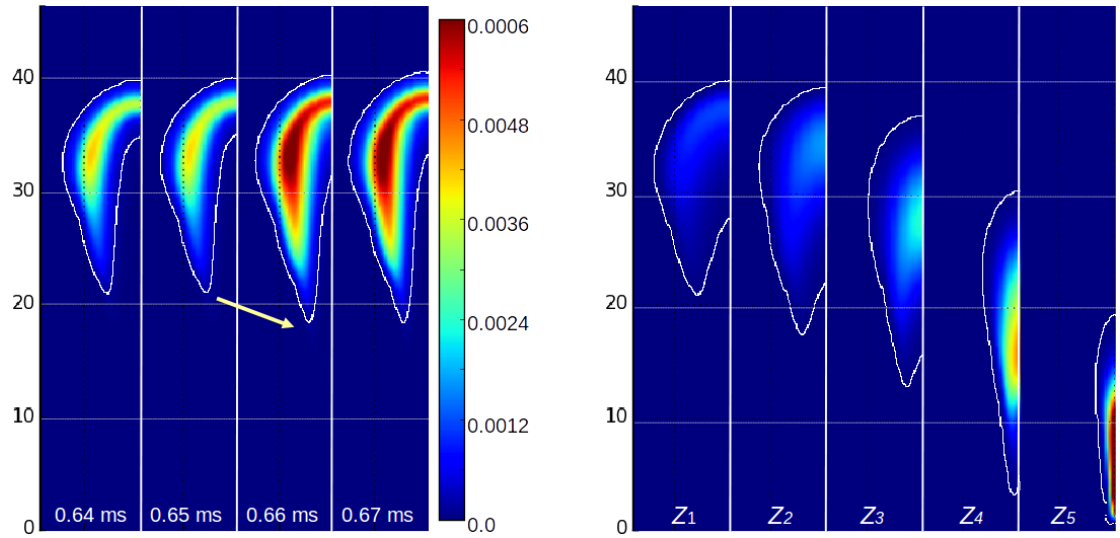

(a) *Time sequence of OH mass fraction observations when oscil- lation appears. Spray flame boundary is marked at 2% of maximum OH mass fraction.*

(b) *Time variations of marker solutions. White solid line indi- cates the spray flame boundary at 2% of stoichiometric mixture fraction.*

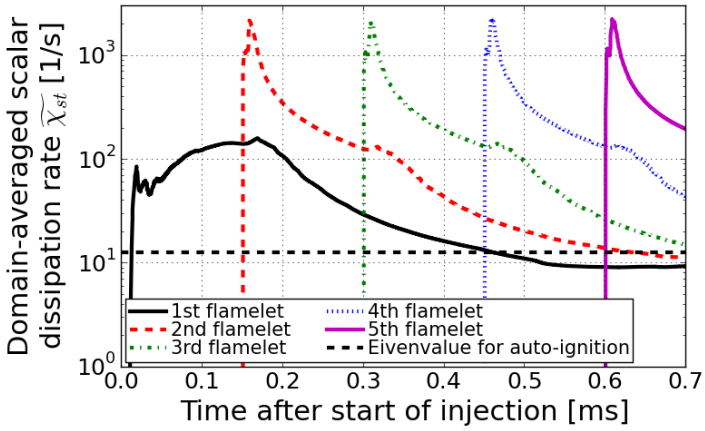

(c) *Time sequence of flamelet initiation and corresponding domain-averaged scalar dissipation rate variations in time. Dashed black line indicates the eigenvalue at 13 for capturing auto-ignition.*

Figure 5.7: *Observation of sudden change in reactive scalar (OH mass fraction) and correlation with Eulerian marker solutions and domain-averaged scalar dissipation rate: CONVERGE simulation at T_{amb} = 900 K using 5 flamelets*

solution to ignite can be evaluated at around 13 as indicated with black dashed line in Figure 5.7c. The concept of the eigenvalue problem for local autoignition is supported by finding that the second flamelet's scalar dissipation rate meets this value at the time instance of 0.65 ms at which the noticeable ignition contribution is found

by second flamelet; i.e., oscillatory peak, in Figure 5.7a.

5.2.2 Assessment of TCI modeling in Diesel Combustion Dynamics

In this section, several important features of approximated turbulent mean scalar fields produced by the TCI modeling approaches in consideration is discussed. One of the important aspects of turbulent combustion physics is its intermittency characteristic. In practical turbulent flows, this is often encountered with unsteady nature of flapping flame brush, which in turn should exhibit rather distributed transverse profile when ensemble-averaged. A more physical insight into these conceptual differences can be achieved by considering a fixed location near the spray flame periphery. A temperature measurement at such a location would yield an intermittent signal due to the turbulent flame fluctuations across the measurement location. Furthermore, there will be a likelihood of measuring the stoichiometric adiabatic flame temperature over a wide spatial region due to these fluctuations. In this regard, the main conceptual difference between WSR model and general TCI models lies in modeling the aforementioned intermittency nature of turbulent combustion. Within the RANS framework, the laminar chemistry (non-TCI) type model (e.g., WSR model in this study) will only predict one stoichiometric adiabatic flame location along the ensemble-averaged stoichiometric contour since the model eliminates sub-grid scale heterogeneous mixture and accordingly neglects non-linear chemical reaction source terms. Therefore, the key principle of the TCI modeling is to approximate turbulent "mean" flame profile rather than capturing instantaneous laminar profile especially in RANS framework.

5.2.2.1 Spray Flame Structure Analysis: WSR model vs. RIF model

Figures 5.8a and 5.8b illustrate quasi-steady lifted flame captured at $t_{SOI} = 1.46$ ms (equivalent to $t_{ASOR} = 0.0$ ms), where the EOI transient is about to begin shortly

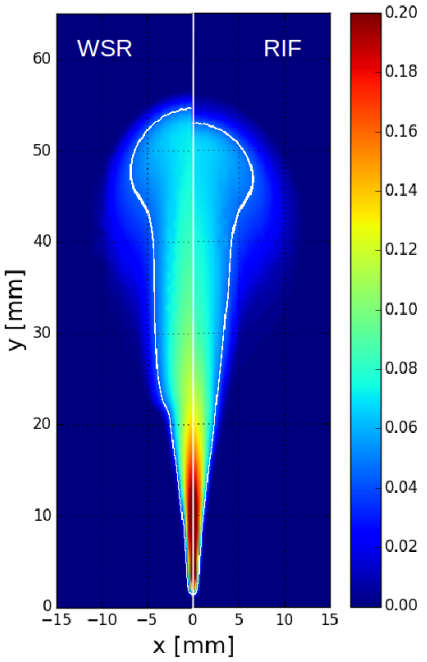

(a) *Mixture fraction z*

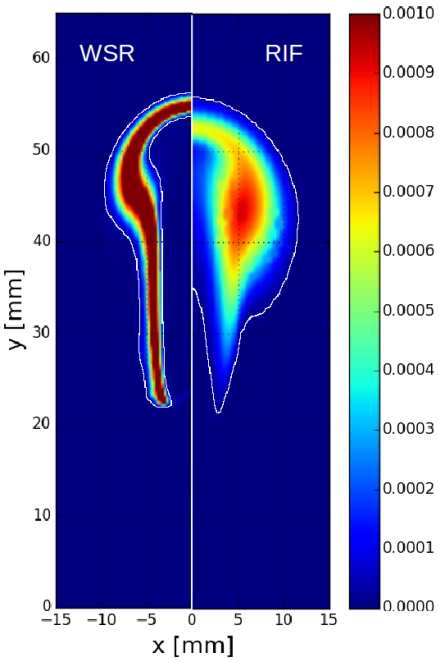

(b) *OH mass fraction*

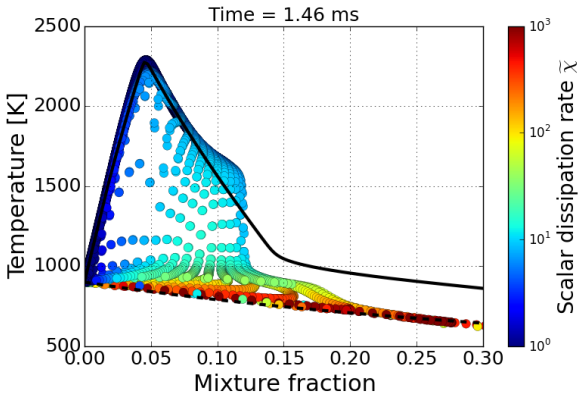

(c) *Flame structure by WSR model*

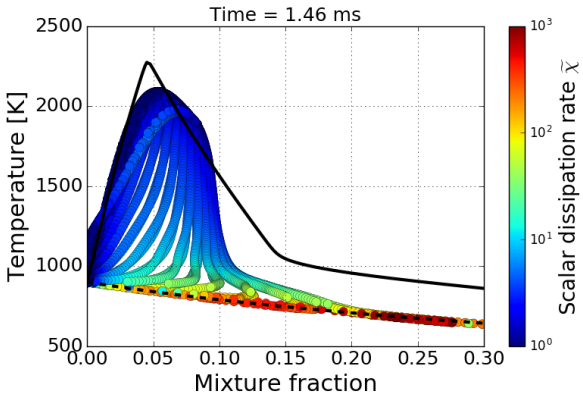

(d) *Flame structure by RIF model*

Figure 5.8: *CONVERGE simulations: Quasi steady spray flame at t = 1.46ms and flame structure; (a, b) White solid line in Z contour: iso-stoichiometric mixture, White solid line in OH contour: OH level at 2% of maximum steady-state concentration. (c, d) Flame structure with respect to mixture fraction: black solid line indicates equilibrium thermochemical state as only a function of mixture fraction. 20 flamelets for RIF model was adopted as suggested for Spray A by Kundu et al. [159]*

after this time instance. One can see different OH profiles across the spray flame periphery, whereas the mixture fraction field looks rather qualitatively similar. It is important to note that the RANS resolved OH mass fraction field with RIF model

reveals substantially thick profile of numerical solution, whereas the WSR model estimates non-zero level of reaction in the vicinity of stoichiometric mixture with much narrower span. Also, the approximated OH field with RIF model seemingly shows lower peak of OH level across the stoichiometric line. This implies that the introduction of PDF in RIF model gives rise to a broader mean reacting scalar profile, and consequently a more dissipative solution. Such a rather distributed flame profile by the RIF model support the idea of intermittency captured by the TCI modeling, because highly unsteady turbulent feature of spray flame may intermittently sweep over a broad range of physical space such that its ensemble-averaged quantity no longer exhibits sharp change in reaction zone.

Figures 5.8c and 5.8d shows instantaneous flame structure in terms of mixture temperature with respect to mixture fraction z. The stoichiometric mixture is formed at $z = 0.04509$ for this ECN Spray A condition ($T_{amb} = 900$ K, and 15% oxygen level). The upper black solid line in the figures follows the variation of equilibrium temperature of the mixture as a function of mixture fraction; this means that the equilibrium temperature was obtained by the assumption of zero-dimensional (path-independent) adiabatic, constant volume batch reactor (i.e., homogeneous mixture combustor). The lower black dashed line indicates pure-mixing problem which is prior to ignition. Thus, points in the figures may individually represent instantaneous progress variable with respect to equilibrium state. It should be noted that the plots identify overly heated mixture beyond the equilibrium level; it is due to the feature of path-dependent mixing and chemical reaction processes of spray flame in physical space, whereas the batch reactor assumption only considers mixture fraction variable space.

A noticeable difference found in the flame structures between WSR model and RIF model is clear by looking at some intermediate level of progress variable (here, temperature level between pure-mixing and equilibrium). Points in the Figure 5.8c

tend to sit along or in the vicinity of mixing line (dashed) and equilibrium line (solid), while the Figure 5.8d identifies significant density of intermediate progress variable level. Such a tendency in the WSR model case is attributed to the nature of fast chemistry with no consideration of finite rate of mixing; as such, once a mixture element starts to chemically react, it may promptly jump to equilibrium level due to fast chemistry. However, for the RIF model, the use of presumed PDF integration may generate diffusive solution points as shown in Figure 5.8d. Another difference between two models is also obvious at stoichiometric mixture temperature. The WSR model predicts adiabatic equilibrium flame temperature around 2,300 K in Figure 5.8c; thus, this is an evidence of no consideration of turbulent mixing in chemical reaction. In other words, the calculation of reaction source term is representative of adiabatic constant volume batch reactor model without mixing effect. On the other hand, the RIF model produces lowered peak temperature at this stoichiometric condition since it combines the effect of local scalar dissipation rate and turbulent intermittency replicated by the presumed PDF integration method.

To further investigate the effect of presumed PDF integration on predicted flame structure, GTFOAM code was utilized since it offers an option to freely turn on/off PDF integration method by its opensource software platform, whereas it is not allowed for CONVERGE simulations. Figures 5.9a and 5.9b shows calculated flame brush in terms of OH concentration as an indication of high-temperature reaction zone with an option of β-PDF integration turned on and off. Thus, the latter case will yield mean flame brush produced by bypassing moment of *pdf* when estimating mean reactive scalars in Equation 2.58. One can notice that bypassed PDF integration method in Figure 5.9b estimated very high concentration and stiff gradient of OH quantity across spray flame. Therefore, it can be stated that the PDF integration plays an essential role in generating turbulent "mean" flame brush in ensemble-averaged solution field. In addition, knowing that the higher OH concentration indicates more heat release;

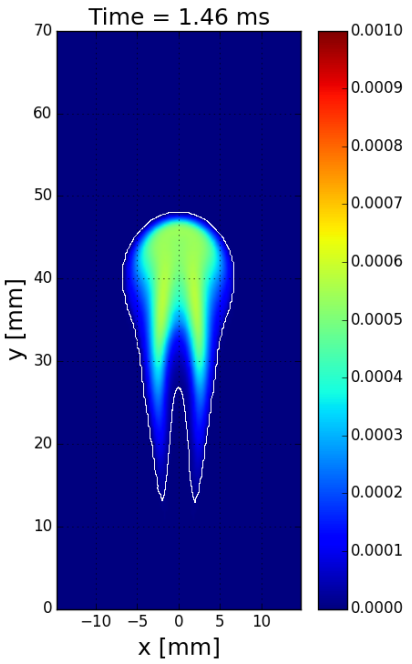

(a) *OH mass fraction with presumed PDF*

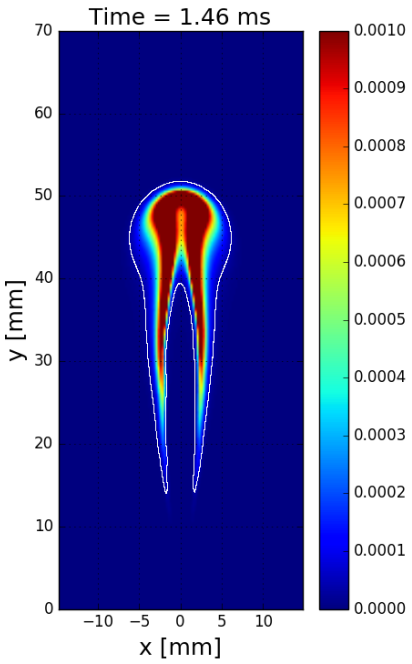

(b) *OH mass fraction without presumed PDF*

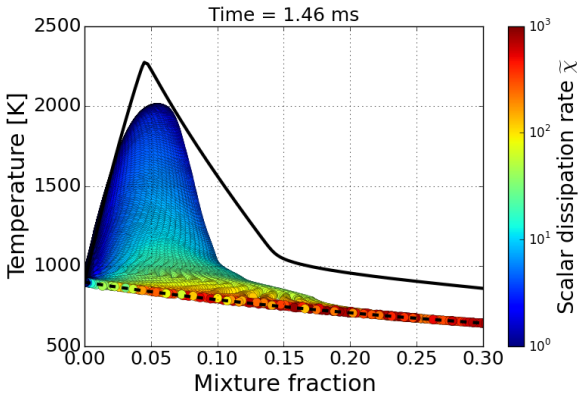

(c) *Flame structure with presumed PDF*

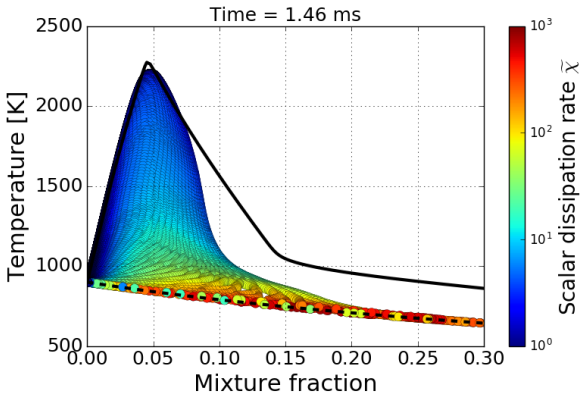

(d) *Flame structure without presumed PDF*

Figure 5.9: *GTFOAM simulations with effect of presumed β-PDF integration: test condition and detailed analysis on this result are same as CONVERGE simulations in Figure 5.8*

thus case with bypassed PDF integration results in more intense thermal expansion leading to extended flame length along the spray axis as illustrated in Figure 5.9b.

Figures 5.9c and 5.9d also display calculated flame structures by setup of GT-FOAM code and RIF model with and without presumed PDF integration. The comparison between these two scatter plots exhibits an outcome of PDF integration

in estimating turbulent mean scalars; i.e., the presumed PDF method results in lowering peak temperature by 200 K approximately under the employed ECN Spray A condition (T_{amb} = 900 K). In addition, one thing to note in Figure 5.9d is that peak temperature is still below the adiabatic equilibrium flame temperature at stoichiometric condition; this implies that the use of RIF model still applies impact of scalar dissipation rate on the flame structure as illustrated in Figure 1.6a.

Lastly, GTFOAM-RIF model setup in Figure 5.9c in comparison to CONVERGE-RIF model setup reveals a code-to-code variation in calculated flame structure. The solution of GTFOAM-RIF model setup predicts flame structure within equilibrium limit. This deviation is originated from the intrinsic difference in RIF model implementation in different CFD codes. As explained in previous section 2.2.2.2, the solution of temperature field in CFD physical space is determined by different method for these two CFD codes; i.e., GTFOAM directly applies primitive variable method to enthalpy solution in three-dimensional CFD solution (physical space) without transporting energy quantities in physical space, whereas the CONVERGE code with RIF model setup is to solve energy balance equation in both physical space and reaction space. Therefore, GTFOAM produces rather physical-path independent solution because it relies directly on the solution of one-dimensional flamelet equation, that is only a function of mixture fraction and it proceeds towards equilibrium state in principle.

5.2.2.2 Evaluation of General Diesel Combustion Test Metrics

Figure 5.10 presents ECN Spray A diesel combustion ignition delay (ID) time and flame lift-off length (LOL) reproduced by combined use of two CFD codes and two combustion models in considerations. For the GTFOAM simulations, as aforementioned in the previous section, using WSR model is limited to some extent since it requires to evaluate stiff ODE calculations for entire cells whereas the CONVERGE

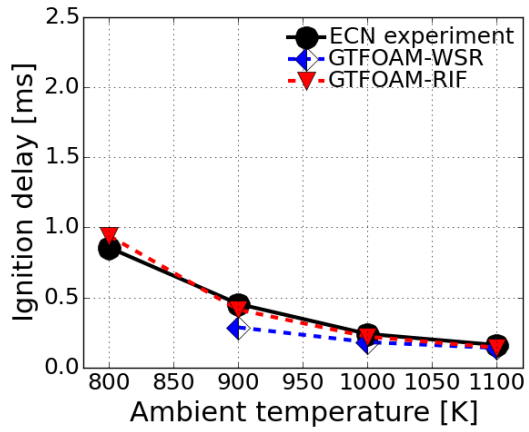

(a) *Ignition delay: GTFOAM*

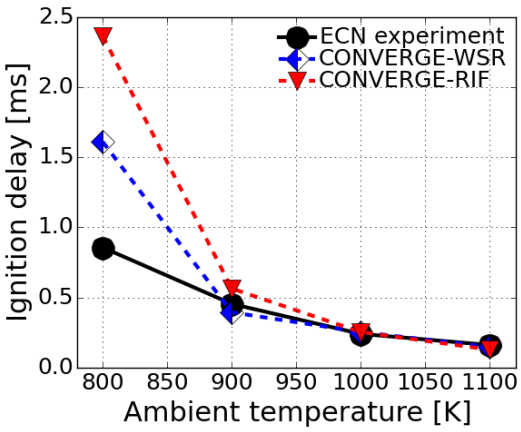

(b) *Ignition delay: CONVERGE*

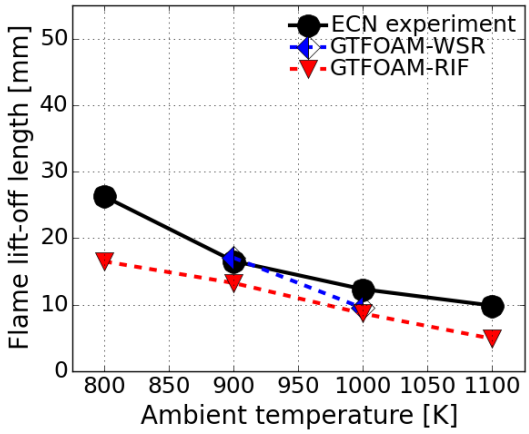

(c) *Flame lift-off length: GTFOAM*

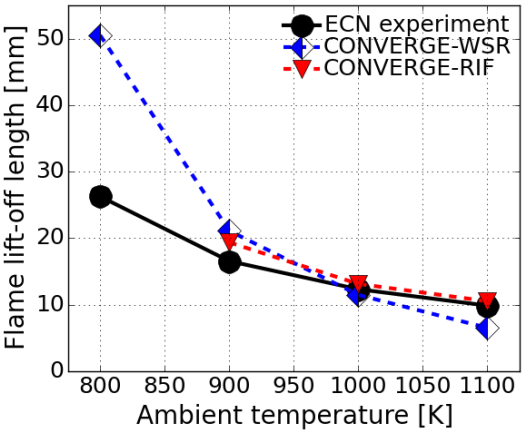

(d) *Flame lift-off length: CONVERGE*

Figure 5.10: *Comparison of WSR model and RIF model in assessment of diesel combustion ignition delay (ID) time and flame lift-off length (LOL). GTFOAM simulations are also presented to be assessed against the CONVERGE simulations.*

provides powerful tool to reduce such an expensive effort by using multizone modeling [158]. Using this multizone modeling for detailed chemistry WSR model, the computational time was comparable to the case of RIF model used in CONVERGE simulation. Since the stiffness in ODE calculation may noticeably arise when ignition initiates, the use of WSR model without multizone modeling may be viable to assess predictions of ID and LOL at relatively high ambient temperature conditions. This is because time required to settle the flame down at steady state is relatively small as the ambient temperature increases; i.e., fast chemistry governs the physics. For this

reason, simulations with GTFOAM at low ambient temperature (e.g., T_{amb} = 800 K) was computationally prohibitive.

In general, predictions of ignition delay are found to be rather consistent at high ambient temperature conditions (T_{amb} = 1,000 and 1,100 K) irrespective of choice of combustion models. Under such chemically reactive conditions (high temperature), chemical reaction proceeds relatively fast so that transition from low-temperature kinetics to high-temperature kinetics is rapid; consequently, impact of turbulent mixing on onset of ignition may be unnoticeable. However, deviation between the models become clear as the ambient temperature decreases; i.e., second-stage combustion (high-temperature kinetics) with WSR model tends to arise more rapidly than the case of RIF model in use. This tendency may be attributed to the significant impact of turbulent mixing incorporated in scalar dissipation rate χ in the RIF model. As previously explained, increased turbulent mixing intensity (high χ) around the spray jet may partly prevent the mixture from reacting with ambient air to some extent due to heat loss to ambient gas. Thus, it may delay the high temperature ignition process. However, this effect of turbulent mixing intensity is not taken into account for the WSR model. This tendency is observed consistently across the use of different CFD codes.

On the other hand, it is noteworthy that several earlier studies [160, 161] reported opposite trend to this observation particularly under low-temperature combustion (LTC) targeted conditions, e.g., T_{amb} = 800 K. According to their results, RIF model predicts lower ignition delay than WSR model due to some degree of turbulent diffusion effect in intermediate reaction step. To be specific, diffusion of some intermediate species during low-temperature kinetics were observed to accelerate the high-temperature kinetics. This was also evidenced by other studies of LES [161] and DNS [50, 162]. For detailed analysis on this effect, Dahms and co-workers [162] explained the evidence of *cool flame wave propagation*; a localized low-temperature

ignition kernel makes neighbor mixture chemically excited promoting rapid high-temperature kinetics. The recent studies [160, 161] using RIF model revealed that this cool flame wave effect was observed to be realized within flamelet model framework rather than using WSR model approach. However, this effect is not evident in the present simulation results. Therefore, further examinations under LTC targeted conditions in regard to modeling and chemical mechanism is needed for a follow-up study.

5.2.3 Effect of TCI modeling on Predictions of Combustion Recession

This section focuses on the predicted end-of-injection (EOI) combustion transient. The predicted and measured time sequence of combustion recession after start of ramp-down (ASOR) is presented in Figures 5.11a and 5.11b at ambient temperatures 900 K and 1,000 K, respectively. The left column of snapshots shows instantaneous images of OH chemiluminescence from ECN experiments [92] followed by the OH concentration from the RANS simulations with the WSR model and the RIF model. The GTFOAM simulation was conducted under T_{amb} = 900 K only. It is important to know that the experimental measurements are line-of-sight images, while the computational predictions are shown as cut-planes along the spray axis for simplicity of post-processing. Because the combustion recession is generally found in the near-nozzle location, where the jet thickness is narrow (less then 1 mm), it can be believed that observations of predicted combustion behavior at the spray centerline should nearly replicate line-of-sight observations.

It is noteworthy that prior experiments [61] have identified distinctive combustion recession regimes at different ambient thermodynamic conditions, including no combustion recession, weak or partial combustion recession, or strong sequential reactions retreat. Under this notion, Figure 5.11a shows an example of weak or partial combustion recession, where isolated pockets of ignition are observed upstream of the LOL,

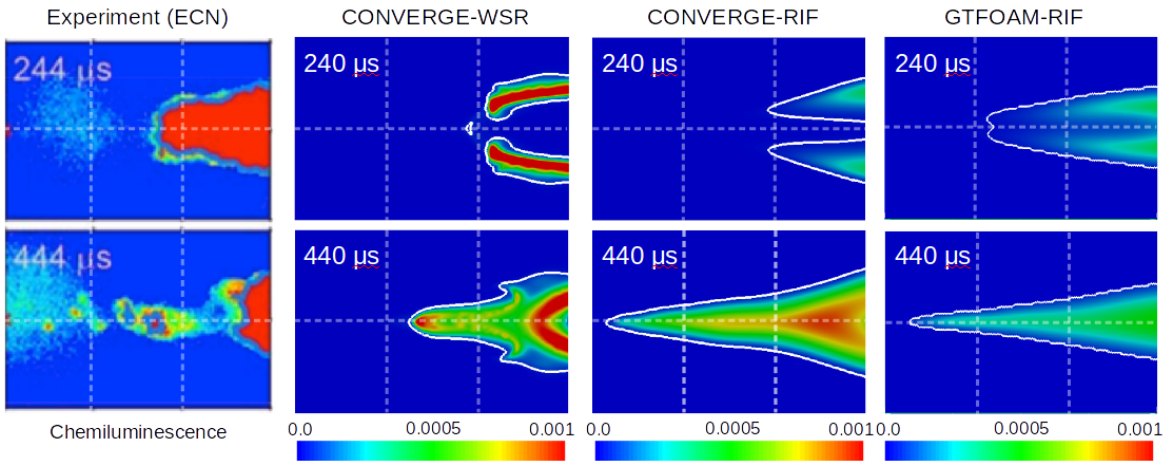

(a) T_{amb} = *900 K*

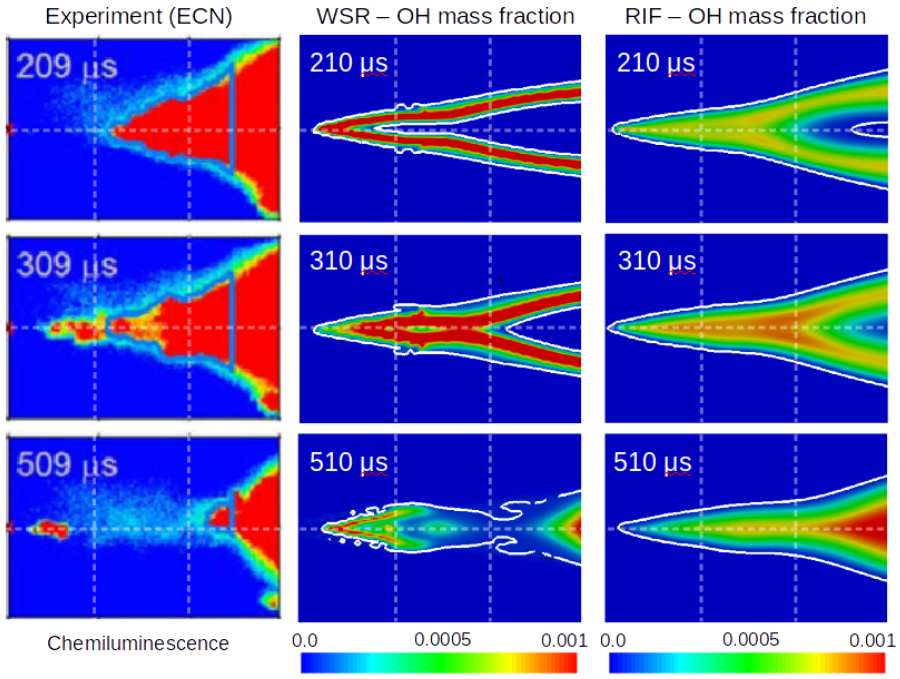

(b) T_{amb} = *1,000 K*

Figure 5.11: *OH* chemiluminiscence and calculated OH concentration for combustion recession at different ambient temperature conditions: Instantaneous snapshots from ECN experiment (left first column) and ensemble-averaged quantities from RANS computations (next two or three columns) with spray flame boundary limit detected by OH concentration at 2% of ground-state maximum OH level in steady state, GTFOAM simulation for combustion recession was conducted under only* T_{amb} = *900 K.*

but a connected high-temperature ignition sequence or flame front is never observed.

Figure 5.11b displays an example of strong sequential reactions back towards the in-

jector nozzle, where high-temperature ignition regions appear to propagate upstream from the LOL and nearly fill the entire jet between the nozzle and LOL. Following discussions focus on modeling these two regimes.

At the condition of T_{amb} = 900 K, the experiment shows very clear indications of separated small-scale regions of high OH (indicated by small red spots) upstream of the LOL. It is evident that these pockets spontaneously evolve, indicating an auto-ignition process. Because the experimental snapshots are instantaneous images, quantitatively complete comparisons to the experiment are not possible to achieve with RANS modeling. Instead, the current RANS data only demonstrates the likelihood of combustion recession. In this context, although the WSR model predicts the occurrence of combustion recession, it does not extend very far upstream where high OH regions are observed in the experiment. One possible reason that the WSR model fails to predict these upstream reaction kernels is because these reactions may be generated at a scale much smaller than the grid size (0.25 mm). The first order moment method employed in the WSR model approach cannot accommodate the heterogeneous mixing and reaction in sub-grid scales. On the other hand, the RIF model predicts a much more elongated combustion recession zone, covering up to the near nozzle location, which is more consistent with the experiment. This implies that the RIF model with the presumed PDF may better represent the effect of sub-grid scale reactions on the reactive scalar mean quantities.

At the condition of T_{amb} = 1,000 K, the chemiluminescence identified a "sequential ignition" regime of combustion recession. As the name implies, the ignition kernels are successively generated from the position where the flame was stabilized (i.e., the LOL) back towards the injector shortly after EOI. In this context, the WSR model predicts a more rapid transition to sequential ignition at 210 μs ASOR, compared to the experiment at 209 μs, because the combustion recession zone has already been fully developed. Then, the reactivity decays later in time by 310 μs ASOR, showing

lower OH concentration at the upstream tip than before, whereas the experiment shows the maximum growth of combustion recession at 309 μs. At 510 μs ASOR, the WSR model predicts a separated reaction pocket near the injector, which looks consistent with the experiment at 509 μs ASOR. The success in capturing the local flame dynamics of combustion recession with the WSR model at this condition might be explained by the decreased chemical time scale (rapid reaction rate) at such a highly reactive ambient thermodynamic condition. Therefore, it can be believed that the role of chemistry can be expected to become more dominant than turbulent mixing at a higher temperature condition.

The RIF model also appears to moderately predict the sequence of combustion recession growth followed by decay of chemical reactivity at 1000 K, as seen in the right column of Figure 5.11b. However, it also tends to overestimate the likelihood of combustion recession near the nozzle at 210 μs ASOR. At 310 μs ASOR, the RIF model shows a very good match qualitatively with the experiment. On the other hand, the introduction of the PDF statistics in the model dissipates the numerical solution, preventing separated flame kernels from appearing.

5.2.4 Effect of End-of-Injection (EOI) rate profile on Combustion Recession

The injection profile modeled in the previous sections was based on a single-hole axially-drilled injector that exhibits relatively fast ramp-down end-of-injection (EOI) transient (40 μs), but practical multi-orifice injectors may exhibit slower transients or hole-to-hole variation in EOI profile. As the previous chapter 4 demonstrated the correlation of combustion recession and EOI transient induced mixture leaning process, further examinations on EOI rate shaping change in consideration of combustion recession occurrence will give more insights on the dominating physics. Taking the standard ECN Spray A injection profile into consideration as a baseline case, two

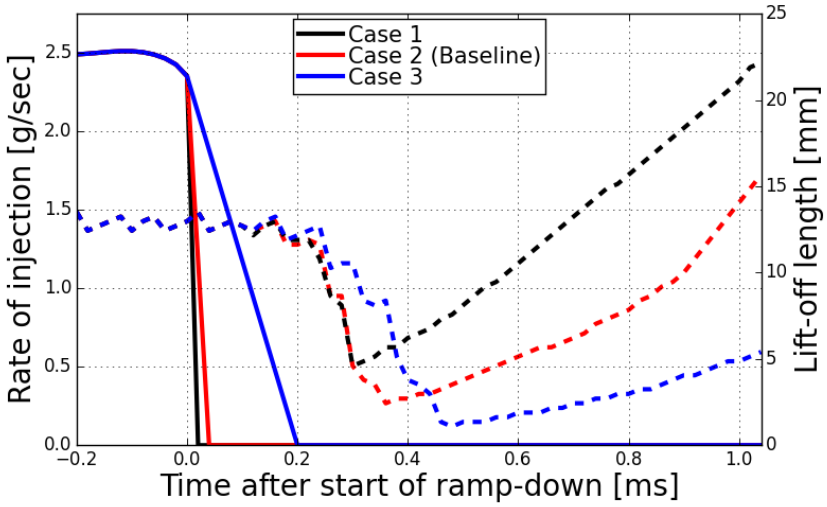

Figure 5.12: *Effect of end-of-injection (EOI) transients on combustion recession behavior. Solid and dashed lines illustrates temporal change in rate of injection (ROI) and flame lift-off length (FLOL), respecitively. Case 1: fast ramp-down EOI shaping, Case 2: standard ECN Spray A, Case 3: slow ramp-down EOI shaping*

more rate shaping modifications were applied to the end period of rate of injection (ROI) profile varying EOI duration from 20 μs (case 1) to 200 μs (case 3) as shown Figure 5.12.

In this test, the simulations were performed using the GTFOAM code setup with RIF model (20 flamelets) and Cai mechanism [153], as this model setup was able to provide reasonable predictions of combustion recession in the preceding section. Also, since the ROI profile prior to start of ramp-down (SOR) should remain unchanged, a single simulation for the preceding ROI period (0 to 1.46 ms) needs to be done for providing initial condition for various cases of simulations considered in the present study. However, the CONVERGE CFD code does not offer this functionality because the code does not store reaction space solutions obtained from RIF solver; thus, when the simulation stops, all information of the reaction space variables will be lost from random access memory (RAM). To avoid this issue, the *restart* functionality for the RIF solver was incorporated in the GTFOAM code development. As such, total simulation time was able to be substantially reduced for this particular purpose of

the present study.

Figure 5.12 illustrates the combustion recession behaviors (dashed lines) for various linear ramp-down profiles. In this analysis, the sudden drop of LOL indicates the inception of the combustion recession for each case. The first two cases are associated with relatively instantaneous ramp-down profile; (e.g., 20 μs for case 1, and 40 μs for case 2). Although onset of combustion recession for these two cases are found at the same time instance, the strength of combustion recession (drop-distance of LOL) varies significantly. The slow ramp-down profile (case 3) appears to delay the combustion recession but sustain the high-temperature reaction in the near-nozzle location longer than other cases. Therefore, it can be argued that slowly closing injector needle is in favor of combustion recession occurrence, thus promoting combustion to recede towards the injector and completely burning unburned or partially burned fuel molecules.

The influence of EOI transient on the high-temperature reaction zone and ambient gas flow are pictorially illustrated in Figure 5.13. The figures present temporal change of the phenomena of interest under fast ramp-down EOI (case 2) and slow ramp-down EOI (case 3) conditions. As discussed in Figure 5.12, the recession of high-temperature reaction zone indicated by high OH concentration is observed for both cases. However quantitative difference between the cases is found in OH concentration; i.e., the slow ramp-down (case 3) EOI profile appears to create more intense combustion recession zone (higher concentration of OH radical) in the near nozzle location, and the receded reaction zone is extended more closely towards the injector, while the fast ramp-down (case 2) generates weak combustion in terms of OH concentration. This indicates that high-temperature combustion kernels upstream field may be sustained long enough to fully burn remainder of fuel vapor, yielding potentially low concentration of UHC emissions.

On the other hand, in Figure 5.13, qualitative difference between two test cases

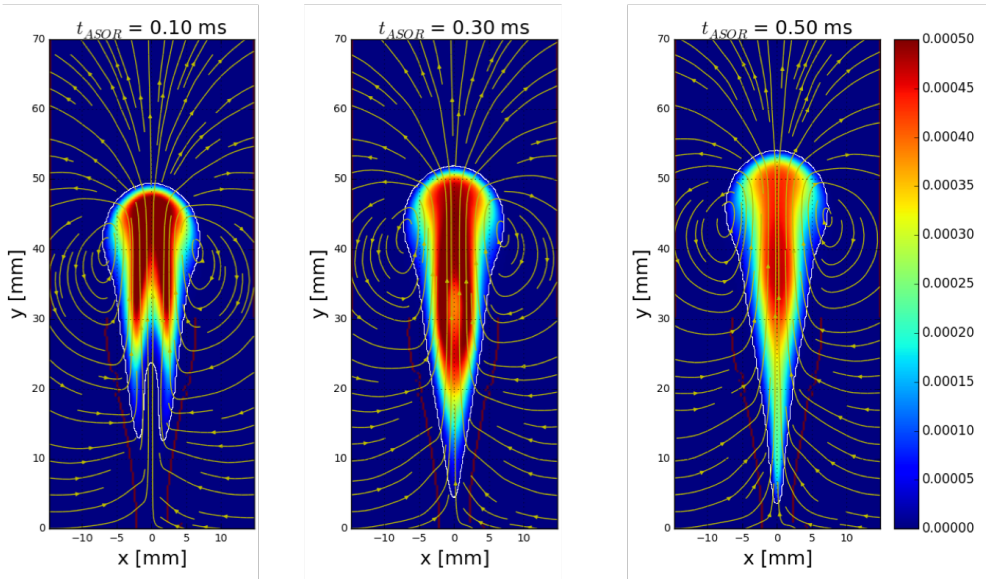

(a) *Case 2 (fast ramp-down)*

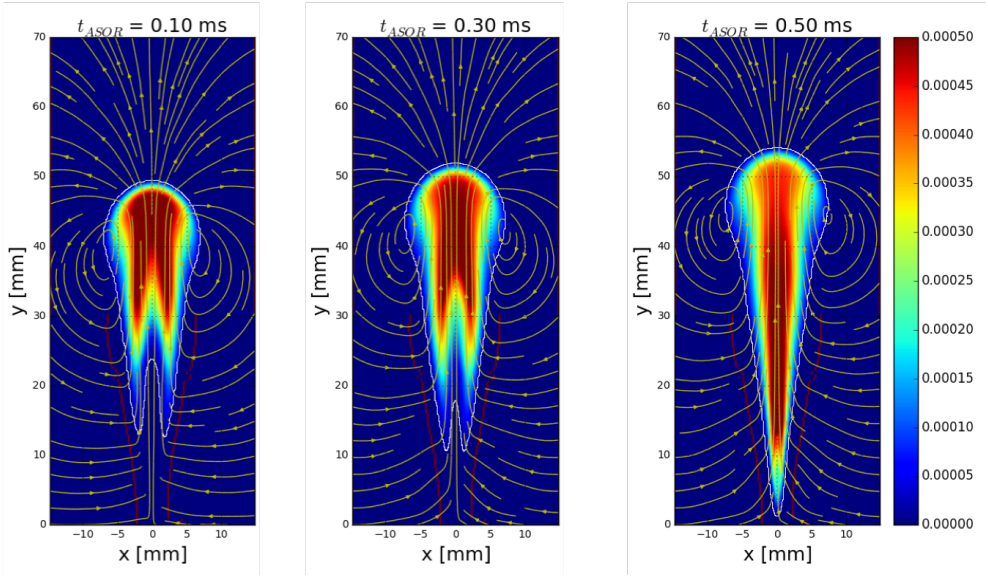

(b) *Case 3 (slow ramp-down)*

Figure 5.13: *OH concentration and ambient gas velocity streamlines with spray boundary lines (indicated by red solid line) during combustion recession occurence*

can be found in the ambient gas flow field indicated by the streamlines on the same figures. Immediately after start of ramp-down incidence happens (see t_{ASOR} = 0.1 ms), a sudden disturbance of streamline is made as shown in Figure 5.13a. This finding suggests that the sudden fuel cut immediately create discontinuous of fuel jet downstream of injector; thus, the region where the fuel jet is absent may experience

weakened air entrainment due to no presence or reduction of driving inertia of the liquid jet. Then, the air flux coming radially inward may chase the liquid jet which has traveled further downward; therefore it may also enhance the air entrainment further downstream; this is an evidence of entrainment "wave", which was identified by earlier studies [49, 61, 64, 163]. Such a process is indicated by curved streamlines in the near nozzle location.

The aforementioned air entrainment wave can be quantitatively identified by tracking temporal variation of air entrainment flux. However, calculation of the entrainment flux is not necessarily straightforward and depends on the definition of the local jet boundary. To this end, Eagle and co-workers [164] have recently proposed a criterion for defining the jet boundary based on the local minimum in the product of radial distance r and radial velocity u_r; i.e., ru_r. This definition has been proved to be robust in the presence of axial flow gradients within the ambient gases surrounding the jet. To test the validity of this method, it has been deployed to obtain the jet boundary for the present Spray A condition between 0 and 30 mm from the injector. To apply this method, ensemble-averaged ru_r during the quasi-steady injection period was calculated. Then, along the spray axial location, the radial location where minimum ru_r is met is considered as the boundary to calculate the entrainment flux during the EOI transient. The resultant spray boundary is indicated by red solid line in Figure 5.13. For simplicity, details of this calculation method are not repeated in this thesis; readers are encouraged to read author's publication [165] for details of the present post-processing technique.

Figure 5.14 displays the normalized entrainment flux. The calculated air entrainment flux quantities through the spray boundary in Figure 5.13 were normalized against the state-state value which can be obtained at $t_{ASOR} = 0.0$ ms. Therefore, the lines plot relative entrainment flux; e.g., the quantity greater than 1.0 means that the air entrainment has been increased during EOI transient. To further understand

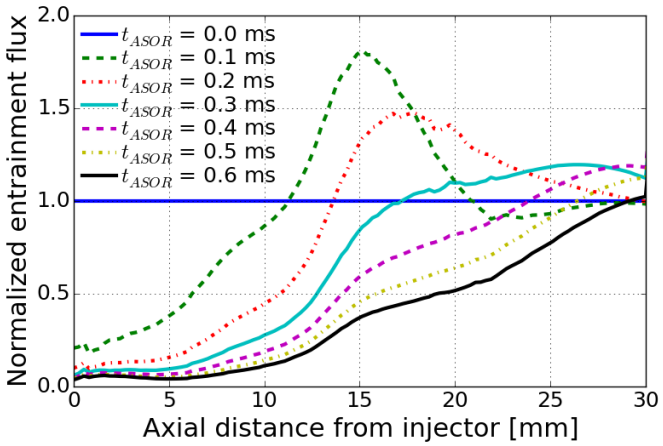

(a) *Case 2 (fast ramp-down)*

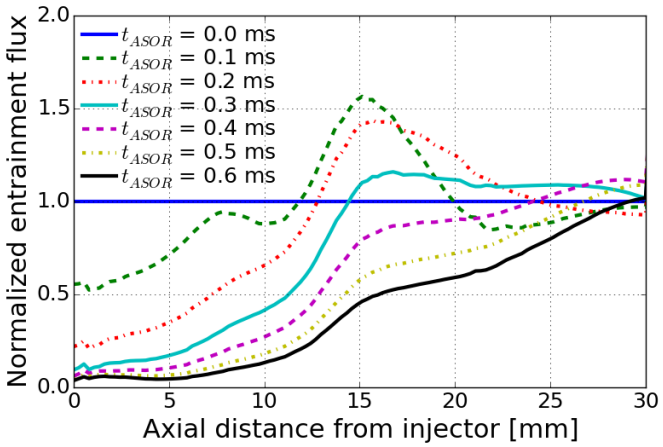

(b) *Case 3 (slow ramp-down)*

Figure 5.14: *Temporal change of ambient air entrainment flux normalized to stead-state (t_{ASOR} = 0.0)*

the presence of entrainment wave which was discussed in Figure 5.13, it is important to identify sudden drop of entrainment flux immediately after SOR. Both cases generated normalized entrained flux less than 1.0 for axial locations 0.0 mm $\sim$ 10 mm at t_{ASOR} = 0.1 ms; sudden cut or reduction of fuel feed in this region rapidly disturbs the air incoming flux through the spray boundary. As already mentioned, this change may augment the air flux increase further downstream; thus, conversely the entrainment flux from 10 mm to 20 mm is then increased at the same time. This augmented air entrainment flux appears to shift downward in time, and the slow

ramp-down in Figure 5.14b is shown to move the "wave" relatively slowly compared to the fast ramp-down case.

This increased entrainment flux is important in discussion of leaning process of fuel-air mixture during EOI transient. More enhanced air entrainment flux in fast ramp-down (case 2) is then characterized by fast leaning process; thus, it is more likely to form overly lean mixture yielding weak combustion recession. In contrast, less augmented entrainment flux may lean the fuel-air mixture relatively slowly; hence the onset of combustion recession may be initiated later in time compared to the former case. As a result, the EOI induced air entrainment change is strongly correlated with the combustion recession behavior as both illustrated in Figure 5.13 and Figure 5.14.

5.2.5 Implications of TCI modeling in Combustion Recession Phenomenon

In this chapter, two category of TCI modeling approaches, i.e., kinetics-controlled combustion model and mixing-controlled combustion model, are examined. For the former setup, well-stirred reactor (WSR) model was used and this model is generally incorporated in a method of direct integration of reaction source term; i.e., reaction rate method. For the latter setup in this study, the representative interactive flamelets (RIF) incorporated with Eulerian particle flamelet model (EPFM) approach was examined as a primitive variable method. These two approaches have been explored in the general diesel spray combustion test metric; thus, general features of diesel spray flame ignition time delay and lifted flame dynamics were predicted by using these two different models. Also, a new opensource sub-model library, GTFOAM, for diesel spray combustion simulation has been developed for further examinations. Using the mixing-controlled physics incorporated in the RIF model approach allows for moderate level of predictive capability in RANS simulations.

In addition, a new direct injection combustion test metric has been suggested for model test platform. The combustion recession is rather unexplored topic especially

in computational modeling study. As the combustion recession was identified to be strongly related to both turbulent mixing and chemical kinetics (first stage ignition) and emerges as a result of competition between them, the mixing process as well as detailed chemistry should therefore be properly taken into account for accurate modeling of the combustion recession dynamics.

In regard to the subjects mentioned above, important finding and consequent implications can be summarized as follows:

- General difference between WSR model and RIF model can be found in prediction of turbulent mean flame brush. The kinetics-controlled model (WSR model) excludes the effect of higher order moment terms in the reaction source term; thus, the model may be optimized to predict laminar chemistry dominating combustion dynamics. In turn, the WSR model produces unrealistically thin reaction zone across the mixture fraction space. In addition, since this model employs a closed reactor with perfect homogeneity for each computational cell, it cannot represent the influence of turbulence and strain effects on diffusion flames; consequently, combustion equilibrium is more likely to be predicted.

- The RIF model, based on flamelet model approach, was found to better perform with aid of sufficient number of flamelet libraries by the Eulerian particle flamelet model (EPFM) approach. Essentially, the model is capable of reproducing the effects of a strained diffusion flame. Moreover, the incorporation of presumed PDF statistics enables to achieve predictions that mimic the characteristics of turbulent flame intermittency; thus, the predictions show a wider reaction zone and lower peak OH concentrations across the mixture fraction space.

- Despite some level of success in general feature of diesel combustion, the present study found some shortcomings of the RIF model, finding that it produces an

oscillatory behavior in the heat release rate and flame lift-off length in time. This appears related to inaccuracies in the temporal and spatial development of scalar dissipation rate within flamelet solutions, which arise when individual flamelets occupy a large range of spatial and/or temporally varying mixtures. Increasing the number of flamelets can mitigate this oscillatory behavior, but computational costs could be a factor to be concerned.

- The employed combustion models; WSR model and RIF model, were able to capture the general occurrence of combustion recession over the examined test conditions. However, the RIF model seems to better follow the qualitative observance of combustion recession from the experiment, in particular, in the extent of second-stage ignition reactions closest to the injector nozzle. This may imply that the governing physics of combustion recession is rather subject to finite rate of turbulent-mixing process.

- This study reveals important finding in comparison between two different CFD platform; i.e., CONVERGE vs. GTFOAM. Especially, the RIF model in GTFOAM was implemented in somewhat different way of integrating temperature field in physical space. This affects resolved flame structure with respect to equilibrium solution, which in turn the resolved flame solution of GTFOAM simulation was identified within the equilibrium limit, whereas the CONVERGE simulations obviously presented physically path-dependent solution. Therefore, a further improvement in GTFOAM-RIF modeling may be needed to better account for physically relevant spray flame dynamics. However, such a difference does not significantly discourage the predictive accuracy in capturing ignition delay and flame lift-off length.

- In the present results, the use of RIF model in two different CFD codes consistently leads to retarded ignition compared to the WSR model. This tendency

may be understood by knowing that the RIF model incorporates the impact of scalar dissipation rate, which brings up a role of turbulent mixing intensity in ignition/quenching problem. However, this tendency of ignition delay prediction is opposite to the trend revealed by the earlier literatures; they reported that flamelet based TCI models tend to estimate shorter ignition delay than WSR model. This opposite tendency is attributed possibly to inability of accounting for cool flame wave propagation in the considered chemical mechanism. Therefore, further investigation needs to be carried out with multiple choice of chemical mechanisms.

- This thesis also reveals important findings in regard to end-of-injection (EOI) profile effect on combustion recession transient. As the combustion recession is considered an outcome of comprehensive effect of mixing-induced air entrainment and finite rate of ignition, the change in rate of ramp-down profile in ROI may significantly alter the onset of combustion recession and consequent emission characteristics. Therefore, altering EOI profile may be regarded as an important strategy in emission controls.

CHAPTER 6

INVESTIGATION OF DUCTED FUEL INJECTION (DFI) FOR NON-SOOTING DIESEL COMBUSTION

Ducted fuel injection (DFI) is a newly developed technology for achieving non-sooting diesel flame in compression ignition engine. The principle behind this technique is to enhance fuel-air mixing and accordingly obtain lean mixture charge prior to partially premixed combustion. Toward this goal, increased mixing residence time is essential; thus, incorporating a small duct in front of injector nozzle such that the injected fuel travels through the small channel maintaining its inertia without being exchanged with ambient air momentum. In this strategy, secondary mixing is achieved by entraining ambient air downstream of nozzle exit as sketched in Figure 6.1, yielding lean lifted flame combustion (LLFC).

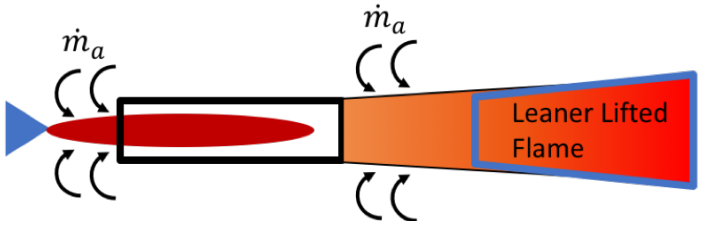

Figure 6.1: *Conceptual schematic of leaner lifted flame combustion (LLFC) achieved by ducted fuel injection (DFI) strategy*

In this chapter, preliminary investigation of ducted fuel injection (DFI) is conducted to present the feasibility of DFI for non-sooting diesel flame under engine relevant conditions. The primary objective of this investigation is thus to determine if this new diesel combustion strategy is viable in further considerations of DFI design parameters and turbulence-chemistry interaction (TCI) modeling strategy, which have never been investigated to this date.

6.1 Demonstration of Leander Lifted Flame Combustion (LLFC) by DFI Strategy

Following sections demonstrates the effectiveness of DFI strategy in enhancing turbulent fuel-air mixing and achieving LLFC configuration. To this end, a preliminary setup of numerical simulation for non-reacting spray and reacting spray under ECN Spray A injection condition (21% oxygen and T_{amb} = 900 K) was made. The simulations were performed using CONVERGE (v2.3.0) [83]. The spray model setup was as consistent as described in section 5.1. The TCI models employed for this investigation are well-stirred reactor (WSR) model and representative interactive flamelets (RIF) model that were validated in the previous chapter.

6.1.1 Non-Reacting DFI Spray

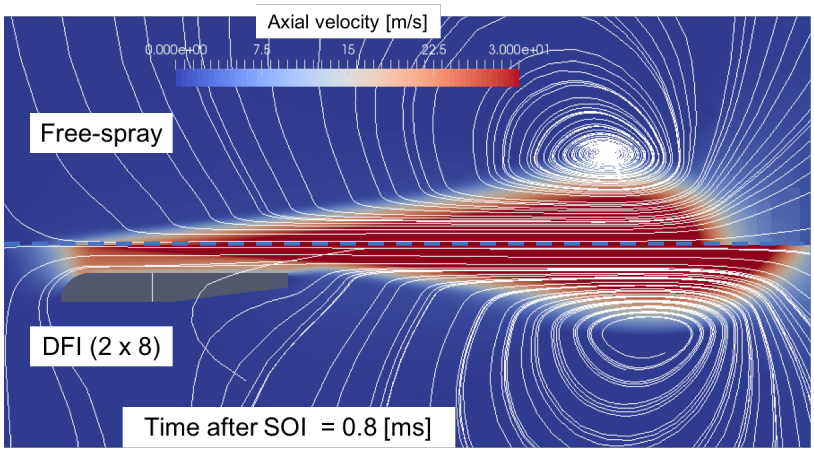

Figure 6.2: *Ambient gas flow streamlines driven by spray injection via free-spray and DFI configurations. DFI was obtained by 2x8 duct channel and nozzle offset G = 3.79 mm*

Figure 6.2 illustrates the difference in spray-driven flow field between free-spray (upper half figure) and DFI spray (lower half figure) configurations under non-reacting ambient gas condition (zero oxygen level). One can notice that the streamlines appear to keep entering into the spray jet via ambient air entrainment in the free-spray jet;

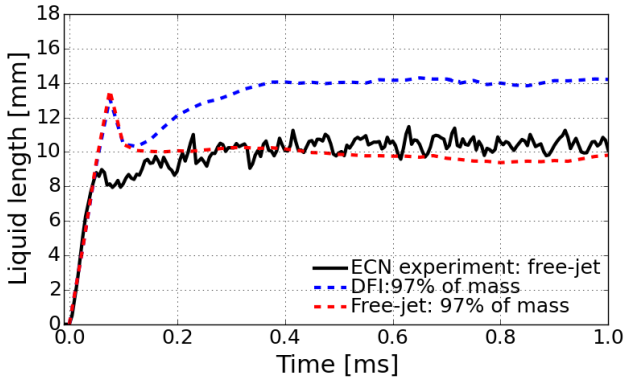

(a) *Liquid penetration*

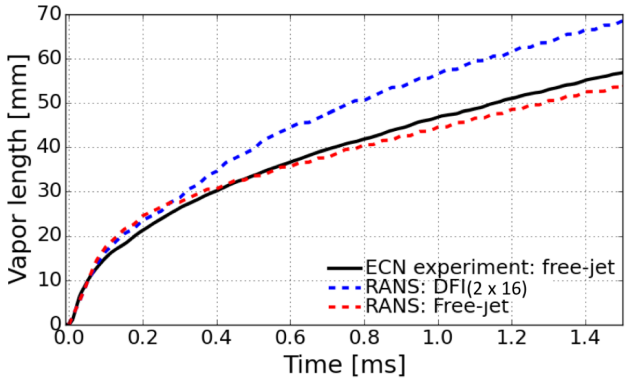

(b) *Vapor penetration*

Figure 6.3: *Effect of DFI configuration on enhancement of liquid penetration and vapor penetration: DFI setup with 2 mm × 16 mm duct dimension*

thus the fuel-air mixing is continuously sustained throughout the jet, whereas the presence of duct (DFI 2x8) prevents the air entrainment from feeding the spray with ambient gas momentum along the duct length; then the secondary fuel-air mixing is allowed downstream of duct exit. Since in the DFI spray the liquid jet may have maintained its inertia to some extent without being disturbed by the ambient air flow, the jet exiting out the duct should convect further downward at higher velocity than the free-spray configuration. The effectiveness of such enhancement of fuel-air mixing by the DFI strategy is demonstrated in Figure 6.3 where the DFI simulation was conducted with 2 mm × 16 mm duct dimension.

6.1.2 Reacting DFI Spray Flame

Burning free-jet spray and ducted fuel injection (DFI) spray were simulated using RANS formulations coupled with well-stirred reactor (WSR) combustion model and Cai mechanism [153] utilizing CONVERGE CFD code [83]. In order to model the soot formation and oxidation, an empirical soot model, namely Hiroyasu-NSC soot oxidation model [166], is offered by the CONVERGE CFD code. This soot model determines production of soot mass within a computational cell from a single-step competition mechanism between soot formation and oxidation.

The test condition was set by the standardized ECN reacting n-dodecane fuel injection and ambient thermodynamic state ($T_{amb} = 900$ K and 21% oxygen level). The tested dimension of straight-shaped duct was defined to 2 x 8 [mm $\times$ mm] for inner diameter and length, and it is placed 3.79 mm downstream of the injector position ($G = 3.79$ mm). The temperature boundary condition on the duct wall was set constant to 900 K with no consideration heat transfer between elevated gas temperature and the wall during the combustion event. Therefore, it may result in some degree of errors in capturing inner flow and ignition process, which are considered for the future investigation.

Figure 6.4 displays the lifted spray flames contoured by temperature and soot concentration captured at 1.3 ms after start of injection. From the results, the ducted spray flame is found to be further lifted downward compared to the free-jet spray flame in Figure 6.4a, yielding weak concentration soot quantity across the entire reacting spray jet in Figure 6.4b. This is believed to be due to the leaner and less stratified mixture formation prior to premixed combustion phase, since the duct may have promoted the secondary mixing after the spray jet penetrates through the duct channel. The cross-sectional average soot mass is also quantified along the spray axis and presented in Figure 6.5; thus the use of DFI strategy in reacting spray flame is proven effective for leaner lifted spray flame and less soot emission.

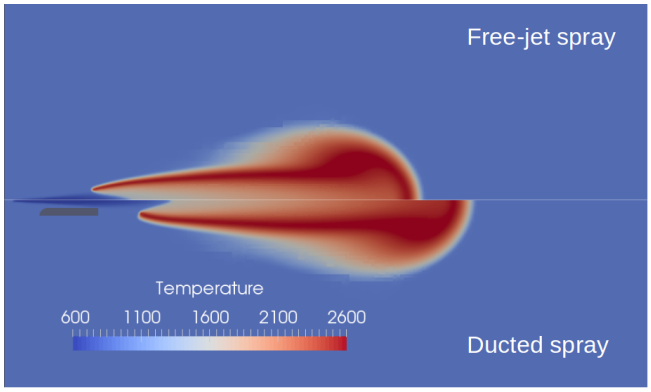

(a) *Temperature [K]*

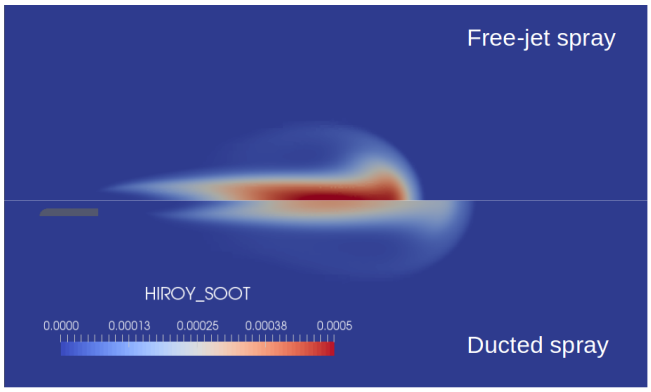

(b) *Hiroyasu soot concentration [-]*

Figure 6.4: *Effect of DFI configuration on lifted flame and reduction of soot emission*

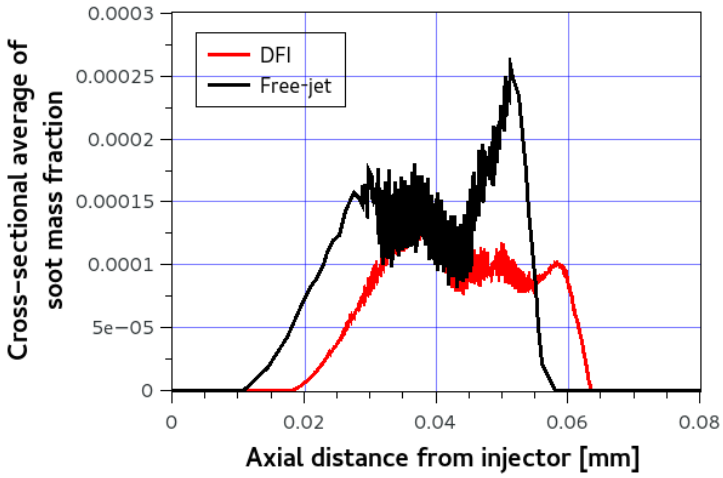

Figure 6.5: *Effect of DFI on reduction of soot formation. Cross-sectional averaged soot concentration captured at* $t_{ASOI} = 1.3$ *ms*

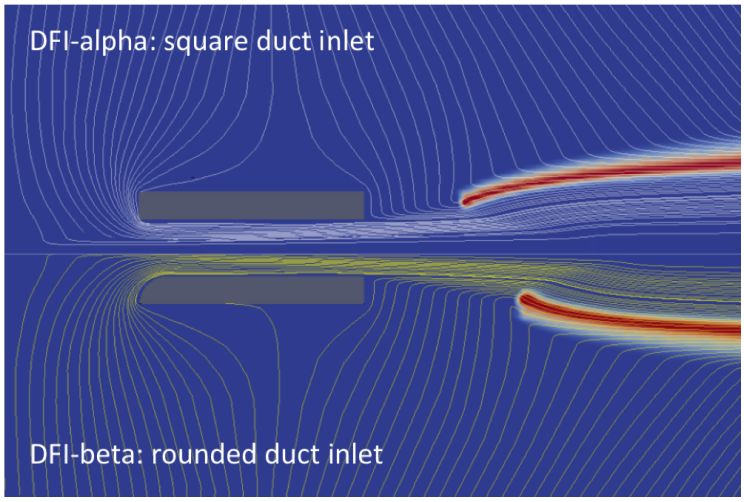

(a) *Impact of duct inlet geometry on gas flow stream and lifted flame height.*

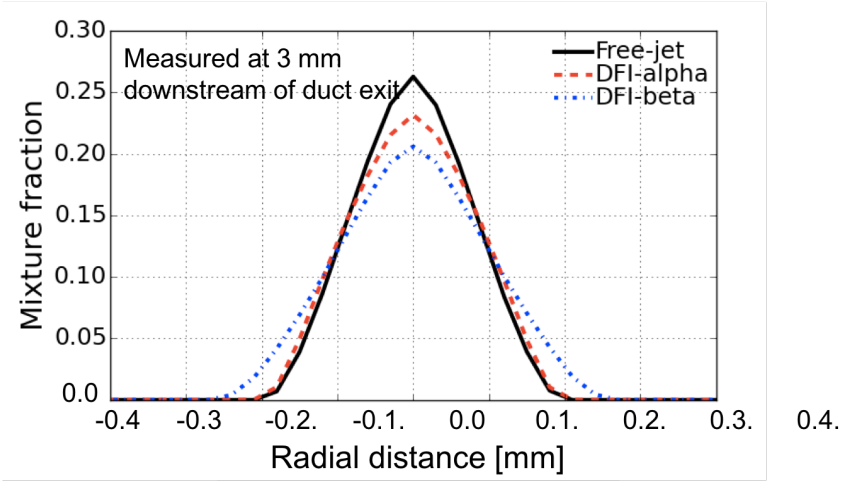

(b) *Impact of duct inlet geometry on radial distribution of mixture fraction: mixture fractions were measured at 3 mm downstream of duct exit for DFI and same downstream position for free-jet spray flame*

Figure 6.6: *Effect of duct inlet shape on LLFC characteristics: DFI alpha (square inlet) vs. DFI beta (rounded inlet)*

Under the notion that the presence of duct along the passage of spray jet significantly affects the lifted flame, it is obvious to anticipate influence of geometric parameters on LLFC characteristics. In this regard, Figure 6.6 demonstrates the impact of inlet geometry of the duct on the fluid flow and flame stabilization. Two different configurations of inlet shape (i.e., DFI-alpha vs. DFI-beta) were adopted in the simulations; the curved geometry (DFI-beta) appears to form smooth curved

streamline across the inlet portion of duct and result in extended lifted flame height as shown in Figure 6.6a. The rounded inlet shape is also found to be beneficial in forming relatively leaner mixture and spreading the mixture outward compared to other tested cases as shown in Figure 6.6b.

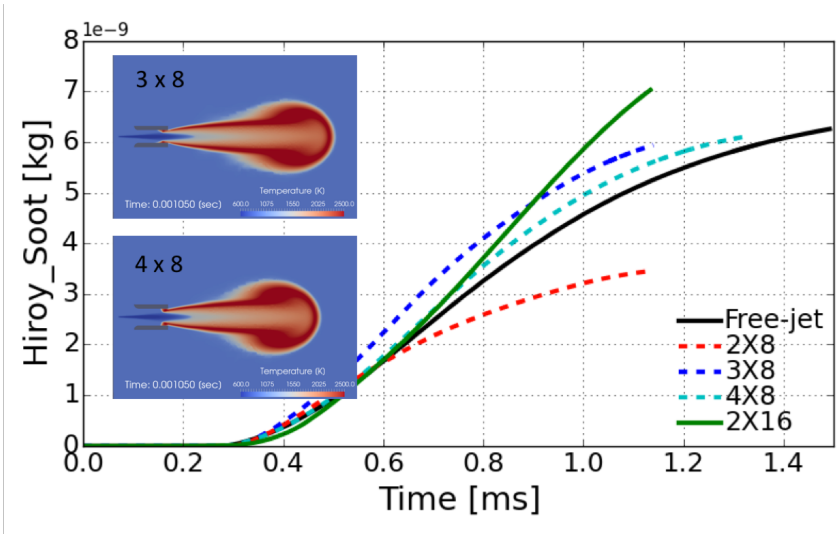

Figure 6.7: *Observation of anchored flame at duct exit as the size of inlet duct diameter increases. Simulations were conducted using WSR model at ECN Spray A condition with 21% oxygen.*

Figure 6.7 shows the variation of accumulated soot quantity across different setup of duct dimensions in length and inner diameter. Although the previous setup with 2x8 DFI showed promising pathway of non-sooting diesel combustion, further increase in inner diameter and duct length lead to increased soot quantity; as illustrated in the sub-figures the flames are found to propagate back sitting inside the duct channel, i.e., non-lifted flame. One possible reason behind this observation can be explained by the occurrence of flow recirculation zone anchoring in the vicinity of duct exit with increase of inner diameter. In other words, bigger diameter of duct may increase likelihood of finding velocity gradient towards the wall; thus, such a condition may recirculate the flow and possibly increase flow residence time. For this reason, the fuel-air mixture formed within the duct channel may ignite before exiting the duct. In RANS simulation framework, the recirculation zone may not be explicitly captured

by the affordable grid resolution (e.g., 0.25 mm in this study); hence the recirculation zone is often estimated by a stagnation point with no convective velocity scale. Nevertheless, such a static fuel-air mixture formation in that region may promote emergence of anchored flame.

The increase of soot quantity can be reasoned by absence of the secondary air entrainment flux; i.e., the failure of achieving lifted flame means no secondary fuel-air mixing downstream of duct exit, and therefore results in very rich mixture burning. As a result, high level of soot formation is expected. However, this tendency of prediction results is not consistent with the recent experimental observations [69].

6.1.3 Impact of TCI modeling on Prediction of DFI Combustion

In the previous section, the simulations with WSR model setup yield failure of LLFC predictions in certain setup of duct dimensions. This might be due to lack of influence of local turbulent intensity in combustion model employed. To be specific, the WSR model follows the constant volume homogeneous reactor assumption; thus, even if there exists high intensity of turbulent mixing, autoignition may initiate if local mixture residence time has elapses on the order of ignition time delay for local equivalence ratio. For instance, occurrence of the anchored flame within the flow recirculation zone (i.e., static fuel-air mixture zone in the RANS simulation) can be explained by this scenario, that is, if flow recirculates on the wall, locally formed fuel-air mixtures may not rapidly convect down yielding burning mixture within the duct channel. However, one lacking physics in the WSR model is the impact of local turbulent intensity on autoignition behavior. Since the local turbulent intensity represented by the scalar dissipation rate χ may be sufficiently elevated in the recirculation zone, the mixture burning should have been delayed, so high-temperature reaction zone appears further downstream.

The finding of aforementioned prediction encourages to apply the turbulence-

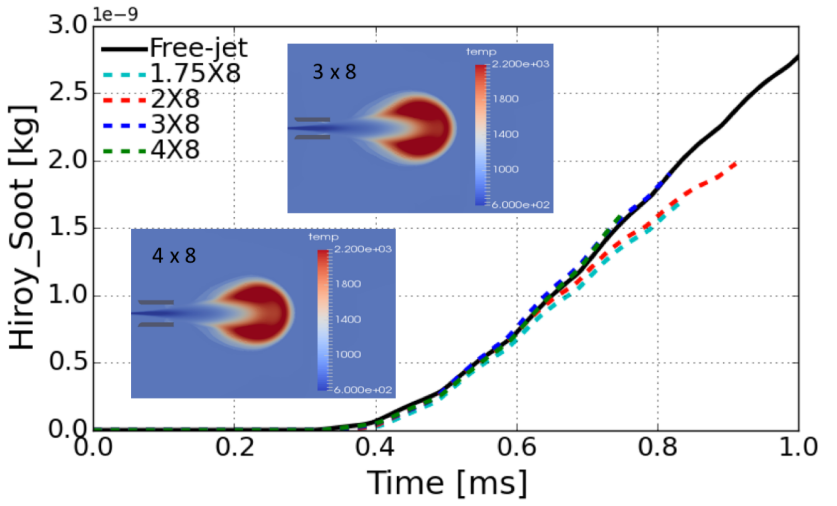

Figure 6.8: *Observation of spray flame lifted off duct exit achieved by RANS simulation coupled with TCI model. RIF model with 20 flamelets used.*

chemistry interaction (TCI) model as mixing-controlled combustion model. Since the RIF model with multiple flamelets setup enabled to predict closely agreeable combustion test metrics in the previous chapters, several simulations were further attempted with the RIF model setup, and the results are presented in Figure 6.8. The cases of inner diameter setup that showed failure of LLFC are now able to present lifted flame and present less soot quantity than the free-jet spray flame. In addition, a new simulation with smaller inner diameter (i.e., 1.7x8 DFI) was conducted, and this shows very similar soot transient with the baseline (2x8 DFI) setup. Therefore, this may imply some degree of convergence of soot transient tendency with inner diameter setup. It is also interesting to find that the 3x8 and 4x8 DFI setups yield almost same soot quantity with the free-jet spray. Accordingly, 2 mm of diameter appears to be the best affordable setup for the ECN Spray A injector.

General belief about the relationship between flame lift-off length (LOL) and soot quantity lies on their inverse proportional correlation; i.e., longer LOL gives rise to less soot quantity. The primary reason is because the longer LOL often ensures more air entrainment flux prior to ignition. However, such a relationship may not hold for

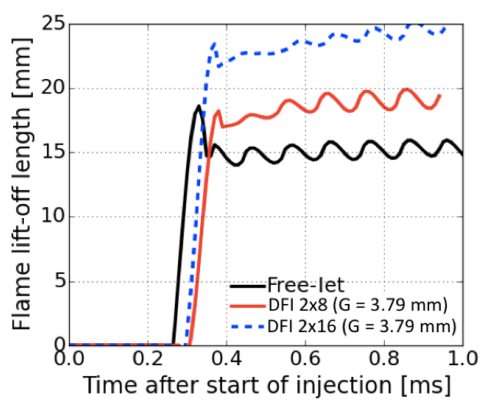

(a) *Flame lifted-off length from injector*

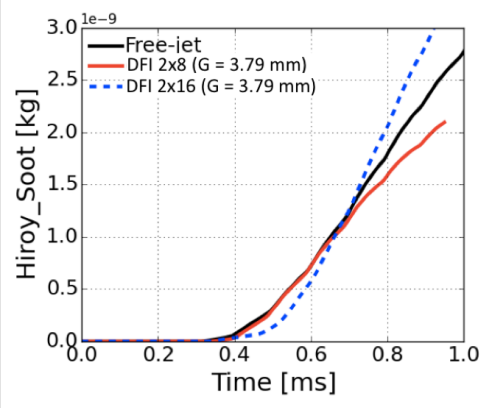

(b) *Accumulated soot formation in time*

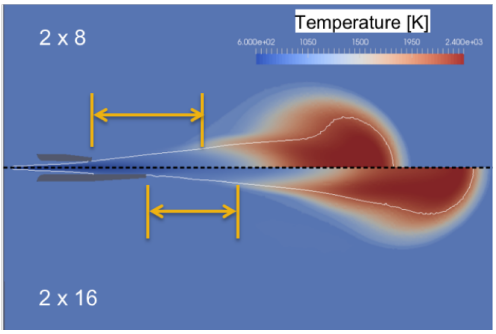

(c) *New flame lift-off length from duct exit*

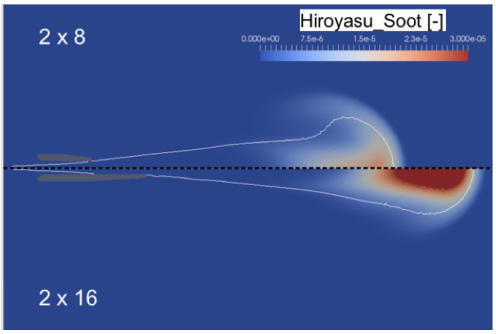

(d) *Soot concentration [-]*

Figure 6.9: *Effect of duct length on flame lift-off length and soot formation. The flame lift-off lenth is defined from the injector location, but new lift-off length from the duct exit is highlighted in (c) by yellow arrows*

the DFI with variation of duct length, and the following results may suggest to define new definition of LOL in DFI study.

Figures 6.9a and 6.9b illustrate variation of LOL and soot transient depending on the duct length change; 2x8 vs. 2x16. In Figures 6.9a, elongated duct channel makes lifted flame stabilize further away from the injector than the free-spray and 2x8 DFI. However, the soot quantity is found to be increased with the 2x16 DFI setup as shown in Figure 6.9b. Since the length of duct is included in the LOL measurement, a new LOL definition may be necessary in order to assess the correlation of soot emission with the lifted-flame. Figure 6.9c shows temperature contour between 2x8 and 2x16 DFI configurations, and the lifted flame heights are indicated with respect to the duct

exit position, namely effective flame lift-off length (eLOL). From the result, eLOL for the 2x8 DFI case is longer than that of 2x16 DFI, and it can be argued that the longer eLOL allows for more ambient air entrainment between duct exit and lifted flame height; hence resulting soot may have been reduced effectively as shown in Figure 6.9d.

6.2 Implications of DFI Preliminary Study

This chapter has presented the first computational study of non-sooting flame technique by using ducted fuel injection (DFI) strategy. Since this technique is a relatively new methodology, many details including governing physics and design parametric effects are largely unknown. Recent two experimental literatures have attempted to demonstrate its effectiveness in non-sooting flame. Based on the basic outcome from those studies, further in-depth knowledges are gained by the present study and summarized as shown below:

- The ducted fuel injection (DFI) benefits from the enhanced fuel-air mixture and yields elongated height of lifted flame; thus, more ambient air-entrainment flux is allowed prior to partially premixed combustion phase resulting in leaner mixture. As a result the DFI configuration is proven to be effective to further reduce soot quantity.

- The primary principle behind this success is that the duct helps to sustain liquid spray momentum without being slowed down, and thus enhances turbulent mixing intensity represented by scalar dissipation rate. As a result, more intense air entrainment can be promoted downstream of duct exit and results in further distanced down lifted flame. Accordingly, the primary role of DFI setup is to enhance turbulent mixing and increase flow residence time.

- Therefore, turbulent mixing plays an essential role in DFI generated non-sooting

flame. However, the use of WSR model in DFI simulations leads to lacking experimentally observed tendency of lifted flame with extended duct dimension. In this regard, it is important to find that the use of RIF model that accounts for the role of scalar dissipation rate enables to capture experimentally observed DFI lifted flame characteristics.

- A few attempts of duct inlet geometry and dimensional parametric investigations were done in this study. The results imply some degree of duct diameter size convergence as well as strong sensitivity of duct length on the sooting flame. In order to convince the feasibility of the DFI application for diesel engines, systematically well-designed studies are needed; e.g., optimized duct length and duct convergence/divergence angle, and broad range of ambient gas thermodynamic conditions need to be considered for future study.

- Although the present discovers important physics governing the DFI flame characteristics, many parametric impact and additional modeling impact remain unanswered since the modeling setups and test duct dimensions were somewhat limited. For example, the effect of heat transfer between duct wall and spray plume may greatly affect the lifted flame structure and emissions. Also, change in thermodynamic state of ambient gas (e.g., varying engine load) may significantly alters the LLFC structure. Therefore, more follow-up investigation are necessary to optimize the DFI configuration.

CHAPTER 7

CONCLUSIONS AND FUTURE WORK

This chapter is dedicated to summarize the primary conclusions and contributions from the studies conducted in this thesis. Recommendations for future investigations are also presented.

7.1 Thesis Contributions

Although the use of low temperature combustion (LTC) techniques have drawn many attentions as an effective way of low NOx and non-sooting combustion, a large portion of spray atomization and combustion physics under LTC relevant conditions has not been fully explored and understood in the CFD modeling aspect. Moreover, a few recent experimental studies have demonstrated potentials of further reduction of soot and unburned hydrocarbon (UHC) emissions by manipulating injection strategy; e.g., combustion recession associated with end-of-injection (EOI) rate shaping and ducted fuel injection (DFI) combustion. However, limited understandings on these new techniques are allowed until now due to lacking of multi-dimensional analysis in the experimental measurements. In order to enable predictive multi-dimensional CFD simulations for those new diesel engine techniques, understanding the governing physics is prerequisite and adequate model selection and/or development accounting for important governing physics is necessary. Toward this goal, a central aim of this thesis is to provide comprehensive understandings of spray atomization and combustion especially at LTC relevant conditions in terms of several physics keywords, and ultimately suggest improved modeling pathways viable for engineering level research CFD platform.

The preceeding chapters presented comprehensive modeling approach including LTC environment adjusted new spray modeling, and turbulence chemistry interaction (TCI) in consideration of finite rate detailed chemistry. This thesis gives full assessment of newly proposed spray atomization model (KH-Faeth model), and then proposes a new primary breakup model (MPT model) that accounts for multi-physics liquid jet breakup mechanisms. Also, in-depth investigations of multi-flamelets RIF model approach against direct integration method (WSR model) are presented with complete assessment of the model predictive capability in new engine combustion test metric, i.e., combustion recession. Those combustion models are further examined in new non-sooting combustion technique (i.e., DFI combustion). To highlight those achievements in this thesis, following sections repeat important findings from the investigations and summarize key contributions.

7.1.1 Development of New Turbulence-Induced Primary Breakup Model

In Chapter 3, two turbulence-induced primary breakup models are introduced. First of all, the KH-Faeth primary breakup model was recently developed by Magnotti [91]; this model represents the hybrid approach of modeling primary breakup that may appears in the form of aerodynamic breakup and nozzle-generated turbulence breakup. Although development of the KH-Faeth was rigorously based on the Wu and Faeth's theories [29] experimentally demonstrated by the same authors, the model has not been fully examined under low ambient gas density conditions in favor of turbulence induced primary breakup regime. Hence, this thesis first presents model validation against the classical modeling approach (i.e., KH model) and new x-ray diagnostics measurement across broad range of engine operating conditions spanning from LTC regime to HTC regime. The results from the previous sections informed that the KH-Faeth model has better predictive capability in capturing rather low ambient density targeted to LTC engines; this is attributed to the fact that the model properly

represent the predominance of nozzle-generated turbulence breakup over the aerodynamically induiced breakup at low ambient density conditions. However, as the ambient density increases up to the level representing HTC conditions, predictions by the KH-Faeth model give rise to some degree of deviation from the measurement. This implies that aerodynamically induced breakup may have not been suitably represented by the model assumption; i.e., KH breakup model may dominate the breakup process at high ambient density conditions.

Secondly, a new primary breakup model is proposed in Chapter 3. The model, i.e., multi-physics turbulence (MPT) model, is an extended version of KH-Faeth model in the fact that the MPT model borrows same framework of turbulence breakup from the KH-Faeth model, but assumption of the aerodynamically induced breakup differs from the hypothesis of KH wave induced breakup. The primary assumption of the MPT model in turn synthesizes the Wu and Faeth's theories [29, 30] behind the breakup mechanisms relevant under a wide range of ambient density conditions in order to provide improved model applicability across wide range of engine conditions. Three distinctive primary breakup mechanisms are therefore included in this model; e.g., (i) nozzle-generated turbulence breakup, (ii) aerodynamically enhanced turbulence breakup and (iii) merged primary/secondary breakup.

In the MPT model, a major model improvement was allowed from the test under high ambient gas density condition where the impact of aerodynamic force may be significant, where both KH model and KH-Faeth model were unsuccessful in SMD predictions. The improvement may be attributed to the model assumption capable of representing relevant aerodynamic force in combination of turbulence breakup. The improvement was found to be obvious in SMD predictions in both axial and transverse directions against new x-ray assisted measurement techniques, i.e., USAXS and SAMR.

Despite a certain degree of improvement in predictions, further investigations

may be required to fully justify the prediction capability of the MPT model because sufficient experimental data set for droplet statistics in near-nozzle location is still not allowed using the combination of USAXS and SAMR measurements.

7.1.2 Preliminary Study of Combustion Recession

In Chapter 4, a preliminary study of combustion recession was conducted using partially-stirrec reactor (PaSR) model and a choice of two chemical mechanisms; e.g., Cai mechanism [153] and Yao mechanism [154]. The test simulations were conducted in OpenFOAM (v2.4) platform, which was original OpenFOAM code basis without modification in spray and combustion models considered.

Due to incomplete Lagrangian droplet models incorporated in the original OpenFOAM, some degree of inaccuracy was observed in the non-reacting Spray A simulation; e.g., noticeable errors in unsteady spray penetrating length in time. This implies that momentum exchange process modeled by the OpenFOAM code may have not been well representive of realistic turbulent mixing process. This shortcoming of the original spray model platform encouraged new development of the Lagrangian spray model library for OpenFOAM platform, which was then used in the investigation in Chapter 5. In addition, important finding was obtained from the investigation on two chemical mechanisms employed. The Cai's chemical mechanism [153] was only able to properly capture the combustion recession behavior as consistently as the recent experimental observations.

This preliminary investigation provided important understandings of combustion recession dynamics in several different ways. First of all, using scaling analysis with specially defined Da number, it is revealed that the likelihood of combustion recession is an outcome of competition between turbulent mixing (combustible fuel-air mixture preparation) and finite rate chemical kinetics. In addition, for detail analysis, a new Lagrangian flow tracking method was developed. This technique allows to track

fluid elements spatiotemporarily such that it helps to gain further insights about the process of combustion recession dynamics in terms of mixing and chemical reaction. This new method of algorithm may also be utilized for run-time based (dynamically) analsys of reactive scalars of interest.

7.1.3 Turbulence-chemistry interaction (TCI) modeling in diesel spray flame and combustion recession

In Chapter 5, two category of TCI modeling approaches, i.e., (i) kinetics-controlled combustion model and (ii) mixing-controlled combustion model, were examined. The first model setup was incorporated with the well-stirred reactor (WSR) model as a non-TCI model, and the second model setup was made with RIF model with aid of multi-flamelets approach (i.e., Eulerian particle flamelet model, EPFM). These two approaches have been explored in the general diesel spray combustion test metric; i.e., general features of diesel spray flame ignition delay (ID) and flame lift-off length (LOL) were assessed. In addition, a new direct injection combustion test metric, combustion recession, was explored with the TCI modeling setup. The combustion recession is rather unexplored topic especially in computational modeling study. Since the combustion recession was idenfiied to be strongly related to both turbulent mixing and chemical kinetics (first stage ignition), the mixing process as well as detailed chemistry should therefore be properly taken into account for accurate modeling of the combustion recession behavior.

General difference WSR model and RIF model can be found in prediction of turbulent mean flame brush. The kinetics-controlled combustion feature in the WSR model appears to diminsh the effect of turbulent flow intermittency nature, so the WSR model predicted unrealistically thin reaction zone across the mixture fraction space. Furthermore, the model was not allowed to account for unsteady stretched flame effect that appears in the non-equilibrium flame temperature. On the other

hand, The RIF model, based on flamelet model approach, was found to better perform with aid of sufficient number of flamelet libraries by the EPFM approach. Essentially, the model is capable of repro- ducing the effects of a strained diffusion flame. Moreover, the incorporation of presumed PDF statistics enables to achieve predictions that mimic the characteristics of turbulent flame intermittency; thus the predictions show a wider reaction zone and lower peak OH concentrations across the mixture fraction space. However, a notable shortcoming of the RIF model for diesel spray combustion simulations were identified by oscillatory behavior in the heat release rate and flame lift-off length in time. This is related to inaccuracies in the spatiotemporal development of domain-averaged scalar dissipation rate incorporated in the reaction space solution (i.e., flamelet equation).

Both two employed combustion models; WSR model and RIF model, were able to capture the general occurence of combustion recession over the examined test conditions. However, the setup with RIF model better performed in capturing the qualitative observance of combustion recession from the experiment, in particular, in the extent of second-stage ignition reactions closest to the injector nozzle. This may imply that the governing physics of combustion recession is rather subject to finite rate of turbulent-mixing process. This also suggests that the use of flamelet modeling coupled with detailed chemistry may be effective.

This thesis also presents the comparison between two different CFD codes; i.e., CONVERGE vs. GTFOAM. The GTFOAM is a open-source CFD library package developed by the author for further examination of improved Lagrangian models and flamelet model. It is important to know that both codes incorporate temperature resolving method in different ways; the GTFOAM is more biased to predictive variable approach for all reactive scalars. This distinctive feature was found to affect resolved flame structure with respect to equilibrium solution, which in turn the resolved flame solution of GTFOAM simulation was identified within the equilibrium limit, whereas

the CONVERGE simulations obviously presented physically path-dependent solution. Therefore, a further modification in GTFOAM code structure needs to be considered to better account for physically relevant spray flame dynamics.

It is also important point out that the results presented in this thesis shows somewhat opposite trend to earlier literatures in terms of ignition delay prediction by RIF model and WSR model. This controversial finding may likely be attributed to failure in capturing cool flame wave propagation in the employed chemical mechanism. Therefore, a deeper investigation with multiple choice of chemical kinetics model needs to be performed in the near future.

Lastly, in Chapter 5, important findings in effect of varying EOI transient on combustion recession dynamics are presented. Since the combustion recession was identified as an outcome of comprehensive process of turbulent mixing and finite-rate of chemistry, altering the ROI profile especially in end-transient may substantially affect the lifted flame dynamics and emission characteristics. This finding gives important guidance in emission control especially for UHC/CO emissions since they are known to be consumed by the combustion recession process.

7.1.4 Ducted fuel injection (DFI) cobustion for non-sooting flame

Chapter 6 presented the first multi-dimensional computational investigations of non-sooting flame technique obtained by ducted fuel injection (DFI) strategy. This study revealed that the DFI may greatly benefit from the enhanced fuel-air mixture and yields elongated height of lifted flame; thus more ambient air-entrainment flux is allowed prior to partially premixed combustion phase and successfully reduces soot quantity consequently. The enhanced mixing was able to be achieved by sustaining spray momentum while it travels through the duct channel. Then after the spray exit out the duct, more intense air entrainment flux was allowed downstream of duct exit, resulting in further lifted flame stabilization and less stratificed and leaner mix-

ture. Therefore, turbulent mixing plays an essential role in DFI generated non-sooting flame. In this regard, the use of RIF model that accounts for the role of scalar dissipation rate enables to capture experimentally observed DFI lifted flame characteristics.

In this study, a few numbers of trials with duct inlet geometry change and dimensional parametric analysis were done. The results imply some degree of duct diameter size convergence as well as strong sensitivity of duct length on the sooting flame. In order to convince the feasibility of the DFI application for diesel engines, well-designed parametric studies are needed for future work. For instance, thermodynamic state of ambient gas (i.e., represented by engine load conditions) may possibly affect the DFI-induced lifted flame and soot transient. Also, additional modeling impact (e.g., wall-gas heat transfer) has not been considered in this study; thus, further future investigation needs to carefully consider broad range of modeling techniques in order to obtain optimized modeling guidance for better DFI understanding.

REFERENCES

[1] S. Kimura, O. Aoki, Y. Kitahara, and E. Aiyoshizawa, "Ultra-clean combustion technology combining a low-temperature and premixed combustion concept for meeting future emission standards," *SAE Paper 2001-01-0200*, 2001.

[2] S. Kook, C. Bae, P. Miles, D. Choi, and L. Pickett, "The influence of charge dilution and injection timing on low-temperature diesel combustion and emissions," *SAE Paper 2005-01-3837*, 2005.

[3] A. Helmantel, J. Gustavsson, and I. Denbratt, "Operation of a di diesel engine with variable effective compression ratio in hcci and conventional diesel mode," *SAE Paper 2005-01-0177*, 2005.

[4] T. Kanda, T. Hakozaki, T. Uchimoto, J. Hatano, and N. Kitayama, "Pcci operation with early injection of conventional diesel fuel," *SAE Paper 2005-01-0378*, 2005.

[5] W. Hardy and R. D. Reitz, "A study of the effects of high egr, high equivalence ratio, and mixing time on emissions levels in a heavy-duty diesel engine for pcci combustion," *SAE Paper 2006-01-0026*, 2006.

[6] C. L. Genzale, S.-C. Kong, and R. D. Reitz, "Modeling the effects of variable intake valve timing on diesel hcci combustion at varying load, speed, and boost pressures," *Journal of Engineering for Gas Turbines and Power*, vol. 130, no. 052806-1, 2005.

[7] B. Keeler and P. J. Shayler, "Constraints on fuel injection and egr strategies for diesel pcci-type combustion," *SAE Paper 2008-01-1327*, 2008.

[8] D. Kim, M. Y. Kim, and C. S. Lee, "Effect of premixed gasoline fuel on the combustion characteristics of compression ignition engine," *Energy and Fuels*, vol. 18, pp. 1213–1219, 2004.

[9] A. Ghazimirsaied, M. Shahbakhti, and C. R. Koch, "Comparison of crankangle based ignition timing methods on an hcci engine," in *Proceedings of the ASME 2010 Internal Combustion Engine Division Fall Technical Conference, ICEF2010-35087*, 2010.

[10] M. Christensen, B. Johansson, and P. Einewall, "Homogeneous charge compression ignition (hcci) using isooctane, ethanol and natural gas - a comparison with spark ignition operation," *SAE Paper 972874*, 1997.

[11] J. E. Dec and M. Sjoberg, "A parametric study of hcci combustion – the sources of emissions at low loads and the effects of gdi fuel injection," *SAE Paper 2003-01-0752*, 2003.

[12] S. M. Aceves, D. L. Flowers, F. Espinosa-Loza, J. Martinez-Frias, J. E. Dec, M. Sjoberg, R. W. Dibbie, and R. P. Hessel, "Spatial analysis of emissions sources for hcci combustion at low loads using a multi-zone model," *SAE Paper 2004-01-1910*, 2004.

[13] M. P. B. Musculus, T. Lachaux, L. M. Pickett, and C. A. idicheria, "End-of-injection over-mixing and unburned hydrocarbon emissions in low-temperature-combustion diesel engines," *SAE Paper 2007-01-0907*, 2007.

[14] C. P. Koci, Y. Ra, R. Krieger, M. Andrie, D. E. Foster, R. M. Siewert, R. P. Durrett, I. Ekoto, and P. C. Miles, "Detailed unburned hydrocarbon investigations in a highly-dilute diesel low temperature combustion regime," *SAE Paper 2009-01-0982*, 2009.

[15] G. M. Faeth, "Evaporation and combustion of sprays," *Progress in Energy and Combustion Science*, vol. 9, pp. 1–76, 1983.

[16] D. L. Siebers, "Liquid-phase fuel penetration in diesel sprays," *SAE Paper 980809*, 1998.

[17] J. D. Naber, "Effects of gas density and vaporization on penetration and dispersion of diesel sprays," *SAE Paper 960034*, 1996.

[18] D. L. Siebers, "Scaling liquid-phase fuel penetration in diesel sprays based on mixing-limited vaporization," *SAE Paper 1999-01-0528*, 1999.

[19] W. O. H. Mayer and A. H. A. Schik, "Atomization and breakup of cryogenic propellants under high-pressure subcritical and supercritical conditions," *Journal of Propulsion and Power*, vol. 14, no. 5, 1998.

[20] W. O. H. Mayer and J. J. Smith, "Fundamentals of supercritical mixing and combustion of cryogenic propellants," *Progress in Astronautics and Aeronautics*, pp. 339–367, 2004.

[21] R. N. Dahms and J. C. Oefelein, "On the transition between two-phase and single-phase interface dynamics in multicomponent fluids at supercritical pressures," *Physics of Fluids*, vol. 25, no. 092103, 2013.

[22] P. M. Schweitzer, "Mechanism of disintegration of liquid jets," *Journal of Applied Physics*, vol. 8, pp. 513–521, 1937.

[23] M. J. McCarthy and N. A. Molloy, "Review of stability of liquid jets and the influence of nozzle design," *The Chemical Engineering Journal*, vol. 7, pp. 1–20, 1974.

[24] A. M. Sterling, *The Instability of Capillary Jets*. PhD thesis, University of Washington, 1969.

[25] R. A. Castleman, "The mechanism of the atomization accompanying solid injection; n.a.c.a. report 440," tech. rep., NASA, 1932.

[26] R. D. Reitz, *Atomization and other breakup regimes of a liquid jet*. PhD thesis, Princeton University, 1978.

[27] R. D. Reitz and F. Bracco, "Mechanism of atomization of a liquid jet," *The Physics of Fluids*, vol. 25, no. 10, pp. 1730–1742, 1982.

[28] J. J. Taylor and J. W. Hoyt, "Water jet photography - techniques and methods," *Experiments in Fluids*, vol. 1, pp. 113–120, 1983.

[29] P.-K. Wu, L.-K. Tseng, and G. M. Faeth, "Primary breakup in gas/liquid mixing layers for turbulent liquids," *Atomization and Sprays*, vol. 2, pp. 295–317, 1992.

[30] P.-K. Wu and G. M. Faeth, "Aerodynamic effects on primary breakup of turbulent liquids," *Atomization and Sprays*, vol. 3, pp. 265–289, 1993.

[31] P.-K. Wu, R. F. Miranda, and G. M. Faeth, "Effects of initial flow conditions on primary breakup of non-turbulent and turbulent round liquid jets," *Atomization and Sprays*, vol. 5, pp. 175–196, 1995.

[32] W. Bergwerk, "Flow pattern in diesel nozzle spray holes," *Proceedings of the Institution of Mechanical Engineers*, vol. 173, no. 25, pp. 655–660, 1959.

[33] R. Sadek, "Communication on flow pattern in nozzle spray holes and discharge coefficient of orifices," *Proceedings of the Institution of Mechanical Engineers*, vol. 173, no. 671, 1959.

[34] D. J. Duke, A. L. Kastengren, F. Z. Tilocco, A. B. Swantek, and C. F. Powell, "X-ray radiography measurements of cavitating nozzle flow," *Atomization and Sprays*, vol. 23, no. 9, pp. 841–860, 2013.

[35] D. J. Duke, A. L. Kastengren, A. B. Swantek, and C. F. Powell, "X-ray diagnostics for cavitating nozzle flow," *Journal of Physics: Conference Series*, vol. 656, no. 012110, 2015.

[36] I. Khlifa, A. Vabre, M. Hocevar, K. Fezzaa, S. Fuzier, O. Roussette, and O. Coutier-Delgosha, "Fast x-ray imaging of cavitating flows," *Experiments in Fluids*, vol. 58, no. 157, 2017.

[37] Y.-H. Won, T. Kamimoto, H. Kobayashi, and H. Kosaka, "2-d soot visualization in unsteady spray flame by means of laser sheet scattering technique," *SAE Paper 910023*, 1991.

[38] J. E. Dec and C. Espey, "Soot and fuel distributions in a d.i. diesel engine via 2-d imaging," *SAE Paper 922307*, 1992.

[39] C. Espey and J. E. Dec, "The effect of tdc temperature and density on the liquid-phase fuel penetration in a d.i. diesel engine," *SAE Paper 952456*, 1995.

[40] G. Wiltafsky, W. Stolz, J. Kohler, and C. Espey, "The quantification of laser-induced incandescence (lii) for planar time resolved measurements of the soot volume fraction in a combustion diesel jet," *SAE Paper 961200*, 1996.

[41] J. E. Dec, "A coonceptual model of di diesel combustion based on laser-sheet imaging," *SAE Paper 970873*, 1997.

[42] N. Peters, "Laminar diffusion flamelet models in non-premixed turbulent combustion," *Progress in Energy and Combustion Science*, vol. 10, pp. 319–339, 1984.

[43] K. Kuwahara and H. Ando, "Role of heat accumulation by reaction loop initiated by h2o2 decomposition for thermal ignition," *SAE Paper 2007-01-0908*, 2007.

[44] C. K. Westbrook, "Chemical kinetics of hydrocarbon ignition in practical combustion systems," *Proceedings of the Combustion Institute*, vol. 28, pp. 1563–1157, 2000.

[45] J. Chen, T. Litzinger, and H. Curran, "The lean oxidation of iso-octane at elevated pressures," *SAE Paper 2005-01-3734*, 2005.

[46] P. F. Flynn, R. P. Durrett, G. L. Hunter, A. O. Z. Loye, O. C. Akinyemi, J. E. Dec, and C. K. Westbrook, "Diesel combustion: An integrated view combining laser diagnostics, chemical kinetics, and empirical validation," *SAE Paper 1999-01-0509*, 1999.

[47] H. Kosaka, V. H. Drewes, L. Catalfamo, A. A. Aradi, N. Iida, and T. Kamimoto, "Two-dimensional imaging of formaldehyde formed during the ignition process of a diesel fuel spray," *SAE Paper 2000-01-0236*, 2000.

[48] G. Bruneaux, "Combustion structure of free and wall-impinging diesel jets by simultaneous laser-induced fluorescence of formaldehyde, poly-aromatic hydrocarbons, and hydroxides," *Internation Journal of Engine Research*, pp. 249–165, 2017.

[49] M. P. B. Musculus, P. C. Miles, and L. M. Pickett, "Conceptual models for partially premixed low-temperature diesel combustion," *Progress in Energy and Combustion Science*, vol. 39, pp. 246–283, 2013.

[50] A. Krisman, E. R. Hawkes, M. Talei, A. Bhagatwala, and J. H. Chen, "A direct numerical simulation of cool-flame affected autoignition in diesel engine-relevant conditions," *Proceedings of the Combustion Institute*, vol. 36, no. 3, pp. 3567–3575, 2017.

[51] M. Ribaucour, R. Minetti, L. R. Sochet, H. J. Curran, W. J. Pitz, and C. K. Westbrook, "Ignition of isomers of pentane: An experimental and kinetic mod-

eling study," *Proceedings of the Combustion Institute*, vol. 28, pp. 1671–1678, 2000.

[52] J. E. Dec and C. Espey, "Chemiluminescence imaging of autoignition in a di diesel engine," *SAE Paper 982685*, 1998.

[53] J. E. Dec and E. B. Coy, "Oh radicals imaging in a di diesel engine and the structure of the early diffusion flame," *SAE Paper 960831*, 1996.

[54] Y. B. Zeldovich, "The oxidation of nitrogen in combustion and explosions," *European Physical Journal A. Hadrons and Nuclei*, vol. 21, pp. 577–628, 1946.

[55] T. Li and H. Ogawa, "Analysis of the trade-off between soot and nitrogen oxides in diesel-like combustion by chemical kinetic calculation," *SAE Paper 2011-01-1847*, 2011.

[56] T. Kitamura and T. Ito, "Mixing-controlled, low temperature diesel combustion with pressure modulated multiple- injection for hsdi diesel engine," *SAE Paper 2010-01-0609*, 2010.

[57] S. S. Singh, R. D. Reitz, M. P. Musculus, and T. Lachaux, "Validation of engine combustion models against detailed in-cylinder optical diagnostics data for a heavy-duty compression-ignition engine," *International Journal of Engine Research*, vol. 8, pp. 97–126, 2007.

[58] T. Lachaux and M. P. B. Musculus, "In-cylinder unburned hydrocarbon visualization during low-temperature compression-ignition engine combustion using formaldehyde plif," *Proceedings of the Combustion Institute*, vol. 31, pp. 2921–2929, 2007.

[59] S. A. Lewis, J. M. E. Storey, B. Bunting, and J. P. Szybist, "Partial oxidation products and other hydrocarbon species in diesel hcci exhaust," *SAE Paper 2005-01-3737*, 2005.

[60] M. P. B. Musculus, "Multiple simultaneous optical diagnostic imaging of early-injection low-temperature combustion in a heavy-duty diesel engine," *SAE Paper 2006-01-0079*, 2006.

[61] B. W. Knox, C. L. Genzale, L. M. Pickett, J. M. Garcia-Oliver, and W. Vera-Tudela, "Combustion recession after end of injection in diesel sprays," *SAE Paper 2015-01-0797*, 2015.

[62] M. K. Bobba, C. L. Genzale, and M. P. B. Musculus, "Effect of ignition delay on in-cylinder soot characteristics of a heavy duty diesel engine operating at low temperature conditions," *SAE Paper 2009-01-0946*, 2009.

[63] S. A. Skeen, J. Manin, and L. M. Pickett, "Simultaneous formaldehyde plif and high-speed schlieren imaging for ignition visualization in high-pressure spray flames," *Proceedings of the Combustion Institute*, vol. 35, pp. 3167–3174, 2015.

[64] B. W. Knox and C. L. Genzale, "Effects of end-of-injection transients on combustion recession in diesel sprays," *SAE Paper 2016-01-0745*, 2016.

[65] B. Hu, M. P. B. Musculus, and J. C. Oefelein, "The influence of large-scale structures on entrainment in a decelerating transient turbulent jet revealed by large eddy simulation," *Physics of Fluids*, vol. 24, no. 045106, 2012.

[66] B. W. Knox, *End-of-injection effects on diesel spray combustion.* PhD thesis, Georgia Institute of Technology, 2016.

[67] C. J. Polonowski, C. J. Mueller, C. R. Gehrke, T. Bazyn, G. C. Martin, and P. M. Lillo, "An experimental investigation of low-soot and soot-free combus-

tion strategies in a heavy-duty, single-cylinder, direct-injection, optical diesel engine," *SAE Paper 2011-01-1812*, 2015.

[68] C. J. Mueller, "Ducted fuel injection; provisional u.s. patent application 62,058,613," tech. rep., 2015.

[69] C. J. Mueller, C. W. Nilsen, D. J. Ruth, R. K. Gehmlich, L. M. Pickett, and S. A. Skeen, "Ducted fuel injection: A new approach for lowering soot emissions from direct-injection engines," *Applied Energy*, vol. 204, pp. 206–220, 2017.

[70] R. P. Fitzgerald, K. Svensson, G. Martin, Y. Qi, and C. Koci, "Early investigation of ducted fuel injection for reducing soot in mixing-controlled diesel flames," *SAE Paper 2018-01-0238*, 2018.

[71] J. K. Dukowicz, "A particle-fluid numerical model for liquid sprays," *Journal of Computational Physics*, vol. 35, no. 2, pp. 229–253, 1980.

[72] R. D. Reitz and R. Diwakar, "Effect of drop breakup on fuel sprays," *SAE Paper 860469*, 1986.

[73] W. G. Reinecke and G. D. Waldman, "A study of drop breakup behind strong shocks with applications to flight; avco report avsd-0110-70-rr," tech. rep., 1970.

[74] R. D. Reitz, "Modeling atomization processes in high-pressure vaporizing sprays," *Atomization and Sprays*, vol. 3, pp. 309–337, 1987.

[75] A. Liu, D. Mather, and R. D. Reitz, "Modeling the effects of drop drag and breakup on fuel sprays," *SAE Paper 930072*, 1993.

[76] J. C. Beale and R. D. Reitz, "Modeling spray atomization with the kelvin-helmholtz/rayleigh-taylor hybrid model," *Atomization and Sprays*, vol. 9, pp. 623–650, 1999.

[77] S. Som and S. K. Aggarwal, "Assessment of atomization models for diesel engine simulations," *Atomization and Sprays*, vol. 19, no. 9, pp. 885–903, 2009.

[78] T. F. Su, M. A. Patterson, R. D. Reitz, and P. V. Farrell, "Experimental and numerical studies of high pressure multiple injection sprays," *SAE Paper 960861*, 1996.

[79] M. A. Patterson and R. D. Reitz, "Modeling the effects of fuel spray characteristics on diesel engine combustion and emission," *SAE Paper 980131*, 1998.

[80] S. W. Park, H. J. Kim, and C. S. Lee, "nvestigation of atomization characteristics and prediction accuracy of hybrid models for high-speed diesel fuel sprays," *SAE Paper 2003-01-1045*, 2003.

[81] A. A. Amsden, P. O'Rourke, and T. Butler, "Kiva-ii: A computer program for chemically reacting flows with sprays: technical report la-11560-ms," tech. rep., Los Alamos National Laboratory, 1989.

[82] Fluent, *FLUENT 6.2 User's Guide*, 2005.

[83] K. Richards, P. Senecal, and E. Pomraning, *CONVERGE 2.2. Theory Manual, Convergent Science*, 2015.

[84] H. G. Weller, G. Tabor, H. Jasak, and C. Fureby, "A tensorial approach to computational continuum mechanics using object-oriented techniques," *Computers in Physics*, vol. 12, no. 6, pp. 620–631, 1998.

[85] Y. Yue, C. F. Powell, R. Poola, J. Wang, and J. K. Schaller, "Quantitative measurements of diesel fuel spray characteristics in the near-nozzle region using x-ray absorption," *Atomization and Sprays*, vol. 11, no. 4, pp. 471–490, 2001.

[86] J. Wang, "X-ray vision of fuel sprays," *Journal of Synchrotron Radiation*, vol. 12, no. 2, pp. 197–207, 2005.

[87] A. I. Ramirez, S. Som, S. K. Aggarwal, A. L. Kastengren, E. M. El-Hannouny, D. E. Longman, and C. F. Powell, "Quantitative x-ray measurements of high-pressure fuel sprays from a production heavy duty diesel injector," *Experiments in Fluids*, vol. 47, pp. 119–134, 2009.

[88] S. Som, A. I. Ramirez, S. K. Aggarwar, A. L. Kastengren, E. El-Hannouny, D. E. Longman, C. F. Powell, and P. K. Senecal, "Development and validation of a primary breakup model for diesel engine applications," *SAE Paper 2009-01-0838*, 2009.

[89] S. Som and S. K. Aggarwal, "Effects of primary breakup modeling on spray and combustion characteristics of compression ignition engines," *Combustion and Flame*, vol. 157, pp. 1179–1193, 2010.

[90] K. Y. Huh and A. D. Gosman, "A phenomenological model of diesel spray atomization," in *Proceedings of the Internal Conference of Multi-phase Flows*, 1991.

[91] G. M. Magnotti, *Modeling the influence of nozzle-generated turbulence on diesel sprays*. PhD thesis, Georgia Institute of Technology, 2017.

[92] E. C. Network, "Engine combustion network experimental data archive." http://www.sandia.gov/ECN.

[93] T. Poinsot and D. Veynante, *Theoretical and Numerical Combustion*. Edwards, 1931.

[94] S. P. Burke and T. E. W. Schumann, "Diffusion flames," *Industrial and Engineering Chemistry*, vol. 20, pp. 998–1004, 1928.

[95] A. Y. Klimenko and R. W. Bilger, "Conditional moment closure for turbulent combustion," *Progress in Energy and Combustion Science*, vol. 25, pp. 595–687, 1999.

[96] H. Pitsch, Y. P. Wan, and N. Peters, "Numerical investigation of soot formation and oxidation under diesel engine conditions," *SAE Paper 952357*, 1995.

[97] B. F. Magnussen and B. H. Hjertager, "On mathematical modeling of turbulent combustion with special emphasis on soot formation and combustion," *Symposium (International) on Combustion*, vol. 16, pp. 719–729, 1977.

[98] A. F. V. Bracco and R. D. Reitz, "Comparisons of computed and measured premixed charge engine combustion," *Combustion and Flame*, vol. 60, pp. 309–322, 1985.

[99] V. I. Golovitchev, N. Nordin, R. Jarnicki, and J. Chomiak, "3-d diesel spray simulations using a new detailed chemistry turbulent combustion model," *SAE Paper 2000-01-1891*, 2000.

[100] M. Mawid and S. Aggarwal, "A detailed numerical investigation of burke-schumann gaseous and spray flames," *AIAA-91-2311*, 1991.

[101] T. W. Park and S. K. Aggarwal, "Effect of gravity on the structure of an unsteady spray diffusion flame," *Combustion and Flame*, vol. 99, pp. 767–774, 1994.

[102] Y. M. Wright, G. D. Paola, K. Boulouchos, and E. Mastorakos, "Simulations of spray autoignition and flame establishment with two-dimensional cmc," *Combustion and Flame*, vol. 143, pp. 402–419, 1994.

[103] M. Bolla, T. Gudmundsson, Y. M. Wright, and K. Boulouchos, "Simulations of diesel sprays using the conditional moment closure model," *SAE Paper 2013-01-1618*, 2013.

[104] M. Bolla, D. Farrace, Y. M. Wright, K. Boulouchos, and E. Mastorakos, "Influence of turbulence–chemistry interaction for n-heptane spray combustion under diesel engine conditions with emphasis on soot formation and oxidation," *Combustion Theory and Modelling*, vol. 18, pp. 330–360, 2015.

[105] G. D'Errico, T. Lucchini, F. Atzler, and R. Rotondi, "Computational fluid dynamics simulation of diesel engines with sophisticated injection strategies for in-cylinder pollutant controls," *Energy and Fuels*, vol. 26, pp. 4212–4223, 2012.

[106] C. K. Blomberg, L. Zeugin, S. S. Pandurangi, M. Bolla, K. Boulouchos, and Y. M. Wright, "Modeling split injections of ecn "spray a" using a conditional moment closure combustion model with rans and les," *SAE Paper 2016-01-22378*, 2016.

[107] F. N. Williams, "Recent advances in theoretical descriptions of turbulent diffusion flames," *Turbulent Mixing in Nonreactive and Reactive Flows*, pp. 189–208, 1975.

[108] D. C. Haworth, M. C. Drake, S. B. Pope, and R. J. Blint, "The importance of time-dependent flame structures in stretched laminar flamelet models for turbulent jet diffusion flames," *Symposium (International) on Combustion*, pp. 589–597, 1988.

[109] F. Mauss, D. keller, and N. Peters, "A lagrangian simulation on flamelet extinction and re-ignition in turbulent jet diffusion flames," *Symposium (International) on Combustion*, pp. 693–698, 1990.

[110] H. Pitsch, M. Chen, and N. Peters, "Unsteady flamelet modeling of turbulent hydrogen-air diffusion flames," *Symposium (International) on Combustion*, pp. 1057–1064, 1998.

[111] H. Pitsch, H. Barths, and N. Peters, "Three-dimensional modeling of nox and soot formation in di-diesel engines using detailed chemistry based on the interactive flamelet approach," *SAE Paper 962057*, 1996.

[112] C. Hasse and N. Peters, "A two mixture fraction flamelet model applied to split injections in a di diesel engine," *Proceedings of the Combustion Institute*, vol. 30, pp. 2755—-2762, 2005.

[113] J. Weber, N. Peters, R. Diwakar, R. M. Siewert, and A. Lippert, "Simulation of the low-temperature combustion in a heavy duty diesel engine," *SAE Paper 2007-01-0904*, 2007.

[114] H. Barths, C. Hasse, G. Bikas, and N. Peters, "Simulation of combustion in direction injection diesel engines using a eulerian particle flamelet model," *Proceedings of the Combustion Institute*, vol. 28, pp. 1161–1168, 2000.

[115] H. Kim, N. Heo, Y. Kim, J.-H. Lee, and J. K. Lee, "Numerical study of combustion processes and pollutant formation in hsdi diesel engines," *SAE Paper 2004-01-0126*, 2004.

[116] M. Gauding, C. Felsch, B. Kerschgens, A. Vanegas, H. Won, N. Peters, and C. Hasse, "Applying an extended flamelet model for a multiple injection operating strategy in a common-rail di diesel engine," *SAE Paper 2009-01-0720*, 2009.

[117] M. Wang, M. Raju, E. Pomraning, P. Kundu, Y. Pei, and S. Som, "Comparison of representative interactive flamelet and detailed chemistry based combustion

models for internal combustion engines," in *Proceedings of the ASME 2014 Internal Combustion Engine Division Fall Technical Conference, ICEF2014-5522*, 2014.

[118] P. Kundu, *Tabulated Combustion Model Development For Non-Premixed Flames*. PhD thesis, North Carolina State University, 2015.

[119] G. D'Errico, T. Lucchini, F. Contino, M. Jangi, and X.-S. Bai, "Comparison of well-mixed and multiple representative interactive flamelet approaches for diesel spray combustion modelling," *Combustion Theory and Modelling*, vol. 18, pp. 65–883, 2014.

[120] D. B. Spalding, "Mixing and chemical reaction in steady confined turbulent flames," *Symposium (International) on Combustion*, pp. 649–657, 1971.

[121] M. P. Halstead, L. J. Kirsch, A. Prothero, and C. P. Quinn, "A mathematical model for hydrocarbon autoignition at high pressures," *Proceedings of the Royal Society A*, vol. 346, pp. 515–538, 1975.

[122] R. D. Reitz and F. V. Bracco, "Global kinetics models and lack of thermodynamic equilibrium," *Combustion and Flame*, vol. 53, pp. 141–144, 1983.

[123] S.-C. Kong and R. D. Reitz, "Multidimensional modeling of diesel ignition and combustion using a multistep kinetics model," *Journal of Engineering for Gas Turbines and Power*, vol. 115, pp. 781–789, 1993.

[124] Z. Han, A. Uludogan, G. J. Hampson, and R. D. Reitz, "Mechanism of soot and nox emission reduction using multiple-injection in a diesel engine," *SAE Paper 960633*, 1996.

[125] J. Xin, D. Montgomery, and R. D. Reitz, "Multidimensional modeling of combustion for a six-mode emissions test cycle on a di diesel engine," *Journal of Engineering for Gas Turbines and Power*, vol. 119, pp. 683–691, 1997.

[126] S.-C. Kong, Z. Han, and R. D. Reitz, "The development and application of a diesel ignition and combustion model for multidimensional engine simulation," *SAE Paper 950278*, 1995.

[127] G. D'Errico, D. Ettorre, and T. Lucchini, "Comparison of combustion and pollutant emission models for di diesel engines," *SAE Paper 2007-24-0045*, 2007.

[128] G. D'Errico, D. Ettorre, and T. Lucchini, "Simplified and detailed chemistry modeling of constant-volume diesel combustion experiments," *SAE Paper 2008-01-0954*, 2008.

[129] T. Lucchini, G. D'Errico, D. Ettorre, and G. Ferrari, "Numerical investigation of non-reacting and reacting diesel sprays in constant-volume vessels," *SAE Paper 2009-01-1971*, 2009.

[130] R. W. Bilger, "A note on favre averaging in variable density flows," *Combustion Science and Technology*, vol. 11, pp. 215–217, 1975.

[131] W. E. Ranz and W. R. Marshall, "Evaporation from drops," *Chemical Engineering Progress*, vol. 48, pp. 141–146, 1952.

[132] E. L. Wakill, O. A. Uyehara, and P. S. Myers, "Theoretical investigation of the hating up period of injected fuel droplets vaporizing in air; n.a.c.a. report 3179," tech. rep., 1954.

[133] R. Courant, K. Friedrichs, and H. Lewy, "On the partial difference equations of mathematical physics," *IBM Journal of Research and Development*, vol. 11, 1967.

[134] C. Kralj, *Numerical simulation of diesel spray processes.* PhD thesis, Imperial College, 1995.

[135] S.-H. Keum, *An Improved Representative Interactive Flamelet Model Accounting for Evaporation Effect in Reaction Space (RIF-ER).* PhD thesis, The University of Michigan, 2009.

[136] H. Barths, C. Antoni, and N. Peters, "Three-dimensional simulation of pollutant formation in a di diesel engine using multiple interactive flamelets," *SAE Paper 982459*, 1998.

[137] D. P. Schmidt, *Cavitation in Diesel Fuel Injector Nozzles.* PhD thesis, University of Wisconsin - Madison, 1997.

[138] F. Payri, V. Bermudez, R. Payri, and F. J. Salvador, "The influence of cavitation on the internal flow and the spray characteristics in diesel injection nozzles," *Fuel*, vol. 83, no. 4–5, pp. 419–431, 2004.

[139] J. K. Kim, K. Nishida, and H. Hiroyasu, "Characteristics of the internal flow in a diesel injection nozzle," *Proceedings of ICLASS 1997*, 1997.

[140] D. J. Duke, A. B. Swantek, F. Z. Tilocco, and A. L. Kastengren, "X-ray imaging of cavitation in diesel injectors," *SAE International Journal of Engines*, vol. 7, no. 2, pp. 1003–1016, 2014.

[141] K. E. Matusik, D. J. Duke, A. B. Swantek, C. F. Powell, and A. L. Kastengren, "High resolution x-ray tomography of injection nozzles," in *28th ILASS-Americas Conference, Dearborn, MI*, 2016.

[142] NIST, "Thermophysical properties of dodecane." http://webbook.nist.gov.

[143] C.-M. Termicos, "Engine combustion network experimental data archive." https://www.cmt.upv.es/ECN03.aspx#model.

[144] C. F. Powell and D. J. Duke, "Measurements of diesel spray droplet size with ultra-small angle x-ray scattering," in *25th Annual Conference on Liquid Atomization and Spray System*, 2013.

[145] A. Kastengren, J. Ilavsky, J. P. Viera, R. Payri, D. J. Duke, A. Swantek, F. Z. Tilocco, N. Sovis, and C. F. Powell, "Measurements of droplet size in shear-driven atomization using ultra-small angle x-ray scattering," *International Journal of Multiphase Flow*, vol. 92, pp. 131–139, 2017.

[146] G. L. Martinez, G. M. Magnotti, B. W. Knox, and C. L. Genzale, "Quantification of sauter mean diameter in diesel sprays using scattering-absorption extinction measurements," in *ILASS-Americas 29th Annual Conference on Liquid Atomization and Spray System*, 2017.

[147] S. Kim, B. F. Martinez, G. L. Yraguen, G. M. Magnotti, K. E. Matusik, B. A. Sforzo, A. L. Kastengren, C. F. Powell, T. Lucchini, G. D'Errico, B. W. Knox, and C. L. Genzale, "Validation of a new turbulence-induced lagrangian primary breakup model for diesel spray atomization," in *ICLASS 2018, 14th Triennial International Conference on Liquid Atomization and Spray Systems, Chicago, IL, USA*, 2018.

[148] J. Gimeno, G. Bracho, P. Marti-Aldaravi, and J. E. Peraza, "Experimental study of the injection conditions influence over n-dodecane and diesel sprays with two ecn single-hole nozzles. part i: Inert atmosphere," *Energy Conversion and Management*, vol. 126, pp. 1146–1156, 2016.

[149] H. Schlichting, *Boundary Layer Theory.* McGraw-Hill, 1979.

[150] J. O. Hinze, *Turbulence, 2nd ed.* New York, 1975.

[151] M. P. B. Musculus and K. Kattke, "Entrainment waves in diesel jets," *SAE Paper 2009-01-1355*, 2009.

[152] T.-H. Shih, W. W. Liou, A. Shabbir, Z. Yang, and J. Zhu, "A new k-e eddy viscosity model for high reynolds number turbulent flows," *Computers and Fluids*, vol. 24, no. 3, pp. 227–238, 1995.

[153] L. Cai, L. Kroger, and H. Pitsch, "Reduced and optimized mechanism for n-dodecane oxidation," in *15th international conference on numerical combustion, EM2C, CNRS - Ecole Centrale Paris, Avignon*, 2015.

[154] T. Yao, Y. Pei, B. J. Zhong, and T. Lu, "A hybrid mechanism for n-dodecane combustion with optimized low-temperature chemistry," in *9th U.S. national combustion meeting, Central States Section of the Combustion Institute*, 2015.

[155] K. Narayanaswamy, P. Perrine, and P. Heinz, "A chemical mechanism for low to high temperature oxidation of n-dodecane as a component of transportation fuel surrogates," *Combustion and Flame*, vol. 161, no. 4, pp. 866–884, 2014.

[156] N. Maes, M. Meijer, N. Dam, B. Somers, H. B. Toda, and G. Bruneaux, "Characterization of spray a flame structure for parametric variations in ecn constant-volume vessels using chemiluminescence and laser-induced fluorescence," *Combustion and Flame*, vol. 174, pp. 138–151, 2016.

[157] K. J. Richards, P. K. Senecal, and E. Pomraning, *CONVERGE 2.1. 0 Theory Manual, Convergent Science*, 2013.

[158] A. Babajimopoulos, D. N. Assanis, D. L. Flowers, S. M. Aceves, and R. P. Hessel, "A fully integrated computational fluid dynamics and multi-zone model with detailed chemical kinetics for the simulation of premixed charge compression ignition engines," *International Journal of Engine Research*, vol. 6, no. 5, pp. 497–512, 2005.

[159] P. Kundu, Y. Pei, M. Wang, R. Mandhapati, and S. Som, "Evaluation of turbulence-chemistry interaction under diesel engine conditions with multi-flamelet rif model," *Atomization and Sprays*, vol. 24, no. 9, pp. 779–800, 2014.

[160] P. Pal, S.-H. Keum, and H. G. Im, "Assessment of flamelet versus multi- zone combustion modeling approaches for stratified-charge compression ignition engines," *International Journal of Engine Research*, vol. 17, no. 3, pp. 280–290, 2016.

[161] P. Kundu, M. M. Ameen, and S. Som, "Importance of turbulence-chemistry interactions at low temperature engine conditions," *Combustion and Flame*, vol. 183, pp. 283–298, 2017.

[162] R. N. Dahms, G. A. Packzo, S. A. Skeen, and L. M. Pickett, "Understanding the ignition mechanism of high-pressure spray flames," *Proceedings of the Combustion Institute*, vol. 36, no. 2, pp. 2615–2623, 2017.

[163] C. Koci, G. Martin, T. Bazyn, W. Morrison, K. Svensson, and C. Gehrke, "The influence of diesel end-of-injection rate shape on combustion recession," *SAE Paper 2015-01-0795*, 2015.

[164] W. E. Eagle, M. P. B. Musculus, L. M. C. Malbec, and G. Bruneax, "Measuring transient entrainment rates of a confined vaporizing diesel jet," in *26th ILASS-Americas Conference, Portland, OR*, 2014.

[165] D. Jarrahbashi, S. Kim, B. W. Knox, and C. L. Genzale, "Computational analysis of end-of-injection transients and combustion recession," *International Journal of Engine Research*, vol. 18, no. 10, pp. 1088–1110, 2017.

[166] H. Hiroyasu and T. Kadota, "Models for combustion and formation of nitric oxide and soot in di diesel engines," *SAE Paper 760129*, 1976.